Markus Nyman

Generation and shaping of light in spatially dispersive metamaterials

School of Science

Thesis submitted for examination for the degree of Master of Science in Technology.

Espoo, May 31, 2016

Thesis supervisor:

Prof. Matti Kaivola

Thesis advisor:

D.Sc. (Tech.) Andriy Shevchenko

Aalto University
School of Science

AALTO UNIVERSITY
SCHOOL OF SCIENCE

ABSTRACT OF THE
MASTER'S THESIS

Author: Markus Nyman

Title: Generation and shaping of light in spatially dispersive metamaterials

Date: May 31, 2016 Language: English Number of pages: 7+65

Department of Applied Physics

Professorship: Optics and Photonics Code: Tfy-125

Supervisor: Prof. Matti Kaivola

Advisor: D.Sc. (Tech.) Andriy Shevchenko

Optical metamaterials are nanostructured materials that can be designed to exhibit extraordinary optical characteristics. Consisting of artificial nanoparticles called "metamolecules", optical metamaterials are usually spatially dispersive, and as a result, their optical response depends not only on light polarization but also on propagation direction. In this thesis we develop analytical and numerical calculation tools to study the propagation and generation of light in such materials. To address all relevant phenomena, we describe the materials in terms of wave parameters, which are refractive index and impedance determined for each plane wave separately. We develop an approach to analyze the interaction of optical beams with metamaterial slabs, and introduce a method valid even for materials that do not support polarization modes. We also develop a method to calculate the optical fields created by quantum emitters inside spatially dispersive metamaterial slabs. Equipped with these tools we design and analyze metamaterials with unique optical properties including compensation of optical diffraction, direction-sensitive reflectivity, interface-shaped wavefronts of a multimode light source, and highly directional spontaneous emission.

Keywords: metamaterials, light propagation, light emission, optical beams, computational electromagnetics

AALTO-YLIOPISTO
PERUSTIETEIDEN KORKEAKOULU

DIPLOMITYÖN
TIIVISTELMÄ

Tekijä: Markus Nyman

Työn nimi: Valon emissio ja eteneminen spatiaalisesti dispersiivisissä metamateriaaleissa

Päivämäärä: 31.5.2016 Kieli: Englanti Sivumäärä: 7+65

Teknillisen fysiikan laitos

Professuuri: Optiikka ja fotoniikka Koodi: Tfy-125

Työn valvoja: Prof. Matti Kaivola

Työn ohjaaja: TkT Andriy Shevchenko

Optiset metamateriaalit ovat nanorakenteisia materiaaleja joilla on tavallisesta poikkeavia optisia ominaisuuksia. Optiset metamateriaalit koostuvat keinotekoisista nanopartikkeleista, "metamolekyyleistä", ja ovat usein spatiaalisesti dispersiivisiä, jonka seurauksena niiden optinen vaste riippuu valon polarisaation lisäksi etenemissuunnasta. Tässä diplomityössä kehitetään analyyttisiä ja numeerisia menetelmiä joilla tutkia valon etenemistä ja generointia optisissa metamateriaaleissa. Jotta kaikki metamateriaalien optiset ilmiöt voidaan ottaa huomioon, materiaalien karakterisointiin käytetään aaltoparametrejä, jotka ovat jokaisen tasoaallon oma taitekerroin ja aaltoimpedanssi. Työssä kehitetään menetelmä optisten säteiden ja metamateriaalikalvojen vuorovaikutuksen analysointiin, sekä menetelmä joka soveltuu tähän myös materiaaleissa, joilla ei ole polarisaatiomoodeja. Työssä kehitetään myös menetelmä, jolla voidaan laskea spatiaalisesti dispersiiviseen metamateriaalikalvoon upotetun säteilylähteen optinen kenttä. Näiden työkalujen avulla diplomityössä kehitetään ja analysoidaan metamateriaaleja, joilla on ainutlaatuisia optisia ominaisuuksia kuten valon diffraktion kompensointi, suuntariippuva heijastavuus, monimuotovalonlähteestä lähtöisin olevat rajapintaan muotoutuvat aaltorintamat ja suunnattu spontaani emissio.

Avainsanat: metamateriaalit, valon eteneminen, valon emissio, optiset säteet, laskennallinen sähkömagnetiikka

Contents

Symbols and abbreviations

Symbols

$\mathbf{B}$	magnetic flux density
$\mathbf{D}$	electric flux density
D	directivity
$\mathbf{E}$	electric field
$\mathcal{E}$	emission enhancement factor
$\overleftrightarrow{\mathbf{G}}$	propagator
$\mathbf{H}$	magnetic field
$H(k_z)$	Hessian matrix
$\overleftrightarrow{\mathbf{I}}$	identity tensor
I	electric current
$\mathbf{J}_0$	electric current dipole moment
$\mathbf{J}_\mathrm{F}$	density of free electric current
$\mathbf{K}$	density of surface electric current
$\mathbf{M}$	magnetization
$\mathbf{P}$	polarization
$\mathcal{P}_\mathrm{h}$	Purcell factor relative to host medium
P	power
P_tot	total emission power
R	reflectance
$\mathbf{S}$	Poynting vector
$\overleftrightarrow{\mathbf{T}}$	transfer matrix of a layer
c	speed of light in vacuum
d	thickness of slab
$\overleftrightarrow{\boldsymbol{f}}$	unit cell transmission matrix
f	unit cell transmission coefficient
$\overleftrightarrow{\boldsymbol{g}}$	unit cell reflection matrix
g	unit cell reflection coefficient
$\mathbf{k}$	wave vector
k	wavenumber
k_0	wavenumber in vacuum
$\mathbf{k}_\mathrm{tr}$	transverse wave vector
$\mathbf{m}$	unit vector of TM-polarized electric field
$\mathbf{m}_\mathrm{J}$	unit vector of surface current generating TM-polarized waves
$\mathbf{n}$	normal vector of an interface
n	refractive index
q	electric charge
$\mathbf{r}$	position vector

t	time
$\mathbf{t}$	unit vector of TE-polarized electric field
$\mathbf{t}_{\mathrm{J}}$	unit vector of surface current generating TE-polarized waves
w	width
Γ	spontaneous emission rate
Γ_{h}	spontaneous emission rate in homogeneous host medium
Γ_{rad}	spontaneous emission rate into propagating modes
Λ_x	lattice constant in the x-direction
γ	wavenumber of effective wave
γ_z	z-component of wave vector of effective wave
ϵ	scalar electric permittivity
ϵ_0	electric permittivity of vacuum
$\overleftrightarrow{\epsilon}$	electric permittivity tensor
η	wave impedance
θ	propagation angle
λ	wavelength in a medium
λ_0	wavelength in vacuum
λ_{host}	wavelength in a host medium
μ	scalar magnetic permeability
μ_0	magnetic permeability of vacuum
$\overleftrightarrow{\mu}$	magnetic permeability tensor
ξ	ratio of intensities of emission in opposite directions
ρ_{12}	generalized Fresnel reflection coefficient from medium 1 to medium 2
$\rho_{\pm}$	reflection coefficient of metamolecular layer
ρ_{F}	density of free electric charge
$\overleftrightarrow{\boldsymbol{\rho}}^{\mathrm{slab}}$	reflection matrix of a metamaterial slab
σ	density of surface electric charge
τ_{12}	generalized Fresnel transmission coefficient from medium 1 to medium 2
$\tau_{\pm}$	transmission coefficient of metamolecular layer
$\overleftrightarrow{\boldsymbol{\tau}}^{\mathrm{slab}}$	transmission matrix of a metamaterial slab
ϕ	phase
$\overleftrightarrow{\chi}_e$	electric susceptibility
$\overleftrightarrow{\chi}_m$	magnetic susceptibility
ω	angular frequency

Operators

$\nabla \cdot \mathbf{E}$	the divergence of field $\mathbf{E}$
$\nabla \times \mathbf{E}$	the curl of field $\mathbf{E}$
$\mathbf{a} \cdot \mathbf{b}$	dot product of vectors $\mathbf{a}$ and $\mathbf{b}$
$\mathbf{a} \times \mathbf{b}$	cross product of vectors $\mathbf{a}$ and $\mathbf{b}$
$\dfrac{\partial}{\partial x}$	partial derivative with respect to x
$\dfrac{d}{dt}$	derivative with respect to t
$\displaystyle\int f(\mathbf{r}) d\mathbf{r}$	integral of function $f(\mathbf{r})$ over the three spatial dimensions
$\displaystyle\int_a^b f(t) dt$	integral of function $f(t)$ over t from a to b
$\overleftrightarrow{\boldsymbol{\tau}}\mathbf{E}$	matrix-vector product of matrix $\overleftrightarrow{\boldsymbol{\tau}}$ with vector $\mathbf{E}$
$\overleftrightarrow{\boldsymbol{\tau}}^{-1}$	inverse of matrix $\overleftrightarrow{\boldsymbol{\tau}}$
a^*	complex conjugate of a
$\mathbf{E}^*$	complex conjugate of each element of vector $\mathbf{E}$
$\mathrm{Re}\{a\}$	real part of complex number a
$\mathrm{Im}\{a\}$	imaginary part of complex number a
$\lvert a \rvert$	magnitude of complex number a
$\arg\{a\}$	complex angle of a
k_x	x-component of vector $\mathbf{k}$
$\mathbf{t}^\dagger$	conjugate transpose of vector $\mathbf{t}$
$\mathbf{t}\mathbf{t}^\dagger$	outer product of vector $\mathbf{t}$ with itself, producing a matrix

Abbreviations

2D	two-dimensional
3D	three-dimensional
ECDM	electric-current decomposition method
FDTD	finite-difference time-domain method
FEM	finite element method
FFT	Fast Fourier Transform
TE	transverse electric
TM	transverse magnetic

1 Introduction

Optical metamaterials, also known as photonic metamaterials, are nanostructured materials that can be designed to exhibit unusual electromagnetic characteristics in the infrared, visible, or ultraviolet regions of the spectrum [1]. While the structural units of natural materials are atoms and molecules, in metamaterials, they are solid-state nanoscatterers called meta-atoms or metamolecules. Examples of metamolecules include spheres, wires, rods, layers, discs and rings made of metal, semiconductor or dielectric materials embedded in a host medium which is typically glass or transparent polymer [2, 3]. The material structure is usually crystalline, composing a periodic array of unit cells that contain metamolecules. While the wavelengths of optical radiation are on the order of 1 µm, the unit cells of optical metamaterials have dimensions on the order of 100 nm, and are constructed using various nanofabrication methods [1]. Extraordinary optical characteristics have been demonstrated in metamaterials, including negative and zero refractive index [4, 5], hyperbolic dispersion [6] and exceptionally strong chirality [7]. Promising applications of such materials include sub-diffraction-limited resolution imaging [8, 9], enhanced and controlled emission of light [10–14], invisibility cloaking [15], waveguide coupling [16] and the elimination of optical diffraction [17–19]. Metamaterials are three-dimensional. A two-dimensional surface structure containing only one layer of metamolecules can be called a metasurface [20].

The goal of this thesis is to study the the propagation and generation of light in novel optical metamaterials. While propagation of an optical beam through a metamaterial slab can always be modelled by numerically solving Maxwell's equations in the microscopic structure [21], the calculation will be time-consuming and alone will provide quite limited insight into the material properties. One would like to view the metamaterial as a homogeneous *effective medium*. However, obtaining the effective optical characteristics can be a challenge due to the complexity of the material structure and its optical properties. Metamaterials are often anisotropic and temporally dispersive, meaning that their response depends on the polarization and frequency of a wave. In addition, metamaterials usually exhibit considerable *spatial dispersion*, which makes the material response depend on the light propagation direction [22]. To account for all these effects in a general way, we describe the interaction of electromagnetic plane waves with metamaterials in terms of using frequency-, polarization- and direction-dependent refractive indices and wave impedances [23–25]. To be able to study optical *beams* interacting with metamaterials we develop a semianalytical method based on a plane-wave decomposition [26].

We design and study three different metamaterials. Using a metamaterial constructed of short silver nanorods, we achieve the reduction of optical diffraction [19]. Despite its metallic metamolecules the material shows a very low absorption and its wave impedance is matched to the surrounding medium to suppress reflection from its surface. We show that one can transfer essentially arbitrary beams and images through slabs of such a metamaterial without changing their intensity profiles. The second metamaterial is composed of gold dimers (pairs of nanodiscs with different diameters). The material is *bifacial* so that counter-propagating electromagnetic

waves cause a different optical response of the material [24,27]. In particular, we find that a slab of such a material has different reflection coefficients on its opposite sides. Additionally, the material can be tuned such that it acts as a reflective spatial filter, absorbing obliquely-incident waves and reflecting normally-incident ones. Finally, we showcase a metamaterial composed of silver nanodiscs, which are rotated with respect to the crystal lattice. This material lacks polarization modes, but we develop a transfer-matrix approach based on the interferometric method to describe the properties of such materials [26]. As an example, we show that the polarization state of some waves propagating in the material changes purely due to spatial dispersion.

The study on generation of light in metamaterials is motivated by the fact that the material can significantly modify the characteristics of the emitters [28]. The modification can be studied by direct numerical calculations. For further insight and computational efficiency, we introduce a semianalytical method to model the emitting system using the wave parameters mentioned above. The method is based on decomposing an emitter, such as a point dipole, into a series of electric-current waves. We use both direct numerical calculations and this semianalytical method to study dipole emission in a number of different nanostructures. First, we demonstrate that a metallic waveguide at its cutoff frequency acts as a two-dimensional near-zero-index metamaterial. We use such a waveguide to modify the rate of spontaneous emission as well as to control the wavefronts of the field emitted out of the structure. Then, we show that emitters of light in a diffraction-compensating metamaterial create collimated beams, which do not spread upon propagation. We also show that the nanodisc dimers can be used as simple nanoantennas making the emission of light unidirectional. We demonstrate that the directivity can be improved if a metasurface composed of many such nanoantennas is used. Finally, we show that a bifacial metamaterial introduced previously can also make dipole emitters to radiate in one direction.

The thesis is organized as follows: Section 2 reviews the description of light-matter interaction from the point of view of classical electrodynamics, introduces the interferometric method for calculating the wave parameters, and describes the plane-wave decomposition method used to study the interaction of optical beams with metamaterials. In Section 3, we use the diffraction-compensating silver-rod metamaterial, the bifacial gold-dimer metamaterial and the polarization-converting silver-disc metamaterial to demonstrate the corresponding optical effects. Section 4 addresses the methods to model quantum emitters within the frame of classical electrodynamics, and introduces the electric-current decomposition method for dipole emitters in a general spatially dispersive metamaterial. In section 5 we study the modification of dipole emission in a number of nanostructures including zero-index waveguides, diffraction-compensating metamaterials, individual nanoantennas, metasurfaces and bifacial metamaterials. Section 6 summarizes the work and outlines future research directions.

2 Propagation of electromagnetic waves and beams in nanostructured materials

All optical properties of matter arise from microscopic interactions of light and the elementary charges of the atoms or molecules that matter is composed of. These interactions are fundamentally quantum-mechanical. Many are accurately described by semiclassical approaches, which retain the quantum description of the atoms but use classical electromagnetics to describe light. As an important example, atoms much smaller than the wavelength of light can be described as electric dipoles. This is known as the dipole approximation [29]. To move from the microscopic interaction picture to a macroscopic one, one uses spatial averaging. Classical electromagnetics then provides powerful tools to describe light-matter interaction when matter can be treated as continuous with a macroscopic dipole response, as opposed to considering the response of its discrete building blocks. In this section we review the principles of the propagation of light in matter. Beginning from classical electromagnetics of continuous media, we progress to characterize the propagation of light in metamaterials, in which the building blocks (metamolecules) are designed to give the desired optical properties. These properties are determined by a process of spatial averaging called *homogenization*. For this we use an interferometric approach that reveals the optical properties even for *spatially dispersive* metamaterials, which have traditionally been a difficult object of study. Finally, we use a plane-wave decomposition method to solve the challenging problem of propagation of arbitrary optical fields through metamaterial slabs.

2.1 Maxwell's equations and spatial dispersion

Maxwell's equations are the heart of classical electromagnetic theory. In their basic form they describe the interaction of electric and magnetic fields with electric charges. In materials composed of subwavelength structural units, the fields and charge distributions can be spatially averaged [30], which results in the macroscopic Maxwell's equations valid for macroscopically continuous media. The interaction of light with the media is described in terms of electric and magnetic polarization, using material parameters such as electric permittivity and magnetic permeability. Our first aim is to review how these arise from Maxwell's equations.

Spatially-averaged, macroscopic Maxwell's equations are [29]

$$\nabla \cdot \mathbf{D} = \rho_F, \tag{1}$$

$$\nabla \cdot \mathbf{B} = 0, \tag{2}$$

$$\nabla \times \mathbf{E} = -\frac{d\mathbf{B}}{dt}, \tag{3}$$

$$\nabla \times \mathbf{H} = \mathbf{J}_F + \frac{d\mathbf{D}}{dt}. \tag{4}$$

Here, $\mathbf{E}$ is the spatially-averaged electric field and $\mathbf{B}$ is the magnetic flux density, while ρ_F is the free charge density and $\mathbf{J}_F$ is the density of free electric current.

The auxiliary quantities $\mathbf{D}$, the electric flux density, and $\mathbf{H}$, the magnetic field, are defined as

$$\mathbf{D} = \epsilon_0 \mathbf{E} + \mathbf{P}, \tag{5}$$

$$\mathbf{H} = \frac{1}{\mu_0}\mathbf{B} - \mathbf{M}, \tag{6}$$

where $\mathbf{P}$ is the polarization, $\mathbf{M}$ is the magnetization, ϵ_0 is the vacuum permittivity and μ_0 is the vacuum permeability. In equations (1)–(6), polarization and magnetization effects are due to the excitation of electric and magnetic dipoles, and microscopic higher-order multipoles are not considered, as their contribution is usually negligibly small [30].

The properties of different materials enter the equations in constitutive relations that express $\mathbf{P}$ and $\mathbf{M}$ (or $\mathbf{D}$ and $\mathbf{B}$) in terms of the electric and magnetic fields. In their most general form, $\mathbf{P}$ and $\mathbf{M}$ at a coordinate $\mathbf{r}$ and an instant of time t depend on the values of $\mathbf{E}$ and $\mathbf{H}$ at a current and previous instants of time as well as in and around the considered point in space [31]. We express this dependence with the integrals

$$\mathbf{P}(\mathbf{r}, t) = \epsilon_0 \int_{-\infty}^{t} \int \overleftrightarrow{\chi}_e(\mathbf{r}', t'; \mathbf{r}, t)\mathbf{E}(\mathbf{r}', t')d\mathbf{r}'dt', \tag{7}$$

$$\mathbf{M}(\mathbf{r}, t) = \int_{-\infty}^{t} \int \overleftrightarrow{\chi}_m(\mathbf{r}', t'; \mathbf{r}, t)\mathbf{H}(\mathbf{r}', t')d\mathbf{r}'dt', \tag{8}$$

where $\overleftrightarrow{\chi}_e(\mathbf{r}', t'; \mathbf{r}, t)$ and $\overleftrightarrow{\chi}_m(\mathbf{r}', t'; \mathbf{r}, t)$ are the electric and magnetic susceptibility tensors, and $\overleftrightarrow{\chi}_e(\mathbf{r}', t'; \mathbf{r}, t)\mathbf{E}(\mathbf{r}', t')$ is the ordinary matrix-vector product. As long as the interaction is linear and the material is homogeneous, the susceptibilities depend only on the time difference $t' - t$ and the coordinate difference $\mathbf{r}' - \mathbf{r}$.

The dependence of $\mathbf{P}$ and $\mathbf{M}$ on the field values at the previous times leads to *temporal dispersion* that manifests itself as frequency dependence of the material response to a monochromatic field. To study such time-harmonic fields, which oscillate everywhere at some designated angular frequency ω, we express all fields in the form $\mathbf{F}(\mathbf{r}, t) = \hat{\mathbf{F}}(\mathbf{r}) \exp(-i\omega t)$, where $\hat{\mathbf{F}}(\mathbf{r})$ is the complex amplitude of the field. General time-dependent fields can be analyzed by Fourier-transforming all previous equations with respect to time. This decomposes the fields into their monochromatic components. For linear media the transformation replaces time convolution with multiplication by a frequency-dependent susceptibility, and for each frequency component, we have

$$\hat{\mathbf{P}}(\mathbf{r}, \omega) = \epsilon_0 \int \overleftrightarrow{\chi}_e(\mathbf{r}'; \mathbf{r}, \omega)\hat{\mathbf{E}}(\mathbf{r}', \omega)d\mathbf{r}', \tag{9}$$

$$\hat{\mathbf{M}}(\mathbf{r}, \omega) = \int \overleftrightarrow{\chi}_m(\mathbf{r}'; \mathbf{r}, \omega)\hat{\mathbf{H}}(\mathbf{r}', \omega)d\mathbf{r}', \tag{10}$$

where the single-frequency susceptibilities $\overleftrightarrow{\chi}_e(\mathbf{r}'; \mathbf{r}, \omega)$ and $\overleftrightarrow{\chi}_m(\mathbf{r}'; \mathbf{r}, \omega)$ are the Fourier transforms of $\overleftrightarrow{\chi}_e(\mathbf{r}', t' - t)$ and $\overleftrightarrow{\chi}_m(\mathbf{r}', t' - t)$, respectively.

In the majority of materials, $\mathbf{P}$ and $\mathbf{M}$ depend only on the fields at the same coordinate $\mathbf{r}$, in which case the spatial convolution of Eqs. (9) and (10) simply

disappears [31]. In other cases, e.g., in metamaterials, $\mathbf{P}$ and $\mathbf{M}$ depend on fields in nearby locations, an effect known as *spatial dispersion*. One can now apply the spatial Fourier transformation, which decomposes fields into their plane-wave components, each of which will induce different polarization and magnetization. The monochromatic plane wave solution of Maxwell's equations is written as

$$\mathbf{E}(\mathbf{r},t) = \tilde{\mathbf{E}}(\mathbf{k},\omega)\exp(i\mathbf{k}\cdot\mathbf{r})\exp(-i\omega t), \tag{11}$$

$$\mathbf{H}(\mathbf{r},t) = \tilde{\mathbf{H}}(\mathbf{k},\omega)\exp(i\mathbf{k}\cdot\mathbf{r})\exp(-i\omega t), \tag{12}$$

where $\mathbf{k}$ is the wave vector indicating the propagation direction of the wave, $\tilde{\mathbf{E}}(\mathbf{k},\omega)$ is the complex amplitude of the electric field, and $\tilde{\mathbf{H}}(\mathbf{k},\omega)$ is the complex magnetic field amplitude. For these fields, Eqs. (7) and (8) result in

$$\tilde{\mathbf{P}}(\mathbf{k},\omega) = \overleftrightarrow{\chi}_e(\mathbf{k},\omega)\tilde{\mathbf{E}}(\mathbf{k},\omega), \tag{13}$$

$$\tilde{\mathbf{M}}(\mathbf{k},\omega) = \overleftrightarrow{\chi}_m(\mathbf{k},\omega)\tilde{\mathbf{H}}(\mathbf{k},\omega), \tag{14}$$

where $\overleftrightarrow{\chi}_e(\mathbf{k},\omega)$ and $\overleftrightarrow{\chi}_m(\mathbf{k},\omega)$ are the susceptibility tensors that now depend on both the frequency and the wave vector. Hence, spatial dispersion causes the material to act differently for plane waves propagating in different directions. Since the tensor quantities depend on the properties of both the medium and the wave, they can be called *wave parameters* [32]. Using the susceptibilities, we can define the permittivity and permeability tensors as

$$\overleftrightarrow{\epsilon}(\mathbf{k},\omega) = \epsilon_0(\overleftrightarrow{\mathbf{I}} + \overleftrightarrow{\chi}_e(\mathbf{k},\omega)), \tag{15}$$

$$\overleftrightarrow{\mu}(\mathbf{k},\omega) = \mu_0(\overleftrightarrow{\mathbf{I}} + \overleftrightarrow{\chi}_m(\mathbf{k},\omega)), \tag{16}$$

where $\overleftrightarrow{\mathbf{I}}$ is the identity tensor. The convenient constitutive relations are now $\tilde{\mathbf{D}} = \overleftrightarrow{\epsilon}\tilde{\mathbf{E}}$ and $\tilde{\mathbf{B}} = \overleftrightarrow{\mu}\tilde{\mathbf{H}}$.

When substituting the plane-wave solution into Maxwell's equations, we note that the frequency ω and the wave vector $\mathbf{k}$ are not independent but connected through a dispersion relation $\omega = \omega(\mathbf{k})$. The surface (in the space of $\mathbf{k}$-vectors) formed by allowed $\mathbf{k}$ for a fixed frequency ω is the so-called isofrequency surface. For optically anisotropic materials, the direction of $\mathbf{E}$ and $\mathbf{H}$ also affect the dispersion relation, picking different tensor components from the permittivity and permeability tensors. Hence, the response of a material to an electromagnetic field can change as a function of the propagation direction even if the material is not spatially dispersive, i.e., when the tensors are constant. Optical anisotropy is very common in natural as well as artificial materials [33]. In principle, since anisotropy affects the dispersion relation, it could *also* be said to lead to spatial dispersion. In this work, we reserve the term *spatial dispersion* exclusively for the dependence of the material response on the direction of $\mathbf{k}$ as long as this effect can be separated from the effect of optical anisotropy.

The plane wave solution is a part of the field propagation method we will study later, and we would like to choose a more intuitive set of parameters to characterize plane wave propagation. The wave vector $\mathbf{k}$ has a length k (the wavenumber) that is related to the wavelength λ as $k = 2\pi/\lambda$, and the corresponding plane wave has a

certain relationship between the electric and magnetic field amplitudes $\tilde{\mathbf{E}}(\mathbf{k},\omega)$ and $\tilde{\mathbf{H}}(\mathbf{k},\omega)$. Therefore, we characterize the wave by the refractive index $n(\omega,\mathbf{k})$ and wave impedance $\eta(\omega,\mathbf{k})$, defined by the expressions

$$n(\omega,\mathbf{k}) = \frac{k}{k_0}, \tag{17}$$

$$\eta(\omega,\mathbf{k}) = \frac{E}{H}, \tag{18}$$

where $k_0 = \omega/c$ is the wavenumber in vacuum (c is the speed of light in vacuum), and E and H are the complex scalar amplitudes of the wave's electric and magnetic fields. For isotropic media with no spatial dispersion or anisotropy, n and η are frequency-dependent material parameters equal for all possible plane waves. If this is the case, scalar electric permittivity ϵ and magnetic permeability μ can be used as the material properties. The connection of ϵ and μ to n and η is given by the following equations

$$n = \sqrt{\frac{\epsilon}{\epsilon_0}}\sqrt{\frac{\mu}{\mu_0}}, \quad \eta = \sqrt{\frac{\mu}{\epsilon}}, \quad \epsilon = \frac{n}{c\eta}, \quad \mu = \frac{n\eta}{c}. \tag{19}$$

When dealing with plane waves, the refractive index and impedance are physically more intuitive as they directly describe the propagation of waves in a material. In Section 2.3 we will discuss the "validity" of ϵ and μ in metamaterials, and present a method to determine $n(\omega,\mathbf{k})$ and $\eta(\omega,\mathbf{k})$ for almost any material.

Electromagnetic fields store and transport energy. This is described by the electric and magnetic energy densities u_e and u_m and the Poynting vector $\mathbf{S}$ that gives the direction and magnitude of power flow density. The Poynting vector is defined as [29]

$$\mathbf{S} = \mathbf{E} \times \mathbf{H}. \tag{20}$$

The magnitude of $\mathbf{S}$ is equal to the optical power per unit surface area (perpendicular to $\mathbf{S}$). It is a time-dependent, oscillating quantity. For time-harmonic fields we can average $\mathbf{S}$ over one oscillation and define the time-averaged Poynting vector

$$\hat{\mathbf{S}} = \frac{1}{2}\mathrm{Re}\{\hat{\mathbf{E}} \times \hat{\mathbf{H}}^*\}, \tag{21}$$

where the asterisk stands for complex conjugation. For plane waves and in the absence of anisotropy, the Poynting vector is parallel to the wave vector $\mathbf{k}$ and its magnitude is $\hat{S} = 1/2\mathrm{Re}\{EH^*\}$. Using the definition of the wave impedance, Eq. (18), we can write the magnitude of the plane-wave Poynting vector as

$$\hat{S} = \frac{1}{2}\mathrm{Re}\left\{\frac{1}{\eta^*}\right\}|\hat{E}|^2 = \frac{1}{2}\frac{\mathrm{Re}\{\eta\}}{|\eta|^2}|\hat{E}|^2. \tag{22}$$

The definition of electromagnetic energy densities, and the physical meaning of the Poynting vector are not straightforward in the presence of temporal and spatial dispersion. Dispersion must be explicitly included in these definitions to avoid

unphysical phenomena, such as generation of energy at an interface between two materials [34–36]. Equations (13) and (14) show, however, that for time-harmonic plane waves, dispersion only enters the model through selecting different constants. It appears to be unclear whether or not the Poynting vector is a physically reasonable quantity for time-harmonic fields in strongly dispersive media. Nevertheless, as long as we consider power flow outside the medium – where, in fact, it can be measured – this problem does not exist and the above definitions may be used.

2.2 Boundary conditions

We have, up until now, assumed that plane waves propagate in a space filled with the material of interest. However, we also wish to study how waves propagate through interfaces between two different media. When the interface is infinitely thin, i.e., the medium changes abruptly from medium 1 to medium 2, we can use the electromagnetic boundary conditions. These conditions are [29]

$$\mathbf{n} \times (\mathbf{E}_1 - \mathbf{E}_2) = 0, \tag{23}$$
$$\mathbf{n} \times (\mathbf{H}_1 - \mathbf{H}_2) = \mathbf{K}, \tag{24}$$
$$\mathbf{n} \cdot (\mathbf{D}_1 - \mathbf{D}_2) = \sigma, \tag{25}$$
$$\mathbf{n} \cdot (\mathbf{B}_1 - \mathbf{B}_2) = 0, \tag{26}$$

where $\mathbf{n}$ is the normal of the interface directed from medium 1 to medium 2, $\mathbf{K}$ is the surface electric-current density on the interface, σ is the surface charge density, and the subindices 1 and 2 denote the two different media; $\mathbf{K}$ and σ only contain free currents and charges. For plane waves, these conditions also prescribe

$$\mathbf{n} \times \mathbf{k}_1 = \mathbf{n} \times \mathbf{k}_2, \tag{27}$$

which shows that the wave vector component along the interface is conserved when a plane wave propagates through it. For simplified notation, let us fix the coordinate system such that the z-axis is along the normal $\mathbf{n}$. Let us now define the propagation angle for both of the plane waves as

$$\theta = \arccos \frac{k_z}{k} = \arcsin \frac{k_{\mathrm{tr}}}{k}, \tag{28}$$

where k_z is the z-component of the wave vector and $k_{\mathrm{tr}} = \sqrt{k_x^2 + k_y^2}$ is the transverse component (with respect to z). Using also $k = k_0 n$ from Eq. (17), we can write Eq. (27) as the familiar law of refraction (Snell's law),

$$n_1 \sin\theta_1 = n_2 \sin\theta_2. \tag{29}$$

This law is valid for both real and complex refractive indices. However, with complex indices the angles will also be complex. They no longer directly represent the wavefront propagation angle, but are instead normalized measures of the wave vector components defined by Eq. 28. One can still derive the direction of wavefront propagation [37], but this will not be necessary for our purposes.

The boundary conditions clearly depend on the polarization (direction of electric field) of the waves incident on the interface. Instead of using the x-, y- and z-components of the fields, two mutually orthogonal polarizations suffice to describe the waves in relation to the interface. These are the transverse electric (TE) and transverse magnetic (TM) polarizations. For the TE polarization, $\mathbf{n} \cdot \mathbf{E} = 0$ so that the electric field is always in the plane of the interface. For the TM polarization, $\mathbf{n} \cdot \mathbf{H} = 0$ and the same is true for the magnetic field. These polarizations do not change upon transmission or reflection by the interface.

2.3 Metamaterials and interferometric approach

As explained in Section 1, metamaterials consist of structural units that are smaller than the wavelength of light. More specifically, the unit cells of a metamaterial's crystal lattice tend to have dimensions ranging from $\lambda/10$ to $\lambda/2$, where λ is the wavelength in the host medium. Metamaterials are in many ways similar to photonic crystals, which are also nanostructured media, but operate in different ways [38]. Metamaterials have smaller and more complex unit cells and allow only one mode of propagation (the fundamental Bloch mode [39]) to exist for each frequency, polarization and wave-vector direction, while photonic crystals typically have simpler, but larger unit cells, in order to use the Bragg reflection regime. Metamaterials can often be treated as homogeneous media, which simplifies their macroscopic description.

Various methods exist for homogenization, calculation of the macroscopic optical properties of metamaterials. Fundamentally, these methods are based on spatial averaging over a unit cell [23, 40–42]. This can be challenging since the unit cells of metamaterials are usually anisotropic and not negligibly small compared to the wavelength of interest, which makes the materials strongly spatially dispersive. The traditional permittivity and permeability tensors are no longer convenient for describing these materials, since the tensors will depend on the propagation direction as we outlined in the previous section. Some homogenization methods introduce additional magneto-electric coupling in the form of bianisotropic tensors [43, 44], but these fail to describe the response of spatially dispersive materials for all possible propagation angles. Instead of attempting to determine the angle-dependent tensor quantities, we choose to use plane wave propagation parameters, the refractive index and wave impedance (see Eqs. (17) and (18)), evaluated for each frequency, propagation direction and polarization. This can be done using permittivity and permeability as well, but in metamaterials these quantities can be misleading. Permittivity and permeability, respectively, are associated with electric and magnetic dipole excitations, but for metamaterials, the correspondence does not hold. For example, a permeability other than μ_0 may appear even without any magnetic-dipole excitations in the material [40, 45]. Hence, refractive index and wave impedance are more appropriate wave parameters as they directly describe the properties of the waves propagating in the material. The interferometric approach to homogenization, introduced and expanded in [23–26], is based on this premise.

The interferometric approach considers a crystalline metamaterial as a layered medium. Each layer is a two-dimensional lattice consisting of unit cells filled with

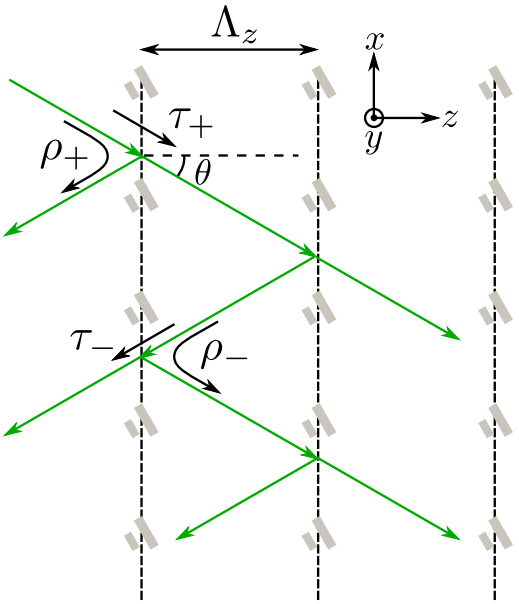

Figure 1: A plane wave (with **k**-vectors in green) propagating in a crystalline, layered medium, experiencing multiple reflections from the layers. The layers are separated by the lattice constant Λ_z and have transmission and reflection coefficients τ_+ and ρ_+ for the forward-propagating wave, and τ_- and ρ_- for the backward-propagating wave.

the host medium and containing the metamolecules. The widths of the unit cell, which are also the periods of the lattice, are Λ_x and Λ_y for the transverse directions (within one metamolecular layer) and Λ_z for the longitudinal direction perpendicular to the layers. As long as Λ_x and Λ_y are smaller than $\lambda_{\text{host}}/2$, where $\lambda_{\text{host}} = \lambda_0/n_{\text{host}}$ is the wavelength in the host medium, a plane wave being transmitted and reflected by one layer remains a plane wave as it is not split by diffraction. For this wave the layer of metamolecules has a transmission coefficient τ and a reflection coefficient ρ, which are defined as the ratios of the transmitted and reflected electric field amplitudes to the incident amplitude. These are generally determined numerically by letting a plane wave propagate through a layer of metamolecules and measuring the corresponding amplitudes. Figure 1 shows the **k**-vectors (green) of a plane wave propagating in a layered medium at an angle θ and being transmitted and reflected by the metamolecular layers. We note that the wave, once reflected, also strikes a layer from the opposite angle $(\pi - \theta)$. One propagation mode can therefore experience two sets of transmission and reflection coefficients. Those for the wave going in the $+z$-direction are τ_+ and ρ_+, and those for the wave going in the $-z$-direction are τ_- and ρ_-. To represent propagation through the unit cell we multiply the coefficients by the propagational phase shift, defining the coefficients

$$f_+ = \tau_+ \exp(ik_z\Lambda_z), \tag{30}$$
$$f_- = \tau_- \exp(ik_z\Lambda_z), \tag{31}$$
$$g_+ = \rho_+ \exp(ik_z\Lambda_z), \tag{32}$$
$$g_- = \rho_- \exp(ik_z\Lambda_z), \tag{33}$$

where k_z is the z-component of the wave vector in the host medium. We now define the *effective plane wave* propagating inside the homogenized metamaterial. It consists of forward and backward propagating "host-medium plane waves", and its electric and magnetic fields are the fields of these two waves spatially averaged over a unit cell. The averaging can be done analytically as the metamolecules in each layer can be "compressed" into an infinitely thin sheet which has the transmission and reflection coefficients $\tau_\pm$ and $\rho_\pm$. The z-component of the effective wave's wave vector, γ_z, satisfies the equation

$$\gamma_z \Lambda_z = -i \ln \left[\frac{\alpha}{2\beta} \pm (\frac{\alpha^2}{4\beta^2} - \frac{1}{\beta})^{1/2} \right] + 2\pi m, \tag{34}$$

where m is an integer and

$$\alpha = f_- + f_+^{-1}(1 - g_+ g_-), \tag{35}$$

$$\beta = f_-/f_+. \tag{36}$$

We omit the derivations of these expressions, as they are presented in [25]. Obviously, we can write

$$\gamma^2 = n_{\text{eff}}^2 k_0^2 = k_x^2 + k_y^2 + \gamma_z^2, \tag{37}$$

where γ is the wavenumber of the wave in the metamaterial, n_{eff} is the effective refractive index, and k_x and k_y are the transverse wave-vector components. This lets us calculate n_{eff} directly. The wave impedance, η_{eff}, is given by

$$\eta_{\text{eff}} = \eta \left(\frac{k\gamma_z}{k_z \gamma} \right)^p \frac{g_- + [1 - f_+ \exp(-i\gamma_z \Lambda_z)]}{g_- - [1 - f_+ \exp(-i\gamma_z \Lambda_z)]}, \tag{38}$$

where η is the impedance of the host medium and p is $+1$ for TE polarization and -1 for TM polarization. The wave parameters n_{eff} and η_{eff} can be calculated for any possible plane wave with a wave vector $\mathbf{k} = (k_x, k_y, k_z)$ and two orthogonal polarizations.

Consider now the interface problem described in Section 2.2. Having n_{eff} and η_{eff}, the boundary conditions can be used to derive the Fresnel coefficients, which are the transmission and reflection coefficients for a plane wave incident onto the interface. The ordinary form of these coefficients is not sufficient for spatially dispersive materials, and therefore, the following generalized Fresnel coefficients must be used [25]

$$\tau = \frac{\gamma_{z,i}/(\gamma_i \eta_i^p) + \gamma_{z,r}/(\gamma_r \eta_r^p)}{\gamma_{z,r}/(\gamma_r \eta_r^p) + \gamma_{z,t}/(\gamma_t \eta_t^p)} \left(\frac{\eta_i}{\eta_t} \right)^{(p-1)/2}, \tag{39}$$

$$\rho = \frac{\gamma_{z,i}/(\gamma_i \eta_i^p) - \gamma_{z,t}/(\gamma_t \eta_t^p)}{\gamma_{z,r}/(\gamma_r \eta_r^p) + \gamma_{z,t}/(\gamma_t \eta_t^p)} \left(-\frac{\eta_i}{\eta_r} \right)^{(p-1)/2}, \tag{40}$$

where subindex i denotes the incident wave, r the reflected wave, and t the transmitted wave. The parameter p is ± 1, picking plus for the TE polarization and minus for

TM polarization. In these equations we have dropped the subscript "eff" to shorten the notation.

Symmetries in the microscopic structure of the metamaterial influence how the layer transmission and reflection coefficients are related to one another. The isofrequency surfaces of the wave parameters then assume similar symmetries. In the simplest case, the metamolecules are centrosymmetric, the case for, e.g., elliptical particles, located at the center of the unit cell. In this case, plane waves arriving in the medium at angles $\pm\theta$ and $\pi \pm \theta$ experience the same transmission and reflection. The condition prescribes $\tau_+ = \tau_-$ and $\rho_+ = \rho_-$, which gives rise to centrosymmetric isofrequency surfaces for both the refractive index and wave impedance. The wave parameters are therefore equal for waves with $\mathbf{k}$ and $-\mathbf{k}$, which is in fact always true of the refractive index due to optical reciprocity [24]. For non-centrosymmetric metamolecules, such as pairs of discs or rods with different sizes, the layer reflection coefficients will be different for the angles θ and $\pi-\theta$. In these *bifacial* metamaterials, the impedance may be different for waves propagating in opposite directions. Finally, if the metamolecules are tilted with respect to the layers, both refractive index and impedance can be different for the waves at θ and $-\theta$ or $\pi+\theta$. These materials have been called *internally twisted* metamaterials [25]. *Chiral* metamaterials, composed of, e.g., spiral metamolecules, may have symmetric isofrequency surfaces for elliptically-polarized waves instead of the TE- and TM-polarized waves.

The TE and TM polarizations are customarily used when considering flat surfaces or slabs of metamaterials. However, they are not always the propagation modes in the material. Presumably one could replace the TE and TM modes in the equations presented above with some elliptically-polarized modes and the method would still be valid. In general, a material may not have any polarization modes, and no wave parameters can be introduced. We can still describe plane-wave propagation in these materials by another method based on the interferometric approach. This method uses transfer matrices for single-layer transmission and reflection [26], and is valid for *any* crystalline metamaterial.

Instead of the transmission and reflection coefficients of Eqs. (30)–(33), the transfer-matrix method uses single-layer transmission and reflection matrices

$$\overleftrightarrow{\boldsymbol{f}} = \begin{bmatrix} \tau_{ss} & \tau_{sp} \\ \tau_{ps} & \tau_{pp} \end{bmatrix} e^{ik_z\Lambda_z}, \tag{41}$$

$$\overleftrightarrow{\boldsymbol{g}} = \begin{bmatrix} \rho_{ss} & \rho_{sp} \\ \rho_{ps} & \rho_{pp} \end{bmatrix} e^{ik_z\Lambda_z}, \tag{42}$$

where each element τ_{ij} is the transmission coefficient for the incident wave with polarization i to the transmitted wave with polarization j, and the reflection matrix elements ρ_{ij} are defined similarly. Here, s and p are used to denote the TE and TM polarizations that are defined with respect to the considered layer of metamolecules. The elements can be measured by letting a TE- or TM-polarized plane wave propagate through a layer and measuring both the TE and TM polarization components in the reflected and transmitted waves. The transfer matrix of the layer can be constructed by noting that there are four waves in the system: forward and backward propagating

waves on both the left and right sides of each layer in the material. We wish to express the waves on the right as functions of the waves on the left,

$$\begin{bmatrix} \tilde{\mathbf{E}}_+^R \\ \tilde{\mathbf{E}}_-^R \end{bmatrix} = \overleftrightarrow{\mathbf{T}} \begin{bmatrix} \tilde{\mathbf{E}}_+^L \\ \tilde{\mathbf{E}}_-^L \end{bmatrix}, \tag{43}$$

where $\tilde{\mathbf{E}}_+^R$ is the right-side forward-propagating wave (going away from the layer), $\tilde{\mathbf{E}}_-^R$ is the right-side backward-propagating wave (coming towards the layer), and the field amplitudes on the left are defined similarly. $\overleftrightarrow{\mathbf{T}}$ is the following transfer matrix:

$$\overleftrightarrow{\mathbf{T}} = \begin{bmatrix} \overleftrightarrow{\mathbf{T}}_{11} & \overleftrightarrow{\mathbf{T}}_{12} \\ \overleftrightarrow{\mathbf{T}}_{21} & \overleftrightarrow{\mathbf{T}}_{22} \end{bmatrix} = \begin{bmatrix} \overleftrightarrow{\boldsymbol{f}}_+^{-1} & -\overleftrightarrow{\boldsymbol{f}}_+^{-1}\overleftrightarrow{\boldsymbol{g}}_- \\ \overleftrightarrow{\boldsymbol{g}}_+\overleftrightarrow{\boldsymbol{f}}_+^{-1} & -\overleftrightarrow{\boldsymbol{g}}_+\overleftrightarrow{\boldsymbol{f}}_+^{-1}\overleftrightarrow{\boldsymbol{g}}_- \end{bmatrix}. \tag{44}$$

The transfer matrix of a N-layer slab is then simply $\overleftrightarrow{\mathbf{T}}^N$, and the slab reflection and transmission coefficients can be solved by combining Eqs. (43) and (44). The slab coefficients are the elements of transmission and reflection matrices similar to those in Eqs. (41) and (42). They can be evaluated from the equations [26]

$$\overleftrightarrow{\boldsymbol{\tau}}_+^{\text{slab}} = \overleftrightarrow{\mathbf{T}}_{11}^{-1}, \tag{45}$$

$$\overleftrightarrow{\boldsymbol{\rho}}_+^{\text{slab}} = \overleftrightarrow{\mathbf{T}}_{21}\overleftrightarrow{\boldsymbol{\tau}}_+^{\text{slab}}, \tag{46}$$

$$\overleftrightarrow{\boldsymbol{\rho}}_-^{\text{slab}} = -\overleftrightarrow{\boldsymbol{\tau}}_+^{\text{slab}}\overleftrightarrow{\mathbf{T}}_{12}, \tag{47}$$

$$\overleftrightarrow{\boldsymbol{\tau}}_-^{\text{slab}} = \overleftrightarrow{\mathbf{T}}_{22} + \overleftrightarrow{\boldsymbol{\rho}}_+^{\text{slab}}\overleftrightarrow{\boldsymbol{\tau}}_+^{\text{slab}}\overleftrightarrow{\boldsymbol{\rho}}_-^{\text{slab}}. \tag{48}$$

The most significant limitation of the interferometric approach is that the meta-molecular layers must not be coupled through evanescent parts of the propagating waves. If the coupling is present, the layers cannot be treated as separate, and one must consider an entire slab of the material at once, partially defeating the purpose of introducing wave parameters. The parameters can still be calculated, but they will depend on the number of layers in the slab. Of course, this still allows one to calculate transmission and reflection from the slab surrounded by other arbitrary media without needing further numerical calculations for the transmission and reflection. The limitation of transverse periods, $\Lambda_{x/y} < \lambda_{\text{host}}/2$, was discussed previously, and is necessary to avoid diffractive splitting of the plane waves in the host medium. Another limitation concerns the z-period of the metamaterial. If $\gamma_z \Lambda_z \geq \pi$, we reach the regime of Bragg reflection, where the material becomes like a one-dimensional photonic crystal and homogenization no longer makes sense due to additional propagation modes.

2.4 Interaction of optical beams with metamaterial slabs

All realistic electromagnetic fields are limited in their transverse dimensions, i.e., they are beam-like. It is therefore essential to know how optical beams interact with metamaterials. Here we present a theoretical method that describes the propagation of time-harmonic electromagnetic fields through metamaterial slabs of finite thickness.

The materials are characterized by wave parameters, refractive index and impedance, and if they cannot be introduced, the slab transmission and reflection matrices. The method, proposed in [26], is a Fourier optics-based approach, expressing a beam-like field as a sum of plane waves for which the wave parameters can be calculated.

Let us consider a time-harmonic electric field with complex amplitude $\hat{\mathbf{E}}(\mathbf{r})$ defined on a xy-plane at some coordinate z (the position vector is $\mathbf{r} = x\mathbf{x} + y\mathbf{y} + z\mathbf{z}$). The plane-wave decomposition of the field is [29]

$$\hat{\mathbf{E}}(\mathbf{r}) = \frac{1}{4\pi^2}\int_{-\infty}^{\infty}\int_{-\infty}^{\infty}\tilde{\mathbf{E}}(\mathbf{k};z)e^{i(k_x x+k_y y)}dk_x dk_y, \tag{49}$$

where k_x and k_y are the transverse components of the wave vector of a plane-wave component with amplitude $\tilde{\mathbf{E}}(k_x, k_y; z)$. The amplitudes are obtained by the Fourier transform

$$\tilde{\mathbf{E}}(\mathbf{k};z) = \int_{-\infty}^{\infty}\int_{-\infty}^{\infty}\hat{\mathbf{E}}(\mathbf{r})e^{-i(k_x x+k_y y)}dxdy. \tag{50}$$

Let us now fix the *input plane*, where the field $\hat{\mathbf{E}}(\mathbf{r})$ is initially known, at $z = 0$. Once we have the plane-wave spectrum of the field, $\tilde{\mathbf{E}}(\mathbf{k}; 0)$, we can separately propagate each plane wave to another xy-plane. The spectrum on the other plane is

$$\tilde{\mathbf{E}}(\mathbf{k};z) = \overleftrightarrow{\mathbf{G}}(\mathbf{k},z)\tilde{\mathbf{E}}(\mathbf{k};0), \tag{51}$$

where $\overleftrightarrow{\mathbf{G}}(\mathbf{k}, z)$ is the *propagator* for the plane wave with wave vector $\mathbf{k}$. The propagator is an operator that "transfers" the plane wave from one plane at coordinate z to an another. It is, in general, a $\mathbf{k}$-dependent matrix describing the TE- and TM-polarized waves. The simplest propagator is the propagator in a homogeneous material [29],

$$\overleftrightarrow{\mathbf{G}}(\mathbf{k},z) = e^{ik_z z}\overleftrightarrow{\mathbf{I}} \tag{52}$$

where $\overleftrightarrow{\mathbf{I}}$ is the identity matrix. The longitudinal wave-vector component k_z will be

$$k_z = \pm\sqrt{k^2 - k_x^2 - k_y^2}. \tag{53}$$

The choice of sign is always "+" when k is positive and we consider propagation in the positive z-direction. Both propagating and evanescent waves can be considered in the plane-wave decomposition, e.g., if evanescent-wave focusing or superresolution imaging are considered. For far fields, it is convenient to simply discard the evanescent waves.

Let us now derive the propagator for a slab of a metamaterial. Consider that the slab has a thickness D, and surface normals directed along the z-axis, and that a set of $\mathbf{k}$-dependent transmission and reflection coefficients for TE and TM polarizations, $\tau_{\mathrm{TE}}(\mathbf{k})$, $\tau_{\mathrm{TM}}(\mathbf{k})$, $\rho_{\mathrm{TE}}(\mathbf{k})$ and $\rho_{\mathrm{TM}}(\mathbf{k})$, are known. Figure 2 depicts the problem, showing a beam with an electric field distribution defined on the left surface of the slab, at $z = 0$. To resolve the polarizations we decompose each plane wave (with the x, y and z-polarized components) into the TE and TM components. For this we define the unit vectors in the directions of the TE and TM polarizations,

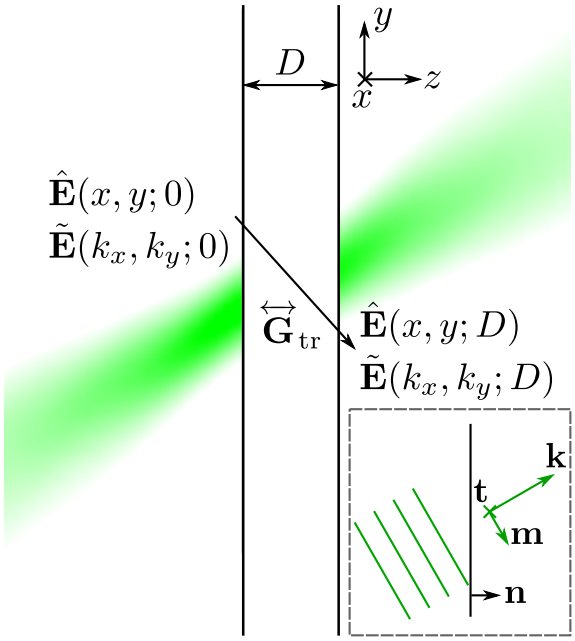

Figure 2: Propagation of a beam through a metamaterial slab (thickness D). The beam has an electric field $\hat{\mathbf{E}}(x,y;0)$ defined at the input interface of the slab, which is Fourier-transformed to its plane wave spectrum $\tilde{\mathbf{E}}(k_x,k_y;0)$. The transmission propagator $\overleftrightarrow{\mathbf{G}}_{\mathrm{tr}}$ determines the transmitted plane wave spectrum $\tilde{\mathbf{E}}(k_x,k_y;D)$ at the output interface, which can be inverse-Fourier-transformed to the beam's transmitted electric field $\hat{\mathbf{E}}(x,y;D)$. Inset: a plane wave with wave vector $\mathbf{k}$ is incident onto an interface with normal vector $\mathbf{n}$. Its electric field can be divided into two polarization components, in the directions of the unit vectors $\mathbf{t}$ and $\mathbf{m}$.

which are, respectively,

$$\mathbf{t}(\mathbf{k}) = \frac{\mathbf{k}\times\mathbf{n}}{|\mathbf{k}\times\mathbf{n}|}, \tag{54}$$

$$\mathbf{m}(\mathbf{k}) = \frac{\mathbf{t}\times\mathbf{k}}{k}, \tag{55}$$

where $\mathbf{n}$ is the slab surface normal (see the inset of Fig. 2). The electric field can then be written as

$$\tilde{\mathbf{E}}(\mathbf{k}) = \tilde{\mathbf{E}}_{\mathrm{TE}}(\mathbf{k}) + \tilde{\mathbf{E}}_{\mathrm{TM}}(\mathbf{k}) = \mathbf{t}\mathbf{t}^{\dagger}\tilde{\mathbf{E}}(\mathbf{k}) + \mathbf{m}\mathbf{m}^{\dagger}\tilde{\mathbf{E}}(\mathbf{k}). \tag{56}$$

where $\mathbf{t}^{\dagger}$ denotes the conjugate transpose of the column vector $\mathbf{t}$, making $\mathbf{t}\mathbf{t}^{\dagger}$ a projection matrix. Applying the transmission or reflection coefficients to the two polarizations results in the slab transmission and reflection propagators

$$\overleftrightarrow{\mathbf{G}}_{\mathrm{tr}} = \left[\tau_{\mathrm{TE}}(\mathbf{k})\mathbf{t}\mathbf{t}^{\dagger} + \tau_{\mathrm{TM}}(\mathbf{k})\mathbf{m}\mathbf{m}^{\dagger}\right], \tag{57}$$

$$\overleftrightarrow{\mathbf{G}}_{\mathrm{ref}} = \left[\rho_{\mathrm{TE}}(\mathbf{k})\mathbf{t}\mathbf{t}^{\dagger} + \overleftrightarrow{\rho}_{\mathrm{TM}}(\mathbf{k})\mathbf{m}\mathbf{m}^{\dagger}\right]. \tag{58}$$

We had to introduce an additional reflection matrix for TM-polarized electric field components, because the fields change direction upon reflection. The matrix is given

by

$$\overleftrightarrow{\rho}_{\mathrm{TM}}(\mathbf{k}) = \rho_{\mathrm{TM}}(\mathbf{k})(\overleftrightarrow{\mathbf{I}} - 2\mathbf{n}\mathbf{n}^{\dagger}). \tag{59}$$

The transmission propagator $\overleftrightarrow{\mathbf{G}}_{\mathrm{tr}}$ determines the transmitted plane wave at $z = D$, as shown in Fig. 2, while the reflection propagator $\overleftrightarrow{\mathbf{G}}_{\mathrm{ref}}$ determines the reflected wave at $z = 0$.

The slab transmission and reflection coefficients are the generalized Fabry-Pérot coefficients [33]. For a plane wave incident from medium 1 onto a slab (medium 2) with medium 3 on the other side of the slab, the coefficients valid for both TE and TM polarizations are

$$\tau_{\mathrm{slab}} = \frac{\tau_{12}\tau_{23}\exp(i\gamma_z D)}{1 - \rho_{21}\rho_{23}\exp(i\gamma_z 2D)}, \tag{60}$$

$$\rho_{\mathrm{slab}} = \rho_{12} + \frac{\tau_{12}\tau_{21}\rho_{23}\exp(i\gamma_z 2D)}{1 - \rho_{21}\rho_{23}\exp(i\gamma_z 2D)}, \tag{61}$$

where γ_z is the z-component of the wave vector in the metamaterial, τ_{ij} and ρ_{ij} denote the generalized Fresnel transmission and reflection coefficients, respectively, for a plane wave incident from medium i onto an interface between media i and j. These coefficients are given in Eqs. (39) and (40).

When the material is described using the transfer-matrix approach, Eqs. (60) and (61) must be replaced with Eqs. (45)–(48) that allow the slab to convert TE polarization into TM polarization and vice versa.

The presented approach allows one to propagate arbitrary optical fields through any metamaterial slab, as long as the transmission and reflection coefficients of the slab can be calculated. This can be done for almost any metamaterial with the interferometric approach, or, in the presence of interlayer evanescent-wave coupling, with direct numerical calculations. The implementation of the method on a computer is straightforward and efficient, as the required Fourier transforms may be computed using a Fast Fourier Transform (FFT) algorithm [46]. The method is limited to slab-like geometries, which nevertheless constitute an important range of practical optical components made of metamaterials, such as thin films and slab waveguides. In the next section, we apply the method to three kinds of metamaterials designed to exhibit unusual optical effects. The method's efficiency and versatility, and especially its capability to handle spatial dispersion, are essential to the study of such materials.

3 Functional propagation effects in spatially dispersive metamaterials

In this section we apply the methods of Section 2 to three different metamaterials designed to manipulate optical beams: a diffraction-compensating metamaterial (Section 3.1), a bifacially reflecting metamaterial (Section 3.2) and a polarization-converting metamaterial (Section 3.3). Spatial dispersion is at the core of the interesting and useful optical properties of these materials. We discuss the physical background of these properties and the rationale of the design, and proceed to study examples of propagation of optical fields through the materials and propose applications and future research directions for each.

3.1 Diffraction compensation in a metamaterial

Diffraction – a wave phenomenon that makes the propagation of light deviate from simple ray-like propagation [47] – is an unwanted effect in many situations. To name two, collimated optical beams diverge and sharp optical images blur and become distorted when they propagate through space. Diffraction of a single-mode laser beam can be eliminated by transversely confining its fields in a waveguide such as a single-mode optical fiber. In general, waveguides only have a fixed set of electromagnetic modes, so that arbitrary fields cannot be transferred through them. However, an array of waveguides can be used for such fields [48]. In some specially-designed media, a properly-shaped isofrequency **k**-surface can be used to compensate for the diffraction. In photonic crystals, the cancellation of optical diffraction is known as self-collimation, and it takes place near the Bragg reflection regime where the isofrequency surfaces are cubical or rectangular in shape [49, 50]. In the realm of metamaterials, flattened hyperbolic dispersion in arrays of metal wires [51] and metal-dielectric layer stacks [52] have been used for diffraction-free transfer of electromagnetic fields with subwavelength features. This is possible, because in these materials, **k**-surfaces theoretically extend to infinity. More recently, we have introduced diffraction-compensating metamaterials based on nanodiscs [18] and rectangular nanorods [19], which make the **k**-surface flat and, additionally, feature very low absorption and reflection losses. Proposed applications for diffractionless propagation of light include "perfect" imaging [52], integrated optical devices such as beam splitters [53], and new types of laser resonators [54].

Fundamentally, all diffractionless materials have a flat **k**-surface, as opposed to a spherical or ellipsoidal surface encountered in ordinary homogeneous materials. The flat **k**-surface ensures that for all plane waves (with any k_x and k_y), the longitudinal z-component of the wave vector is constant, k_{zc}. Optical energy will then propagate along the z-axis, which can point to any direction in the material. Consider the propagator $\overleftrightarrow{\mathbf{G}}$ of Eq. (51). Setting $k_z = k_{zc}$ in the propagator makes it constant for all plane waves at any given propagation distance, which indicates that a beam initially defined at $z = 0$ has the same angular spectrum and the phase distribution for the plane-wave components at any z. Then, according to Eq. (49), the intensity profile of the beam does not change upon propagation in the z-direction.

In terms of the isofrequency surface of the refractive index, the condition for diffraction cancellation can be written as $k_z = k_{zc} = k_0 n_0$ where n_0 is the refractive index for a plane wave with $\mathbf{k}$ directed along $\mathbf{z}$. Using the propagation angle $\theta = \arccos k_z/k$, perfect elimination of diffraction demands

$$n_{\text{eff}}(\theta) = \frac{n_0}{\cos\theta}. \tag{62}$$

It is more common to present isofrequency surfaces as functions of k_x, k_y and k_z, but since $k_{\text{tr}} = k_0 n(\theta)\sin\theta$ and $k_z = k_0 n(\theta)\cos\theta$ [Eq. (28)], the isofrequency surface of refractive index is isomorphic with the corresponding $\mathbf{k}$-surface.

Let us now consider an example of a diffraction-compensating metamaterial introduced by us in [19]. Figure 3a offers a three-dimensional view of the material structure. The material is composed of a tetragonal lattice of rectangular silver nanorods embedded in glass ($n = 1.5$). The rod dimensions are 30 nm in the transverse (x and y) directions and 130 nm in the longitudinal (z) direction. The lattice constants are $\Lambda_x = \Lambda_y = 120$ nm and $\Lambda_z = 200$ nm, and any interfaces with other materials are co-planar with the xy-planes. In order to fulfill Eq. (62), the material uses both anisotropy and spatial dispersion. The rods have a strong plasmon resonance in the longitudinal z-direction, which here is close to but blue-detuned from the operational wavelength of $\lambda_0 = 913$ nm. At normal incidence, the electric field of a plane wave is perpendicular to the z-axis and the interaction of the wave and the rods is weak, because the transverse plasmon resonances of the rods are at much shorter wavelengths. At a larger propagation angle, a TM-polarized plane wave will have an electric field with a larger z-directional component, which will excite a stronger electric dipole moment in each rod, increasing the refractive index. The lattice and rod sizes are tuned to make the $\mathbf{k}$-surface as flat as possible and to match the material's impedance to the impedance of glass. The general design methodology for these materials is detailed in [18].

Figures 3b and 3c show the isofrequency surfaces for TM-polarized waves given by the contours of the refractive index and wave impedance (polar plots of each quantity as functions of the propagation angle θ) calculated with the methods given in Section 2.3. The vacuum wavelength is $\lambda_0 = 913$ nm. The blue curves show the real part and the red curves the imaginary part of each quantity. Large propagation angles are blocked by white sectors as they are inaccessible for propagating waves incident from glass. We observe a wide flat part in the refractive index contour, and a very low imaginary part of n for small propagation angles [at $\theta = 0$, $\text{Im}\{n\} = 3\times10^{-4}$] corresponding to the $1/e^2$ absorption length for intensity of 480 µm. Because the contour of the real part of n is not perfectly flat and the imaginary part varies rapidly with θ, we expect the diffraction compensation effect to show some imperfections at longer propagation distances for fields with wide angular spectra. The impedance is well matched to glass impedance near normal incidence, which virtually eliminates reflection losses for all but the most obliquely incident plane waves. For TE polarization, the wave parameters (not shown) are, for all angles, very close to the TM-polarization parameters corresponding to $\theta = 0$. In general, one must consider three-dimensional isofrequency surfaces, but for the present material, the surfaces are symmetric around the z-axis.

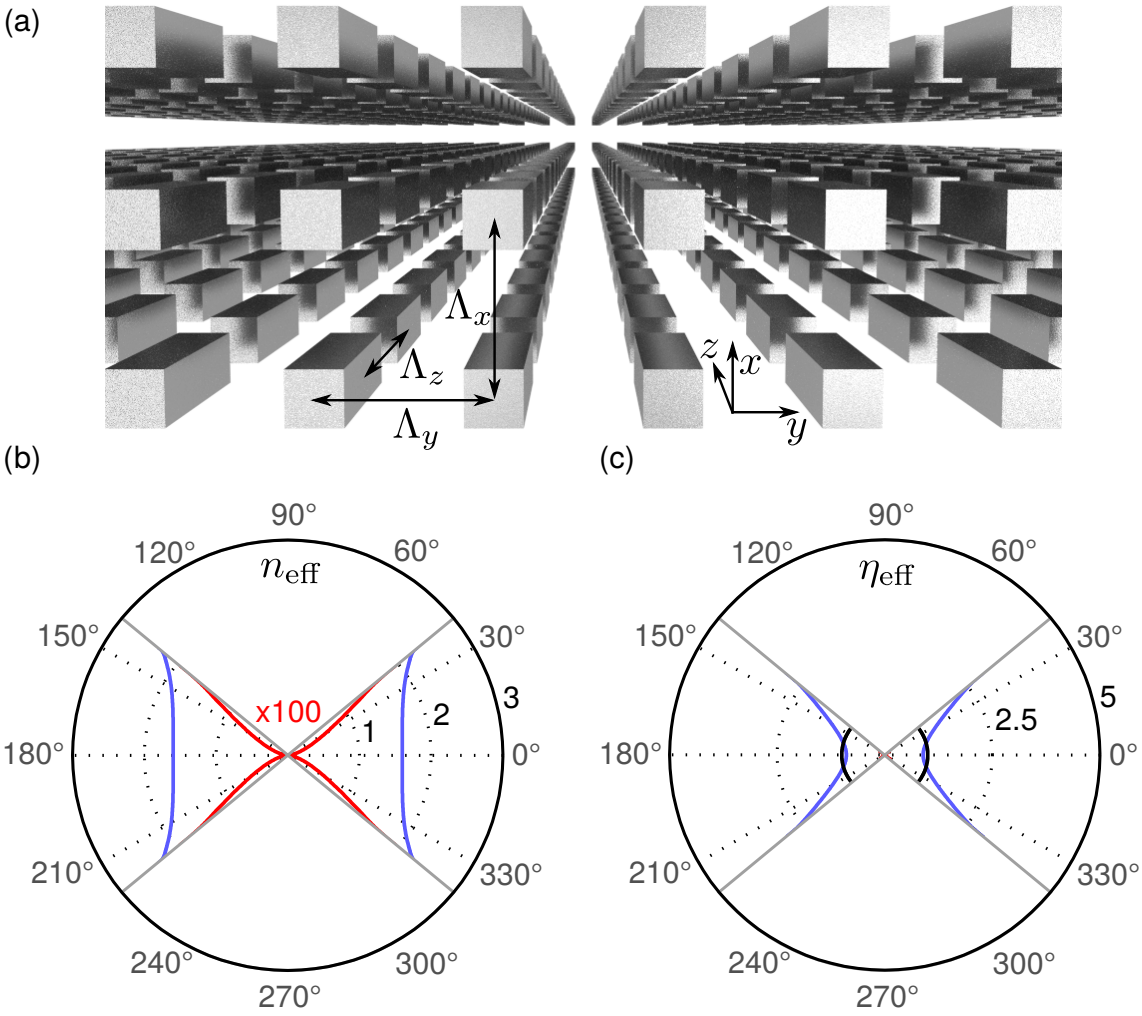

Figure 3: (a) The structure of the rod metamaterial consisting of rectangular silver rods in a lattice with $\Lambda_x = \Lambda_y = 120$ nm and $\Lambda_z = 200$ nm. (b) The refractive index as a function of propagation angle θ for TM-polarized plane waves. The real part is shown in blue and the imaginary part in red; in addition, the imaginary part is multiplied by 10 to make it more visible. The white sectors correspond to propagation directions not accessible from glass. (c) The normalized wave impedance as a function of θ, with the real part shown in blue and the imaginary part in red. The impedance is normalized to the impedance of glass, which is shown in black.

To illustrate the diffraction compensation effect, we use a purely TM-polarized optical beam. The radially polarized first-order Laguerre-Gaussian beam is a simple example, also known as the "doughnut beam" for its hollow shape. The electric field of the beam at the beam waist can be written as [29]

$$\mathbf{E}(x, y, 0) = E_0\sqrt{2e}\left(\frac{x}{w}\mathbf{x} + \frac{y}{w}\mathbf{y}\right)e^{-\frac{x^2+y^2}{w^2}}, \tag{63}$$

where E_0 is the maximum amplitude of the electric field at the beam waist, w is the beam waist radius ($E(w, 0) = \sqrt{2/e}E_0$) and $\mathbf{x}$ and $\mathbf{y}$ are the x- and y-directed

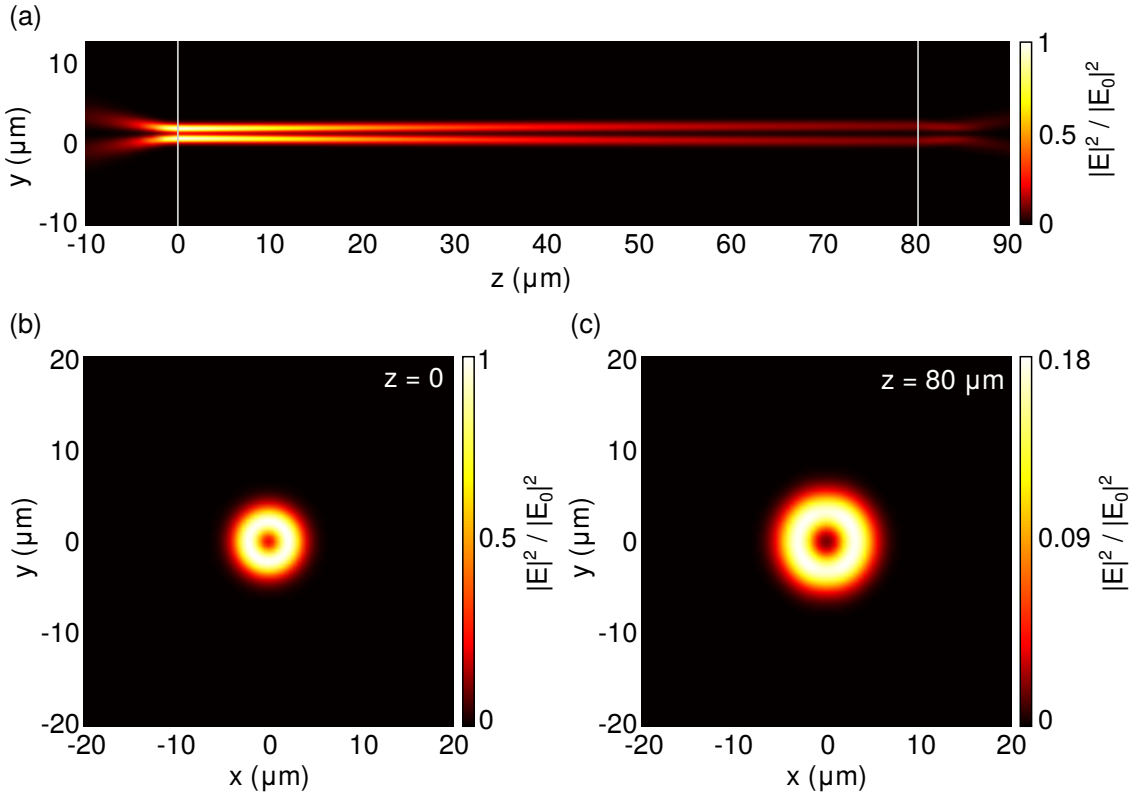

Figure 4: The propagation of a radially polarized beam through a slab of the designed diffraction-compensating rod metamaterial. All the plots show the field intensity, normalized to the intensity maximum on the focal plane at $z = 0$. In (a), the longitudinal cross section of the beam is shown. The white lines mark the slab interfaces. The beam propagates in the positive z-direction. Figures (b) and (c) show the intensity profiles at the input and output surfaces of the slab (at $z = 0$ and $z = 80\,\mu\text{m}$, respectively).

unit vectors. This beam has a divergence angle of approximately $1.5\lambda/(\pi w)$ [55]. Figure 4 shows the normalized intensity distributions of such a beam fired through a slab of the rod metamaterial. The beam propagates in the z-direction, has a waist radius of $w = 800$ nm and a divergence angle of 20°. The slab is 80 µm thick (400 metamolecular layers), and the medium outside it is glass with refractive index $n = 1.5$. Figure 4b shows the normalized intensity on the xy-plane at $z = 0$, which is both the focal plane and the slab input surface. Figure 4a shows the intensity on the yz-plane at $x = 0$, revealing how the beam propagates. The beam's divergence is almost completely eliminated inside the slab: essentially, the focal spot at $z = 0$ is transferred to $z = 80\,\mu\text{m}$. Because the electric field inside the slab is not accurately known in the effective medium picture, each point inside the slab in fact shows the output field from a slab of thickness z. Figure 4c shows the intensity distribution at $z = 80\,\mu\text{m}$ on the output surface of the slab. The beam has slightly expanded, because of absorption and imperfect diffraction cancellation, as we predicted from the isofrequency contour of the refractive index. However, if it had propagated the same distance in glass, the beam diameter would have expanded to 60 µm.

While the material only compensates for the diffraction of TM-polarized fields,

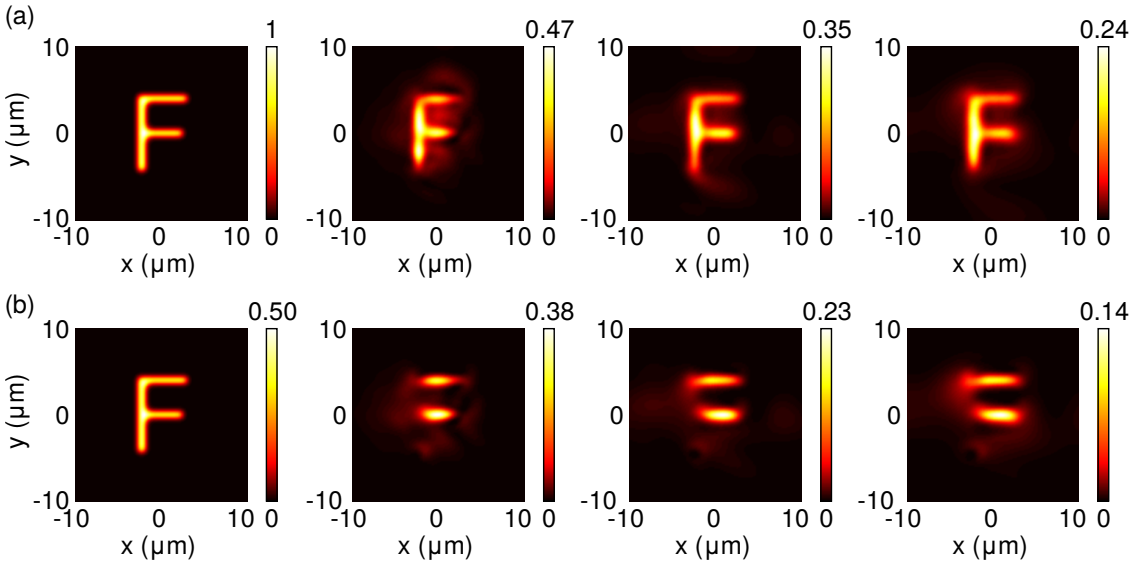

Figure 5: Propagation of an image of the letter F through a slab of the rod metamaterial. The first plot in the row (a) shows the incident intensity distribution, at $z = 0$, and the subsequent plots show the intensity distributions at $z = 30\,\mu\text{m}$, $60\,\mu\text{m}$, and $90\,\mu\text{m}$. The plots in the row (b) show only the intensity of the y-polarized component of the field, at the same z-coordinates as the corresponding plots in the upper row.

this does not limit its image-transfer capabilities to circularly symmetric, TM-polarized beams. In fact, the material can transfer *arbitrary* images, suppressing their diffraction. Consider, for example, an image of the letter F shown in Fig. 5a. If the field of the image has the same phase everywhere, the vertical (y-directional) line will preferably diverge in the horizontal (x) direction. If the image is linearly polarized along the vertical line, the line would be almost entirely TE-polarized, as it would mostly contain TE-polarized plane-wave components. In contrast, the horizontal lines would be TM-polarized. In order to have both TE- and TM-polarized fields everywhere in the image, we can use circularly-polarized or unpolarized light.

Figure 5 shows a circularly-polarized image of the letter F propagating through a slab of the designed rod metamaterial. The lines have a Gaussian transverse profile and are $1.6\,\mu\text{m}$ thick, while the whole letter is approximately $10\,\mu\text{m}$ tall. The first image in Fig. 5a (the upper row) shows the incident intensity distribution at $z = 0$, and the three subsequent images show the distributions at $z = 30\,\mu\text{m}$, $60\,\mu\text{m}$ and $90\,\mu\text{m}$. The letter F is discernible all the way, though at $z = 30\,\mu\text{m}$ a background field slightly obscures it until it disappears and a very clear image is left. In contrast, if the image was propagating in ordinary glass, the divergence would widen the lines up to $12\,\mu\text{m}$ at $z = 90\,\mu\text{m}$. Needless to say, the image would be unrecognizable.

Figure 5b (the lower row) shows the intensity of only the y-polarized component of the field. This component is approximately TM-polarized for the horizontal and TE-polarized for the vertical lines. Indeed, very little of the y-polarized field remains in the vertical line after propagation. The image has therefore become polarized such that it only consists of TM-polarized waves, while still preserving its original shape. Returning to Fig. 5a, we conclude that this will happen to any image upon

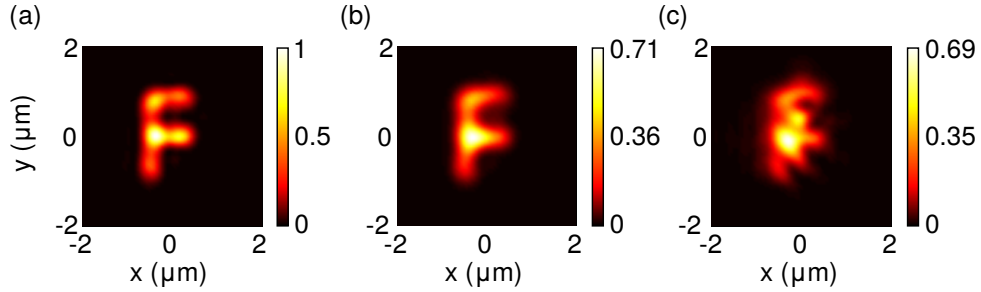

Figure 6: Propagation of a tightly-focused letter F through a two-layer slab of the rod metamaterial. The incident intensity distribution is shown in (a), while (b) shows the intensity after propagation through the slab. Subfigure (c) shows the image after propagation through a glass slab of the same thickness.

propagation over a distance of 100 µm or so in the material.

The example above highlights the low losses and the quality of diffraction compensation even at large distances. The image features are a few wavelengths in size, so the angular spectrum of the image is limited to $\theta < 20°$ in glass. At shorter distances, however, much better resolution can be maintained. Figure 6a shows another circularly-polarized image of the letter F, this time only 2.4 µm tall with 500 nm wide lines. The sharp features of the image are slightly obscured because its angular spectrum extends to evanescent waves which are removed from consideration already at $z = 0$. The image propagates through a 400 nm thick slab (two meta-molecular layers). Figure 6b shows the output image, in which the major features of the letter are clearly preserved. For comparison, Fig. 6c shows the image after propagating the same 400 nm distance in glass. The distortion is massive compared to the diffraction-compensated image transfer.

Diffraction-compensating metamaterials designed to have low absorption and reflection losses may be used for a number of applications. Image transfer is the most obvious one, as demonstrated by our examples. It can be used in both lithography and microscopy systems. The effect where a beam travels strictly in one direction in the material, independently of the incidence angle, may be used to overlap multiple beams and thus increase the information transfer capacity of a waveguide constructed of a diffraction-free material. In laser resonators the elimination of diffraction would allow better confinement and smaller "walk-off" effects. Using the constant-k_z materials, one can make anti-reflection or high-reflection coatings work independently of the incidence angle of incoming radiation, if some other conditions are also satisfied [56]. Later in this thesis, we will investigate the prospect of collimating the emission of light by point sources embedded in a diffraction-compensating metamaterial.

3.2 Bifacial and spatially filtered reflection by a metamaterial

Bifacial metamaterials allow the impedance to differ for two waves propagating in the opposite directions. One consequence of this is that a film of such a material, placed inside an isotropic medium, will reflect different amounts of light from its different sides. This is seen from Eq. (61). Exchanging the direction means swapping

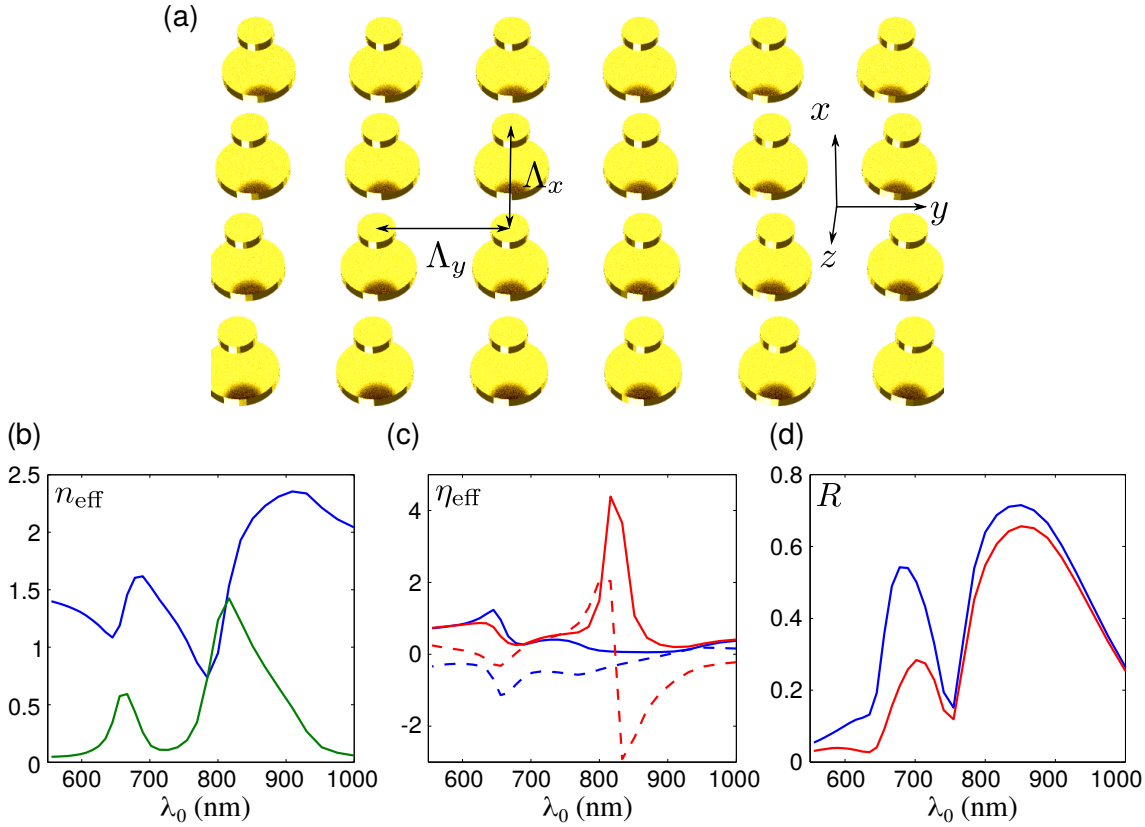

Figure 7: (a) The structure of one metamolecular layer of the bifacial gold-dimer metamaterial with lattice constants $\Lambda_x = \Lambda_y = 180$ nm. (b) The spectrum of the material's refractive index for normally-incident plane waves. The real part is shown in blue and the imaginary part in green. (c) The normalized impedance spectrum for waves propagating in the positive (red lines) and negative (blue lines) z-directions, with real parts shown by solid lines and imaginary parts by dashed lines. (d) The reflectance spectra, with red and blue lines showing the reflectance for positive and negative z-directions, respectively.

indices 12 with 32 and 23 with 21. If the slab is bifacial, the Fresnel coefficients are different and so are the reflection coefficients. Furthermore, metamaterials also allow the wave impedance to be different not only for counterpropagating waves but also waves at propagating at different directions. One can then design a metamaterial that will reflect waves incident on the material at small angles and transmit others. These properties can be used to create bifacial mirrors and ultrathin spatial filters. In the following we will construct a bifacial metamaterial and show that it can be tuned to strongly exhibit reflection effects described above.

Let us consider a metamaterial composed of gold metamolecules, each consisting of two nanodiscs of different size. We call these molecules *metadimers*. Figure 7a illustrates the structure of a single layer of these metamolecules. The rotational symmetry axis of each discs is directed along the z-axis. The diameters of the discs in each dimer are 110 nm and 55 nm, their thickness is 15 nm and the surface-to-surface separation is 70 nm. The lattice is cubic, and the lattice constants are $\Lambda_x = \Lambda_y = \Lambda_z = 180$ nm. As the distance between the discs of each dimer is fairly

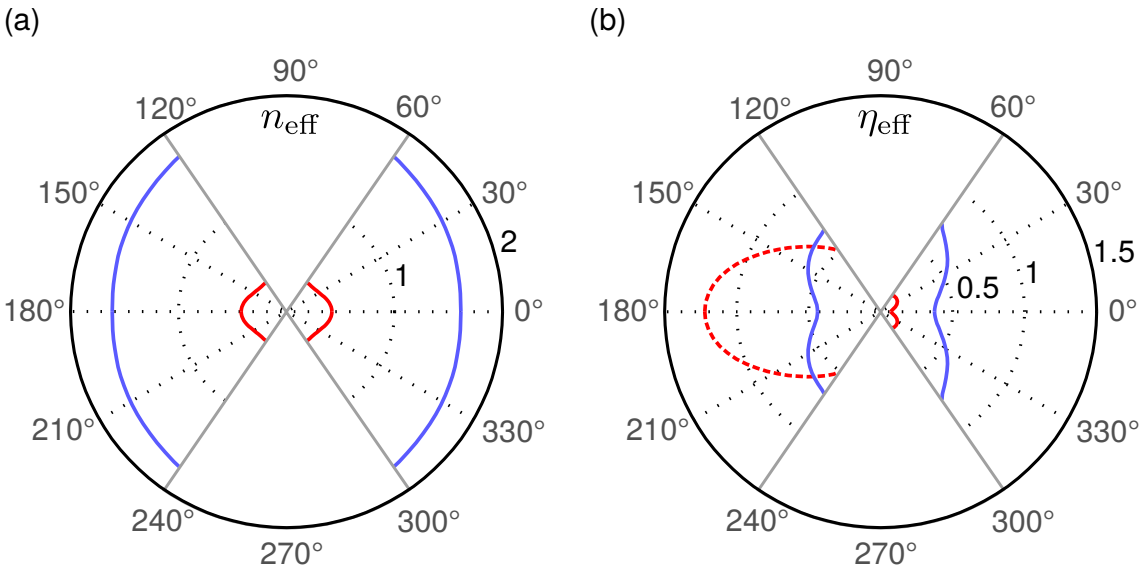

Figure 8: The refractive index (a) and normalized impedance (b) of the gold-dimer metamaterial as functions of the propagation angle θ at $\lambda_0 = 680$ nm for TE-polarized waves. The blue curves show the real parts and the red curves the imaginary parts of the quantities. The white sectors correspond to propagation angles not accessible for waves incident from glass. A dashed line corresponds to a negative value of $\text{Im}\{\eta_{\text{eff}}\}$.

large, a wave propagating along **z** excites the discs at different phases. This creates a combined dipole-quadrupole excitation, which can scatter different amounts of optical energy into the small-disc and large-disc directions [27, 57], making the material bifacial.

Figure 7b shows the refractive index spectrum for normally incident plane waves, with the real/imaginary part presented by the blue/green line (the refractive index of gold used in the calculation was taken from [58]). The plasmonic resonances of each of the two discs are clearly seen as two peaks in the imaginary part of n_{eff}. Figure 7c shows the normalized impedance spectra for waves propagating in the positive (red lines) and negative (blue lines) z-directions. The real/imaginary part of η_{eff} is shown by the solid/dashed line. Figure 7d shows the reflectance (R) spectra of a material slab calculated for waves propagating in the positive and negative z-directions (red and blue curves, respectively). The slab consists of two metamolecular layers and is surrounded by glass. We find a remarkable difference in the reflections, e.g., at $\lambda_0 = 680$ nm where the reflectance is 54 % for the negative and 21 % for the positive z-direction of wave propagation. Figure 8 shows the wave parameters n_{eff} and η_{eff} as functions of the propagation angle θ at this wavelength for TE polarization. While the refractive index in Fig. 8a is rather isotropic in both the real (blue) and imaginary (red) parts, the impedance shown in Fig. 8b varies significantly with θ. For example, the imaginary part of η_{eff} is 0.05 at $\theta = 0$ and -0.8 at $\theta = \pi$.

To witness the unequal reflections, we let two Gaussian beams propagate through a two-layer thick slab of the material in opposite directions. The beams are x-polarized. The beam waist radius is $w = 1.6\,\mu$m. We extend each beam in the x-direction to infinity to make them completely TE-polarized. The incidence plane of each beam is

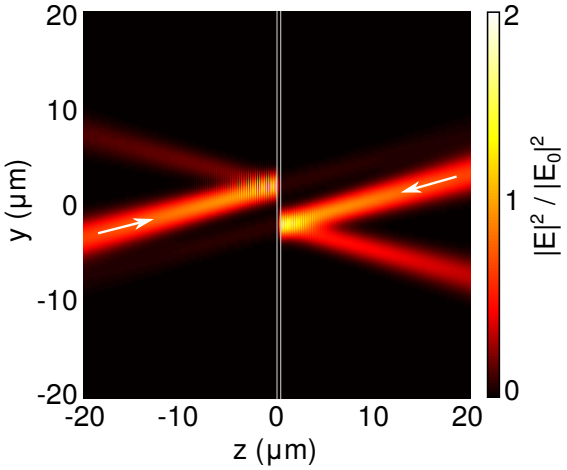

Figure 9: Intensity distribution of two Gaussian beams interacting with a slab of the bifacial dimer metamaterial. The slab has two layers (the vertical gray lines show its interfaces). The intensity is normalized to the maximum of the incident beam intensity.

the yz-plane, the incidence angle is 15 degrees and the divergence angle is 7 degrees. Figure 9 shows the beam intensity on the yz-plane, with the slab designated by the vertical gray lines. We see that the reflected beam on the right side of the slab is much more intense than the beam on the left. The reflected beam powers are 50 % and 20 % of the incident power for the right and left beams, respectively. The transmitted beams are also present but weak, carrying only 7 % of the incident power, chiefly due to the high absorption at this wavelength.

The impedance and hence the reflectance of the bifacial material vary rather slowly with the incidence angle. In order to show a reflective spatial-filtering effect, we can make the spatial dispersion more prominent by changing the lattice. We increase the unit cell size, picking $\Lambda_z = 220$ nm, and calculate the reflectance spectra for waves incident from glass at the incidence angles 0 and 20°. Figure 10a shows the reflectance spectra of an eight-layer metamaterial slab for waves propagating in the positive z-direction (solid lines) and the negative z-direction (dashed lines). The blue lines show the reflectance at $\theta = 0$ and the red lines show R at $\theta = 20°$. Searching for a large difference in the $\theta = 0$ and $\theta = 20°$ reflectances, we find a promising difference around $\lambda_0 = 728$ nm, where R is higher at normal incidence. Figures 10c and 10d show the refractive index and impedance calculated for TE-polarized waves at this wavelength as functions of the *incidence* angle. The real parts are shown by blue lines and the imaginary parts by red lines. The refractive index stays close to 1.5 at all incidence angles, but the impedance varies significantly. It has a large imaginary part at normal incidence for both the left- and right-going waves. At large angles the imaginary part becomes smaller, bringing the impedance closer to that of glass. Finally, Fig. 10b shows the reflectance of the slab as a function of the incidence angle. As predicted, the reflectance is high for a range of angles near normal incidence, until it sharply drops at around 15°.

Figure 11a shows the intensity distribution of a Gaussian beam focused onto a metamaterial slab containing 8 metamolecular layers. The beam is two-dimensional

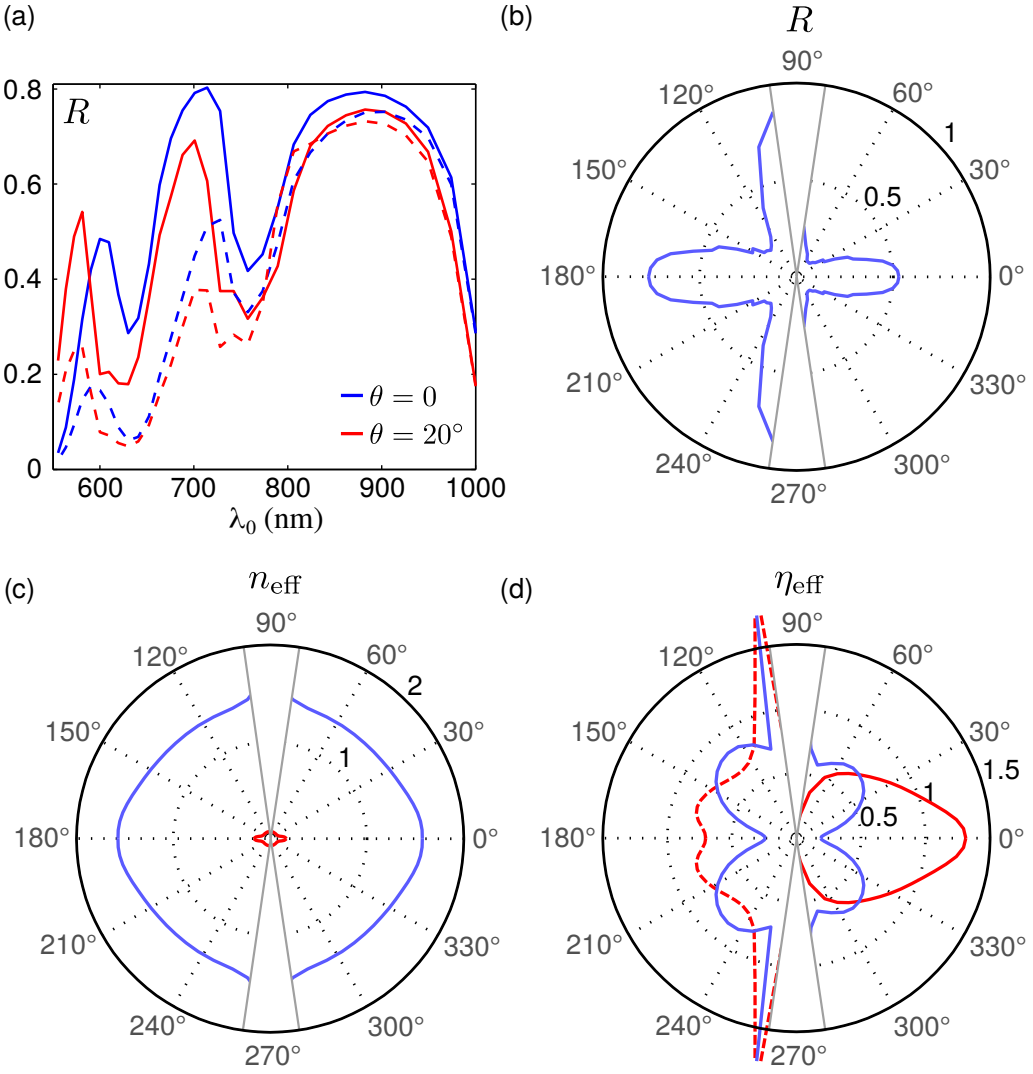

Figure 10: (a) The reflectance spectra of a slab of the modified ($\Lambda_z = 220$ nm) dimer metamaterial for TE-polarized waves. The slab contains 8 metamolecular layers. Solid/dashed lines show the reflectance for waves propagating in the positive/negative z-direction with the incidence angles of 0 and 20° (blue and red curves, respectively). (b) The reflectance as a function of incidence angle from glass at $\lambda_0 = 728$ nm. (c) The refractive index n_{eff} as a function of the incidence angle, with the real and imaginary parts shown by the blue and red lines, respectively. (d) The normalized impedance η_{eff} as a function of the incidence angle, the blue and red lines showing the real and imaginary parts, respectively. A dashed line corresponds to a negative value of $\text{Im}\{\eta_{\text{eff}}\}$.

(extended to infinity in the x-direction) and entirely polarized along $\mathbf{x}$. The beam divergence angle is 60°. The reflected beam is not present in this picture: instead, it is shown in Fig. 11b. The profile of the beam is drastically modified by the reflection. The divergence angle is reduced to approximately 30°, which shows that the large-angle plane waves have been removed. Indeed, these waves form the hollow transmitted beam seen in Fig. 11a.

A slab of a bifacial metamaterial can be impedance-matched to two different

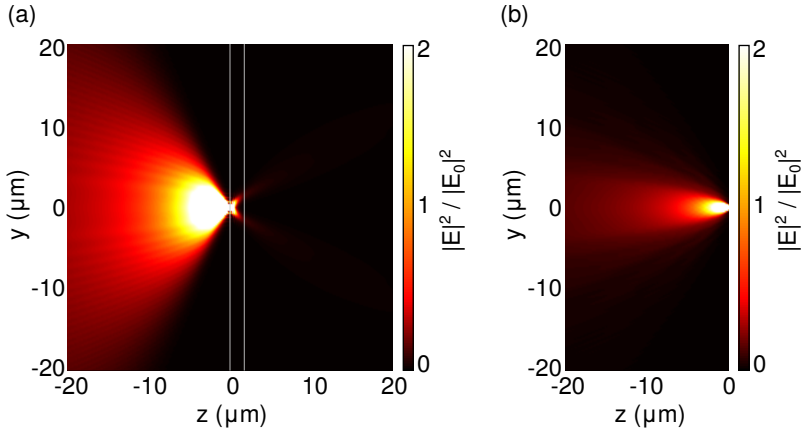

Figure 11: A Gaussian beam interacting with a slab of the modified dimer metamaterial. The divergence angle of the incident beam is 60° and the beam propagates in the positive z-direction. Subfigure (a) shows the intensity of the incident and transmitted parts of the beam, while subfigure (b) shows the reflected, spatially filtered part. The intensity is normalized to the maximum intensity at $z = -20\,\mu\text{m}$.

media on its left and right sides for waves incident on the slab. Such slabs could be used as, e.g., intracavity mode filters in lasers: because of the impedance matching, the reflections can be eliminated from both the substrate and air sides despite the material being absorptive. The angle-sensitive reflection effect may lend itself to other uses. For example, a spatial filter for optical beams in the form of a metamaterial film will function independently of the position of the beam focus, in contrast to conventionally used lens-pinhole systems [47]. Other metamaterial filters could be used to efficiently produce hollow beams. Finally, the highly tunable transmission and reflection characteristics can be useful in the design of light sources with shaped and directional emission patterns. This possibility will be explored later in this thesis.

3.3 Polarization conversion of light in a metamaterial

Control of the polarization of light is essential in all optical systems. The class of metamaterials most closely associated with this task are the chiral metamaterials [7]. Using rotationally asymmetric metamolecules such as L-shaped particles or gammadions, chiral optical metamaterials have been demonstrated to exhibit, e.g., strong polarization rotation [59, 60] and asymmetric transmission in opposite illumination directions [61]. These metamaterials can also act similarly to more common optically active media [33]. They provide an alternative way for realizing negative refraction, though this is a difficult task at optical frequencies [62].

Aside from chiral metamolecules, spatial dispersion itself can be responsible for polarization conversion. We have shown this in [26]. A single metamolecular layer of the material used for this purpose is depicted in Fig. 12. The material consists of silver nanodiscs with a radius of 30 nm and a thickness of 20 nm embedded in glass. The discs make a 45° angle with respect to the x- and y-axes. The TE and TM polarizations are only conserved for plane waves with their wave vector in one

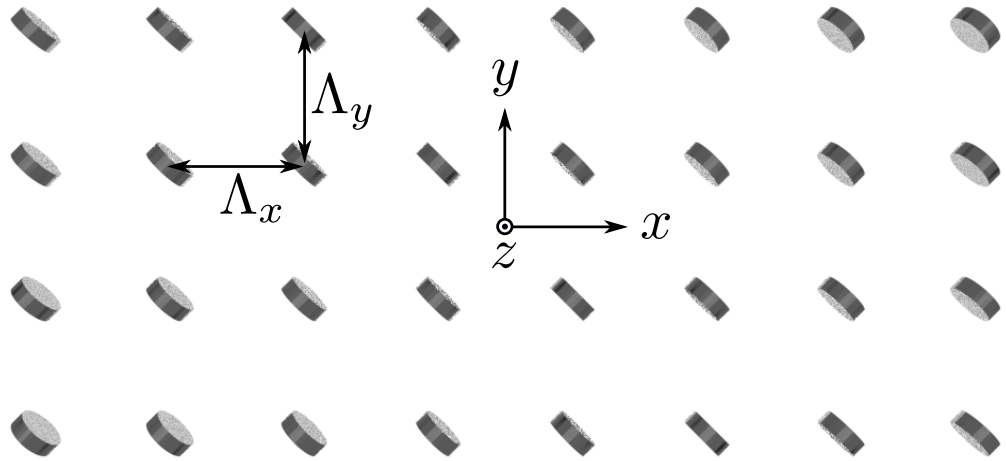

Figure 12: One metamolecular layer of the polarization-converting rotated-disc metamaterial. The discs are made of silver. The transverse lattice constants are $\Lambda_x = \Lambda_y = 120$ nm. The longitudinal one (not shown) is $\Lambda_z = 180$ nm.

of the reflection-symmetry planes of the discs. In other incidence planes, they are not conserved because then the electric field of a wave is not aligned with the discs and can be unequally scattered and absorbed. The metamaterial does not even have polarization modes for all plane waves, and is therefore best described using the transfer matrix approach described in Section 2.3 instead of the wave parameter-based interferometric approach utilized in the previous sections. Figures 13a and 13b show

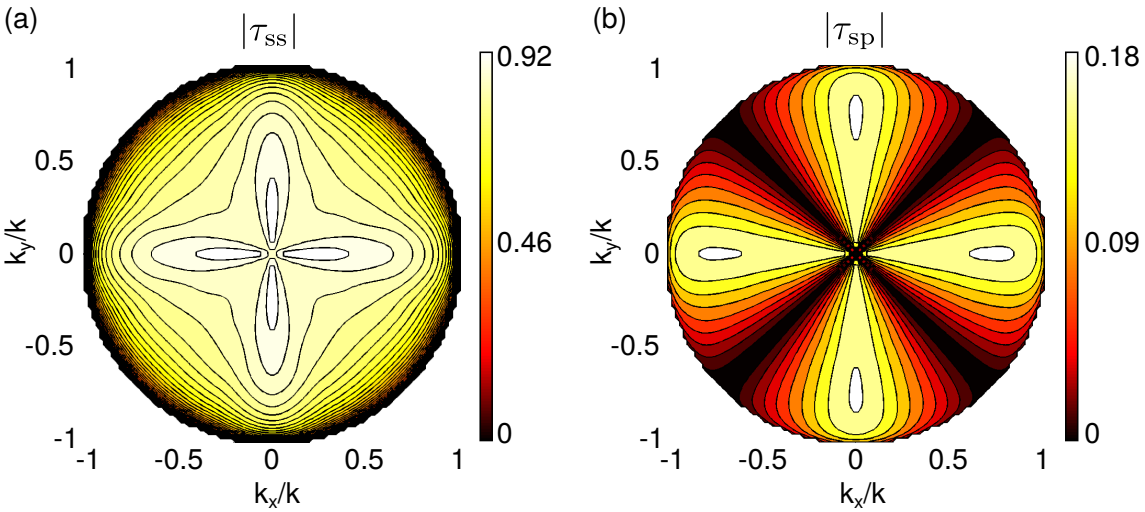

Figure 13: The absolute values of the transmission matrix elements (a) τ_{ss} and (b) τ_{sp} of a metamolecular layer of the rotated-disc metamaterial of Fig. 12, shown as functions of the transverse components of the wave vector, k_x and k_y. Contour lines are drawn in step of 0.02.

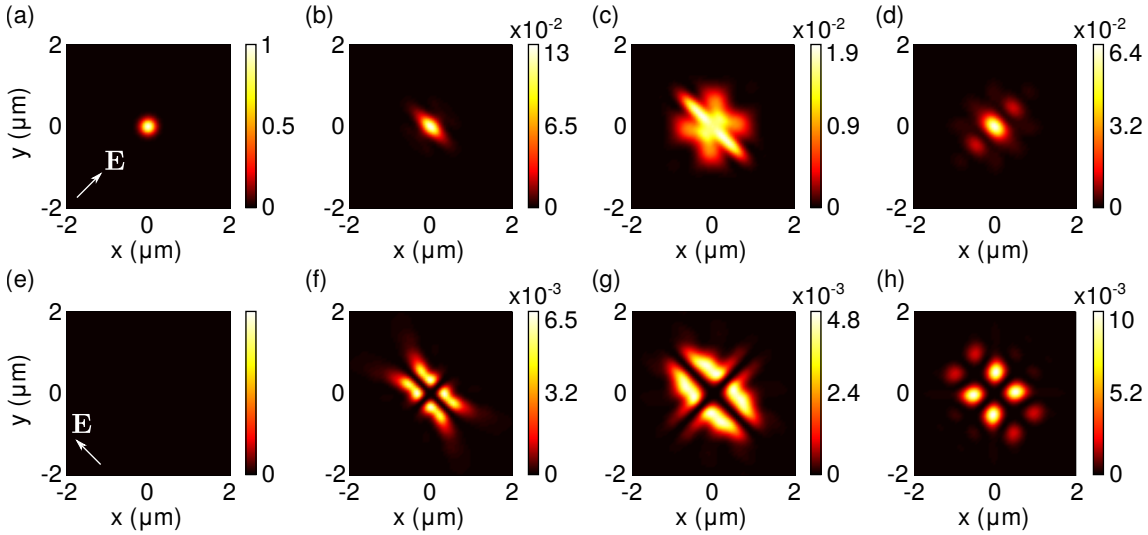

Figure 14: Propagation of a Gaussian beam ($w = 260$ nm) through a 16-layer slab of the rotated-disc metamaterial. The intensity distribution of the incident field polarized along the disc axes ($\mathbf{x} + \mathbf{y}$) is shown in (a). The plots (b) and (c) show the intensity profiles of this component after propagation through 8 and 16 layers, respectively, and (d) shows the intensity at a 1.4 µm distance from the slab exit surface. On the lower row, (e) shows the intensity of the perpendicular electric-field component ($\mathbf{x} - \mathbf{y}$), which is absent in the incident beam. It appears in (f), (g) and (h) corresponding to the same propagation distances as in (b), (c) and (d).

the absolute values of the transmission matrix elements τ_{ss} and τ_{ps}, respectively, as functions of the transverse wave-vector components k_x and k_y, for wavelength $\lambda_0 = 633$ nm. For the planes rotated 45° from the xz-plane, the material preserves the incident polarization as $\tau_{sp} = 0$. For these planes, the TE and TM polarizations have their electric-field vector directed along and normal to the discs. The TM-to-TE polarization conversion takes place at all other angles: $|\tau_{sp}| = 0.18$ at the highest. A single layer of metamolecules therefore converts approximately 3 % of the incident power to an orthogonal polarization. The power conversion is exactly the same for the TE-to-TM conversion direction (not shown in the figure). At most, 15 % of the power will be absorbed by a single layer, though this varies significantly with the incidence plane and angle.

As the conversion effect is dependent on the plane-wave incidence angle, an initially uniformly polarized beam propagating through a slab of this material will have parts of its angular spectrum converted to the orthogonal polarization. Figure 14 shows an example of a Gaussian beam focused on a 2.9 µm thick, 16-layer slab of the metamaterial. The beam is polarized along the rotational-symmetry axes of the discs (along $(\mathbf{x} + \mathbf{y})/\sqrt{2}$), has a divergence angle of 30° and a beam waist radius of 260 nm. Figures 14a–14d show cross sections of the intensity distribution of the incident polarization component at (a) the entrance surface of the slab, (b) the center of the slab, (c) the exit surface of the slab, and (d) at a 1.4 µm distance from the exit surface. Figures 14e–14h show the intensity of the orthogonal polarization component at the same four locations. The orthogonal component grows stronger as the beam

travels through the slab. Some parts of the beam's transverse profile are converted but others remain unchanged. At the end, approximately 6 % of the incident power has been converted to the orthogonal polarization, and the output beam is rather complex in shape. Also, comparing Figs. 14c and 14d, we notice that the beam is slightly focused after leaving the slab, another effect caused by spatial dispersion.

The transfer-matrix method proves essential here, as it is capable of simulating the beam-metamaterial interaction even when no effective wave parameters can be introduced for all relevant plane waves. Various effects can lead to the absence of polarization modes, including anisotropic scattering and absorption and the appearance of higher-order multipoles in metamolecules. These effects are both possibilities and challenges: they can provide new degrees of freedom in the design of metamaterials but complicate the description of the material response, a problem solved by the transfer-matrix approach.

4 Quantum emitters in metamaterials

Most sources of light are quantum-mechanical systems. Fluorescent molecules, for example, have discrete quantum states, and transitions between some of these states are accompanied by emission or absorption of light photons at certain frequencies. Often, quantum emitters are not isolated from their surroundings, which can modify their states and transition characteristics. Remarkable modifications can be made by placing the emitters in a microcavity or near a metal nanoparticle, such as a metamolecule. Even if the quantum states are not perturbed much by such structures, the distribution of electromagnetic modes into which the emitter can radiate can be modified, and the temporal and spatial characteristics of emission can be changed drastically. Most significantly, modification of the local density of these modes is responsible for the Purcell effect, that is, the increase or decrease of the spontaneous emission rate of an emitter [29].

The Purcell effect, directional emission and other associated phenomena are studied in a wide variety of environments and devices, including nanoantennas and plasmonic particles [28, 63–65], photonic crystal microcavities [66] and metamaterials [11]. In metamaterials, numerous studies have concentrated on hyperbolic metamaterials [6, 10, 67]. In theory, the isofrequency surfaces of the **k**-vector in these materials are infinitely extended, which leads to an infinite amount of available electromagnetic modes and thus massive enhancement of spontaneous emission. In practice, the emission enhancement factor does not exceed 10 for emitters placed on top of hyperbolic metamaterial slabs or inside them because of absorption and the associated quenching of fluorescence [10]. Zero-index metamaterials, on the other hand, have been proposed and, to some extent, demonstrated to control the wavefronts of quantum emitters and force them to radiate in phase with each other [13, 68]. As a final example, metamaterials providing field confinement such as split-ring resonator-based materials have been used to demonstrate lasing surface-plasmon amplifiers where emitters are coupled to a metasurface that acts as a resonator [14, 69].

In this section, we briefly summarize the quantum-mechanical description of spontaneous emission and the connection between quantum and classical electrodynamics. We then introduce a semi-analytical method to compute the electromagnetic fields created by emitters modelled as electric dipoles, embedded in a general spatially dispersive metamaterial. The method is based on the beam propagation method introduced in Section 2.4 and the material is described using the wave parameters. We also determine far-field emission patterns inside a spatially dispersive metamaterial, in order to reveal their energy-transfer properties.

4.1 Quantum emitters and dipole approximation

Near-resonant interaction of a quantum-mechanical system with light can often be described in terms of only two discrete quantum states 1 and 2, with energies E_1 and E_2, respectively [70]. The lower energy level 1 is that of the ground state, in which the system preferably resides, while the higher level 2 belongs to the excited state. By near-resonant interaction with other systems, a “two-level” emitter can

decay from level 2 to level 1, transferring the excess energy $E_2 - E_1$ to some of these systems. Conversely, an excitation of the emitter by another system is accompanied by a transition from level 1 to level 2 and the absorption of energy $E_2 - E_1$. In optics, we are often interested in radiative excitation and decay processes, in which the system absorbs and emits photons, respectively. Emission, furthermore, can be spontaneous or stimulated. Spontaneous emission is a radiative decay of the system, induced by interaction with the surrounding electromagnetic vacuum, while stimulated emission is caused by the interaction with photons [71].

Fermi's golden rule states that the rate of spontaneous emission is proportional to the number of the modes into which the emitter can radiate, i.e., the *local density of states* [29], and this is responsible for the Purcell effect. This description is valid in the so-called weak coupling regime, where photons emitted by the system are not absorbed back by it. When a photon can be transferred back and forth between the emitter and an external system, they are said to be *strongly coupled*. Weak coupling does not perturb the quantum states of the emitter, while strong coupling does [72]. In the absence of strong coupling, emitters are characterized by their unperturbed parameters found in tables [33].

Real quantum emitters are never two-level systems, but instead, have a large number of energy levels or bands. When the emitter is *pumped* to one of the excited states, it can decay non-radiatively to another state before emitting a photon. However, the emission process itself can often be studied in terms of the two-level system, since usually only two levels participate in any single transition at a time. Furthermore, since typical quantum emitters are small in size, only a dipole excitation appears when they interact with an optical field, and so most radiative transitions are dipole transitions [29]. Hence, a quantum emitter can be modelled in terms of classical mechanics as an oscillating electric dipole, and its coupling to the environment can be described by Maxwell's equations. The dipole in question, however, is characterized by the quantum-mechanical transition dipole moment and the transition frequency [29]. The description is therefore called semiclassical.

We now define two quantities characterizing the changes of the spontaneous emission rate. The first is the Purcell factor

$$\mathcal{P}_\mathrm{h} = \frac{\Gamma}{\Gamma_\mathrm{h}}, \tag{64}$$

where Γ is the spontaneous emission rate and Γ_h is the rate for the same emitter in a host medium (hence the subscript h). This is slightly different from the usual definition, as the factor is normalized to the emission rate in a homogeneous host medium instead of vacuum. A Purcell factor $\mathcal{P}_\mathrm{h} > 1$ indicates that emission rate is enhanced by the environment. When a narrowband transition is considered, all emitted photons have the same energy, and the Purcell factor may also be written as the ratio of the total power radiated by the corresponding time-harmonic electric dipole to the power of the same dipole in the host medium (see Section 4.3) [29]. If the dipole is located in an absorbing medium or close to absorbing particles, such as plasmonic nanostructures, some fraction of the emitted photons will be coupled to the decaying modes and will not be detected in the far field. Therefore, we also

define the emission enhancement factor

$$\mathcal{E} = \frac{\Gamma_{\mathrm{rad}}}{\Gamma_{\mathrm{h}}}, \tag{65}$$

where Γ_{rad} is the rate of spontaneous emission into propagating electromagnetic modes. For narrowband transitions the emission enhancement factor may be computed as the far-field power divided by the power in the host medium. While $\mathcal{P}_{\mathrm{h}}$ and $\mathcal{E}$ characterize the rates, often we will also be interested in the quantum yield

$$\mathrm{QY} = \frac{\Gamma_{\mathrm{rad}}}{\Gamma} = \frac{\mathcal{E}}{\mathcal{P}_{\mathrm{h}}}, \tag{66}$$

which is the fraction of all created photons emitted into the far field. Quantum yield therefore characterizes the conversion efficiency of the emitter.

To characterize the directionality of the emission, we introduce *directivity*, which can be calculated from the Poynting vector on some sphere of radius r centered on the antenna-emitter system,

$$D(\theta,\varphi) = \frac{\hat{\mathbf{S}}(\theta,\varphi)\cdot\mathbf{r}/r}{P_{\mathrm{tot}}} 4\pi r^2 = \frac{I(\theta,\varphi)}{P_{\mathrm{tot}}} 4\pi, \tag{67}$$

where P_{tot} is the total radiated power and $I(\theta,\varphi)$ is the radiant intensity with units of power per solid angle. The first form of the definition is more useful in practice, while the second form shows this is really a quantity independent of any chosen r. For an isotropic emitter $D = 1$ and for a dipole emitter $D = 1.5$. In general, when a multi-level quantum emitter is excited, its dipole moment will be randomly oriented. Therefore we must compute directivity and emitted power for, e.g., three orthogonal dipole directions separately and averaging the results.

4.2 Electric current decomposition method for optical sources

As outlined above, optical fields are in most cases produced by oscillating electric dipoles. In the frequency domain, determining these fields for any particular emitter is equivalent to finding Green's functions in the medium or structure surrounding the emitter. The dipole emission problem has been previously solved analytically for homogeneous and isotropic media [29] as well as layered and optically anisotropic media [73–77]. These methods typically rely on solving Maxwell's equations through expansion into a series of elementary waves, such as plane waves or spherical waves. In metamaterials, however, direct numerical ("full-wave") solutions, e.g., by the finite difference time domain method (FDTD) or the finite element method (FEM) are more usual (see, e.g., [21] for an overview). This is due to the need to model the complex internal structure of the medium, and the difficulty of retrieving suitable effective parameters for it. The main drawback of using full numerical simulations is the time-consuming computational effort. We will now introduce a semi-analytical method to solve the dipole emission problem in an arbitrary spatially dispersive medium characterized by the wave parameters $n_{\mathrm{eff}}(\mathbf{k})$ and $\eta_{\mathrm{eff}}(\mathbf{k})$ introduced in Section 2.

This method is, in fact, more general as it can be used to model *any* kind of emitter that can be modelled as a distribution of electric current in a plane. Throughout this section, we will consider time-harmonic fields with the time dependence given by $e^{-i\omega t}$, as previously.

An oscillating electric dipole can be treated as an infinitesimally short element of electric current [29]. For a dipole located in the origin of a chosen coordinate system the complex amplitude of the current density is

$$\hat{\mathbf{J}} = \mathbf{J}_0 \delta(\mathbf{r}), \tag{68}$$

where $\mathbf{J}_0$ is the current-element amplitude of the dipole measured in units of $\mathrm{A} \cdot \mathrm{m}$ and $\delta(\mathbf{r})$ is the three-dimensional Dirac delta function. Spatial integration over the current density shows that the current-element amplitude is equal to the electric current dipole moment, which has the magnitude Id, where I is the electric current amplitude and d the length of the dipole. Transition dipole moments are usually expressed as electric dipole moments $p = qd$, where q is the electric charge of the dipole. For a dipole oscillating at frequency ω, the connection between the electric and current dipole moments is $J_0 = -i\omega p$.

Analogously to the plane-wave decomposition of Section 2.4, a distribution of surface electric current $\hat{\mathbf{K}}(x, y)$ at $z = 0$ (corresponding to the current density $\hat{\mathbf{J}}(x, y)\delta(z)$ where $\mathbf{J}$ is in the plane), may be expressed as a sum of sinusoidally-varying waves of electric current,

$$\hat{\mathbf{K}}(x, y) = \frac{1}{(2\pi)^2} \int_{-\infty}^{\infty} \int_{-\infty}^{\infty} \tilde{\mathbf{K}}(k_x, k_y) e^{i(k_x x + k_y y)} dk_x dk_y, \tag{69}$$

where k_x and k_y are the spatial frequencies of the current waves and $\tilde{\mathbf{K}}(k_x, k_y)$ is the current wave amplitude that can be obtained from the Fourier transform

$$\tilde{\mathbf{K}}(k_x, k_y) = \int_{-\infty}^{\infty} \int_{-\infty}^{\infty} \hat{\mathbf{K}}(x, y) e^{-i(k_x x + k_y y)} dx dy. \tag{70}$$

The surface current density corresponding to Eq. (68) is $\hat{\mathbf{K}}(x, y) = \mathbf{J}_0 \delta(x)\delta(y)$, and its Fourier transform is a constant, $\tilde{\mathbf{K}}(k_x, k_y) = \mathbf{J}_0$. The reason for making this decomposition is that current waves emit plane waves with the same transverse spatial frequencies k_x and k_y. One plane wave is emitted on each planar current wave. If the wave parameters for these optical waves are known, we can determine the electric-field amplitudes of the waves by using the electromagnetic boundary conditions. This will give us the angular spectrum of the plane waves emitted by the dipole.

To this end, we further decompose the electric-current waves into the waves emitting transverse-electric and transverse-magnetic fields. The unit vectors for the TE and TM currents are, respectively,

$$\mathbf{t}_{\mathrm{J}}(\mathbf{k}_{\mathrm{tr}}) = \frac{\mathbf{k}_{\mathrm{tr}} \times \mathbf{n}}{|\mathbf{k}_{\mathrm{tr}} \times \mathbf{n}|} \text{ and} \tag{71}$$

$$\mathbf{m}_{\mathrm{J}}(\mathbf{k}_{\mathrm{tr}}) = \mathbf{t}_{\mathrm{J}}(\mathbf{k}_{\mathrm{tr}}) \times \mathbf{n}, \tag{72}$$

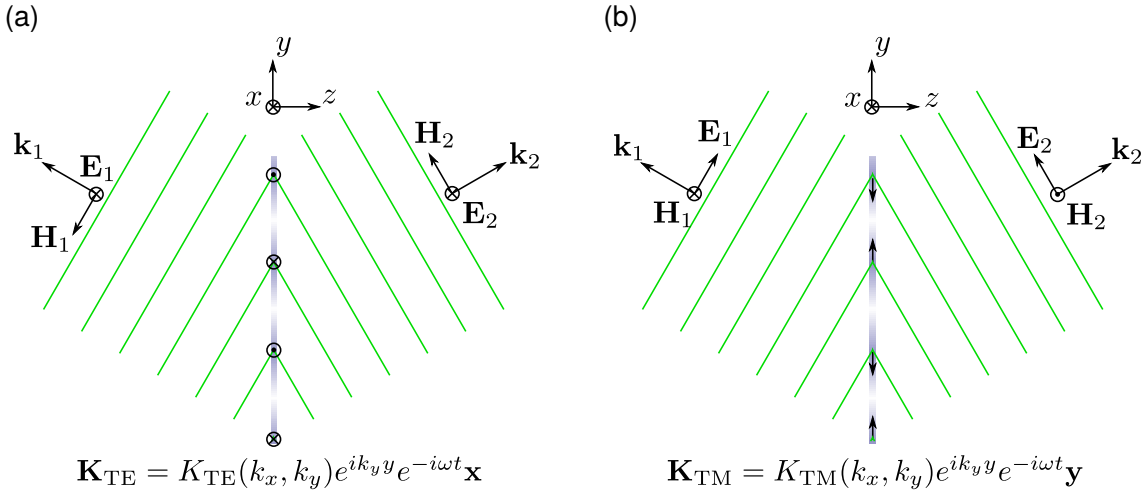

$\mathbf{K}_{\mathrm{TE}} = K_{\mathrm{TE}}(k_x, k_y)e^{ik_y y}e^{-i\omega t}\mathbf{x}$ $\mathbf{K}_{\mathrm{TM}} = K_{\mathrm{TM}}(k_x, k_y)e^{ik_y y}e^{-i\omega t}\mathbf{y}$

Figure 15: Optical plane waves (wavefronts shown in green) emitted by an electric-current wave on the xy-plane at $z = 0$. In (a) the currents are x-directional and generate TE-polarized waves, while in (b) they are y-directional, generating TM-polarized waves. In each case, the wave sent to the positive z-direction has a wave vector $\mathbf{k}_2$, electric field $\mathbf{E}_2$ and magnetic field $\mathbf{H}_2$, while the wave sent to the negative z-direction is characterized by $\mathbf{k}_1$, $\mathbf{E}_1$ and $\mathbf{H}_1$.

where $\mathbf{k}_{\mathrm{tr}}$ is the transverse wave vector with spatial frequencies k_x and k_y, and $\mathbf{n}$ is the surface normal of the xy-plane. The TE and TM current wave amplitudes are then

$$\tilde{K}_{\mathrm{TE}}(k_x, k_y) = \mathbf{t}_{\mathrm{J}}(k_x, k_y) \cdot \tilde{\mathbf{K}}(k_x, k_y), \tag{73}$$

$$\tilde{K}_{\mathrm{TM}}(k_x, k_y) = \mathbf{m}_{\mathrm{J}}(k_x, k_y) \cdot \tilde{\mathbf{K}}(k_x, k_y). \tag{74}$$

We will now derive the electric field amplitudes of the optical plane waves emitted by one of the current waves, using the electromagnetic boundary conditions. The geometry of the problem is shown for TE currents in Fig. 15a and for TM currents in Fig. 15b. For simplicity of notation we define the coordinate system such that the TE and TM currents are x- and y-directional, respectively. In this coordinate system, the electric field of a TE-polarized plane wave will only have an x-component, and the electric field of a TM-polarized wave will have y- and z-components. Also, the wave vector will always be in the yz-plane because $k_x = 0$. Furthermore, we assume that the refractive index is the same for waves emitted in both directions, so the material can be bifacial but not internally twisted. We first insert a TE-polarized plane wave $\mathbf{E} = \mathbf{x}E_x \exp[i(k_y y + k_z z)] \exp[-i\omega t]$ into Maxwell's equations [Eqs. (3) and (4) with constitutive relations of Eqs. (13)–(19)], which yield

$$k_z E_x = k\eta H_y, \tag{75}$$

$$-k_y E_x = k\eta H_z, \tag{76}$$

$$k_y H_z - k_z H_y = -\frac{k}{\eta} E_x. \tag{77}$$

We can write these equations for the waves propagating in the positive and negative z-directions; let us label these directions with the subindices 2 and 1, respectively.

The boundary conditions of Eqs. (23)–(26) simplify, with the help of Eq. (19), to the following form:

$$H_{2y} - H_{1y} = K_{\mathrm{TE}}, \tag{78}$$
$$n_2\eta_2 H_{2z} - n_1\eta_1 H_{1z} = 0, \tag{79}$$
$$E_{2x} - E_{1x} = 0. \tag{80}$$

Here, n_1 and η_1 are the refractive index and impedance for the plane wave emitted to the left (negative z-direction), and n_2 and η_2 are the same parameters for the wave emitted to the right (positive z-direction). The surface electric current density K_{TE} is simply $K_{\mathrm{TE}} = \tilde{K}_{\mathrm{TE}} \exp(ik_y y) \exp(-i\omega t)$. Substituting Eq. (75) into Eq. (78) for both left- and right-going plane waves and using Eq. (80) yields the electric-field amplitude

$$E_{\mathrm{TE}} = E_{1x} = \frac{k}{k_z} \frac{K_{\mathrm{TE}}}{\frac{1}{\eta_1} + \frac{1}{\eta_2}}. \tag{81}$$

This holds at all points on the interface, so dividing Eq. (81) by $\exp(ik_y y) \exp(-i\omega t)$ shows that the equation holds also for the wave amplitudes $\tilde{E}_{\mathrm{TE}}$ and $\tilde{J}_{\mathrm{TE}}$. Also, we note that the amplitude is the same for the plane waves propagating in the positive and negative z-directions.

Inserting a TM-polarized plane wave $\mathbf{E} = (\mathbf{y}E_y + \mathbf{z}E_z) \exp[i(k_y y + k_z z)]$ into Maxwell's equations, we obtain

$$k_y E_z - k_z E_y = k\eta H_x, \tag{82}$$
$$k_z H_x = -\frac{k}{\eta} E_y, \tag{83}$$
$$-k_y H_x = -\frac{k}{\eta} E_z. \tag{84}$$

Like in the case of TE polarization, the boundary conditions simplify to

$$H_{2x} - H_{2y} = K_{\mathrm{TM}} \tag{85}$$
$$E_{2y} - E_{1y} = 0 \tag{86}$$
$$\frac{n_2}{\eta_2} E_{2z} - \frac{n_1}{\eta_1} E_{1z} = \sigma, \tag{87}$$

where the surface density of free charge σ can be calculated from the charge conservation equation $\nabla \cdot \mathbf{J} = -d\rho/dt$, which gives

$$\sigma = \frac{K_{\mathrm{TM}} k_y}{\omega}. \tag{88}$$

Substituting Eq. (83) into Eq. (86) and the result into Eq. (85), we obtain the magnetic field of the left-going wave,

$$H_{1x} = \frac{K_{\mathrm{TM}}}{1 + \frac{\eta_1}{\eta_2}}, \tag{89}$$

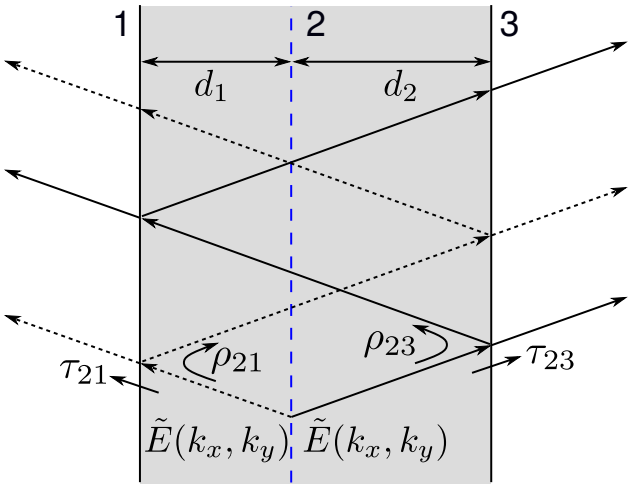

Figure 16: Propagation of plane waves radiated by an emitter in a metamaterial slab (medium 2), with arbitrary media 1 and 3 on the left and right sides of the slab, respectively. The electric currents of the emitter are known on a plane marked with the vertical blue dashed line. Each current wave in the emitter plane creates a plane wave with amplitude $\tilde{E}(k_x, k_y)$ to the right (solid lines) and to the left (dashed lines). The waves undergo multiple reflections inside the slab and contribute to the waves propagating into media 1 and 3.

and by using the definition of impedance in Eq. (18) we find the electric-field amplitude of the TM-polarized wave to be

$$E_{\mathrm{TM}} = \frac{K_{\mathrm{TM}}}{\frac{1}{\eta_1} + \frac{1}{\eta_2}}. \tag{90}$$

Again, we can divide Eq. (90) by $\exp(ik_y y)\exp(-i\omega t)$ to obtain the same relation for the wave amplitudes $\tilde{E}_{\mathrm{TM}}$ and $\tilde{K}_{\mathrm{TM}}$, which are equal for both plane waves. The amplitudes $\tilde{E}_{\mathrm{TE}}$ and $\tilde{E}_{\mathrm{TM}}$ as functions of k_x and k_y form the angular spectrum emitted by the dipole, which we can then freely propagate away from it. In particular, we can place the dipole inside a metamaterial slab and determine the radiation coming out. Figure 16 shows a slab with an embedded dipole emitter located somewhere on the plane (blue dashed line) that is at a distance of d_1 from the left and d_2 from the right surface of the slab, and where its angular spectrum is known. Each plane wave in the spectrum undergoes multiple reflections inside the slab. The amplitudes of the waves transmitted and reflected at each surface are given by the generalized Fresnel coefficients of Eqs. (39) and (40). It is straightforward to sum the infinite series of transmitted waves that interfere with each other to obtain the angular spectra on the left and right surfaces of the slab. These spectra are, respectively,

$$\tilde{E}^{\mathrm{L}} = \tau_{21} e^{ik_z d_1} \frac{1 + \rho_{23} e^{ik_z 2d_2}}{1 - \rho_{21}\rho_{23} e^{ik_z 2(d_1+d_2)}} \tilde{E}, \tag{91}$$

$$\tilde{E}^{\mathrm{R}} = \tau_{23} e^{ik_z d_2} \frac{1 + \rho_{21} e^{ik_z 2d_1}}{1 - \rho_{21}\rho_{23} e^{ik_z 2(d_1+d_2)}} \tilde{E}, \tag{92}$$

where $\tilde{E}$ is the plane-wave spectrum in the emitter plane, and the generalized Fresnel coefficients τ_{21}, τ_{23}, ρ_{21} and ρ_{23} are defined as shown in Fig. 16. The amplitude

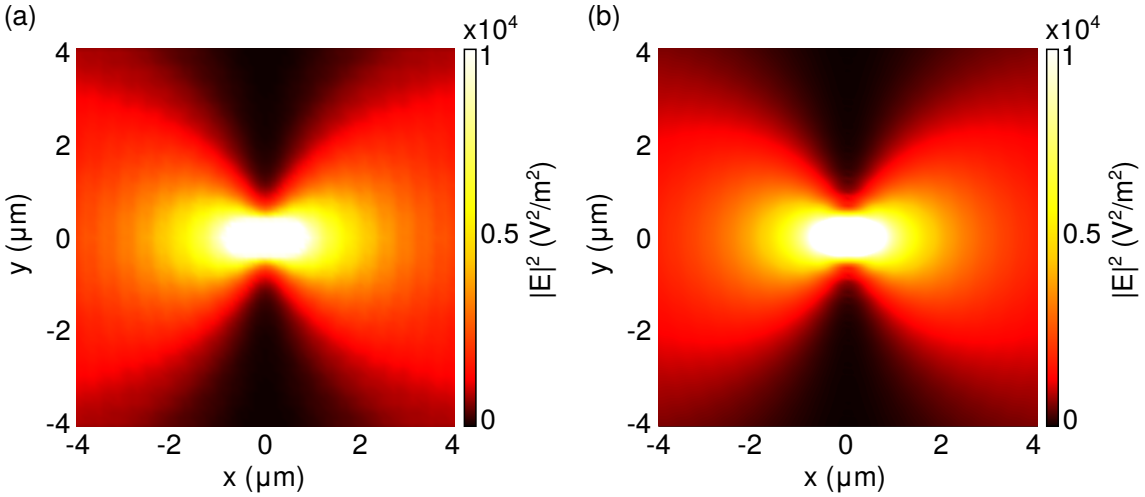

Figure 17: The intensity distribution of the field of a dipole emitter positioned at the center of a glass slab. The distribution is given in vacuum on the surface of the slab, as calculated by (a) the finite element method and (b) the current decomposition method.

spectra $\tilde{E}^{\mathrm{L}}$, $\tilde{E}^{\mathrm{R}}$ and $\tilde{E}$ as well as the Fresnel coefficients have the same (k_x, k_y)-dependency. This calculation is done for the TE and TM waves separately, using the corresponding Fresnel coefficients τ_{21}, τ_{23}, ρ_{21} and ρ_{23}, as well as the z-component of the wave vector k_z for each polarization. Equation (49) can then be used to calculate the actual electric-field distribution from the plane-wave spectrum.

Both evanescent and propagating waves can be included in the plane-wave spectrum of the electric-current decomposition of Eq. (69) and the resulting plane-wave spectrum. Furthermore, both the outgoing waves and the waves confined inside the slab are present in the angular spectra. This poses some difficulty in numerical calculations, where a discrete Fourier transform is used to implement Eqs. (69) and (70). This makes the number of plane waves finite and the angular spectra actually represent the emission of a periodic, infinite array of dipoles. In order to avoid interference effects between these dipoles, a large enough calculation domain must be used. In addition, one can further reduce the interference by introducing a slight absorption into the slab and perhaps the surrounding medium. In many metamaterials, this problem is not significant, since the waves trapped in the slab already experience high absorption.

Let us now demonstrate the method in a simple test case: a dipole emitter (with a current dipole moment of $1 \times 10^{-12}\,\mathrm{A\,m}$ [see Eq. (68)] chosen to make the numerical values of intensity convenient) located at the center of a slab of glass surrounded by air. To prevent periodic-dipole interference, we introduce a slight absorption, using refractive indices $n = 1.5 + 0.0015i$ for glass and $n = 1 + 0.001i$ for vacuum (the imaginary parts are chosen to be orders of magnitude smaller than the real parts). We pick a wavelength of $\lambda_0 = 1\,\mu\mathrm{m}$ and set the slab thickness to 333 nm, which is equal to $\lambda/2$ in glass. Thus, we are on a Fabry-Pérot resonance for normally incident waves. Figure 17a shows the intensity distribution on the surface of the slab computed by a direct numerical finite-element method calculation (using the

software Comsol Multiphysics), while Fig. 17b shows the same distribution calculated by the electric current decomposition method implemented in Matlab. The results are nearly identical, demonstrating that our semianalytical method is sufficiently accurate. A weak standing-wave pattern seen in Fig. 17a is a numerical artifact caused by not perfectly suppressed reflection from the perfectly-matched layer used at the boundaries of the computational domain. Comparing the calculation times, if a typical FEM calculation with sufficient accuracy takes several minutes, the computation time of the decomposition method is measured in seconds.

The electric-current decomposition method, when used together with the interferometric approach introduced in Section 2.3, inherits the limitations of the latter, i.e., the metamaterial around the dipole must have a layered structure with no evanescent-wave coupling between the layers, and have the TE- and TM-polarized modes. The current wave decomposition does not admit dipoles oriented normal to the plane of the current, though it is possible to generalize the method to such dipoles. It is also possible to combine the electric-current decomposition with the transfer-matrix method, which would allow treatment of metamaterials that do not have polarization modes. Finally, even in metamaterials with no interlayer evanescent-wave coupling, the evanescent fields due to the internal structure can be significant between the layers, and will promote near-field interaction between the dipole emitters and the metamolecules. This will influence the Purcell effect and radiation patterns, making them depend on the exact location of the emitter. Any effective-medium approach where the material is considered continuous will not grasp this effect exactly. In such cases, the electric current decomposition method will not be exact, but will still yield good agreement with direct numerical calculations in many materials, as will be demonstrated in Section 5. If the dipole-metamolecule near-field coupling is too significant, one can first use direct numerical calculations to determine the plane-wave spectra of the emitter coupled to *one* layer of metamolecules, and then propagate the resulting fields using the methods of Section 2.4. This will, however, sacrifice the simplicity of the electric current decomposition method.

4.3 Far-field emission

The electric current decomposition method is not only capable of determining the fields produced by point dipoles embedded in metamaterial slab, but can also approximately treat infinite spatially dispersive media and provide understanding of how optical energy propagates in them. Equations (81) and (90) reveal the angular spectrum emitted by a dipole. Determining the radiation in the far field is then a matter of propagating the angular spectrum to a point of interest that is convenient to represent in spherical coordinates $(x,y,z) = (r\sin\theta\cos\varphi,\ r\sin\theta\sin\varphi,\ r\cos\theta)$, where r is the radius of the sphere and θ and φ are the polar and azimuthal angles. Explicitly, the propagation equation, Eq. (49), can be written as

$$\hat{\mathbf{E}}(x,y,z) = \frac{1}{(2\pi)^2}\int_{-\infty}^{\infty}\int_{-\infty}^{\infty}\tilde{\mathbf{E}}(k_x,k_y)e^{i[k_x x+k_y y+k_z(k_x,k_y)z]}dk_x dk_y. \tag{93}$$

When x, y and z are large enough, the integral may be solved approximately using the method of stationary phase. This method was utilized in [29] to determine far fields in isotropic media, but here we let the medium be anisotropic and spatially dispersive. The method of stationary phase observes that the oscillations of the complex exponential become very fast at large arguments (here, at large x, y and z) and tend to interfere destructively. In this situation, the major contribution to the integral comes from the parts of the angular spectrum for which the phase of the complex exponential $\phi = k_x x + k_y y + k_z(k_x, k_y)z$ has a critical point. At such a point of stationary phase, we have

$$\frac{\partial \phi}{\partial k_x} = 0, \tag{94}$$

$$\frac{\partial \phi}{\partial k_y} = 0, \tag{95}$$

from which we derive the conditions

$$\frac{\partial k_z}{\partial k_x} = -\frac{x}{z} \tag{96}$$

$$\frac{\partial k_z}{\partial k_y} = -\frac{y}{z}. \tag{97}$$

These equations show that the main contribution to the far-field point $\mathbf{r} = (x,y,z)$ comes from the parts of the $\mathbf{k}$-surface that are normal to $\mathbf{r}$. This is shown in Fig. 18 in two dimensions. Around such a point, $\mathbf{k}_s$, on the $\mathbf{k}$-surface, we can expand the phase in a Taylor series. Writing $\Delta\mathbf{k} = \mathbf{k} - \mathbf{k}_s$ as a column vector, we obtain

$$\phi = k_{sx}x + k_{sy}y + k_{sz}z + \frac{z}{2}\Delta\mathbf{k}^T H(k_z)\Delta\mathbf{k} + \cdots, \tag{98}$$

where $H(k_z)$ is the Hessian matrix with elements

$$H(k_z)_{ij} = \frac{\partial^2 k_z}{\partial k_i \partial k_j}, \tag{99}$$

where i and j are either x or y and the derivatives are evaluated at $\mathbf{k} = \mathbf{k}_s$. Discarding the terms of orders higher than 2 from the series, we can solve the integral of Eq. (93) analytically. Specifically, we can diagonalize the real, symmetric part of the Hessian matrix as $H = VDV^T$ (assuming that the imaginary part is negligibly small), to find its eigenvalues D_1 and D_2 and the eigenvectors. Transforming the variables k_x and k_y to the eigenbasis (new variables b_1 and b_2), we simplify the integral and obtain the following expression for the far-field amplitude

$$\hat{\mathbf{E}}(x,y,z) = \frac{1}{(2\pi)^2} e^{i(k_{sx}x + k_{sy}y + k_{sz}z)} \tilde{\mathbf{E}}(k_{sx}, k_{sy}) \int_{-\infty}^{\infty}\int_{-\infty}^{\infty} e^{i\frac{1}{2}z(D_1 b_1^2 + D_2 b_2^2)} db_1 db_2 \tag{100}$$

$$= \frac{1}{2\pi} e^{i(k_{sx}x + k_{sy}y + k_{sz}z)} \tilde{\mathbf{E}}(k_{sx}, k_{sy}) \frac{i}{z} \frac{1}{\sqrt{D_1 D_2}}. \tag{101}$$

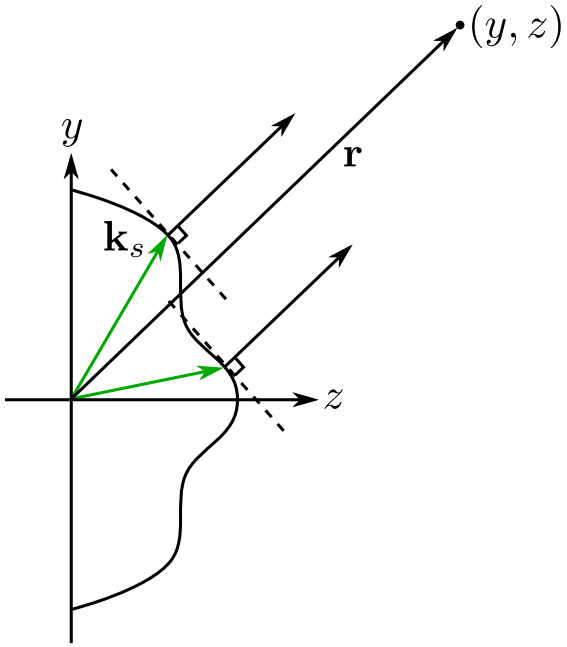

Figure 18: A two-dimensional version of the **k**-surface of a metamaterial. The point $\mathbf{k}_s$ is a point of stationary phase for the far-field point (y,z), as the tangent to the surface (dashed line) at $\mathbf{k}_s$ is perpendicular to the position vector $\mathbf{r}$. Another point on the **k**-surface (the second green arrow) also contributes to the far-field at $\mathbf{r}$.

Denoting $A = \partial^2 k_z/\partial k_x^2$, $B = \partial^2 k_z/\partial k_y^2$ and $C = \partial^2 k_z/\partial k_x \partial k_y$, where all the derivatives are evaluated at $\mathbf{k}_s$, the eigenvalues can be written as

$$D_{1,2} = \frac{1}{2}\left[A + B \pm \sqrt{(A+B)^2 - 4(AB - C^2)}\right]. \tag{102}$$

Here we choose the sign + for D_1 and − for D_2. For isotropic media, we find $D_1 = -1/k_z$ and $D_2 = -k^2/k_z^3$, and Eq. (101) becomes

$$\hat{\mathbf{E}}(x,y,z) = \frac{i}{2\pi} e^{i(k_{sx}x + k_{sy}y + k_{sz}z)} \tilde{\mathbf{E}}(k_{sx}, k_{sy}) \frac{k_z}{r}, \tag{103}$$

which agrees with [29]. For metamaterials, we can calculate the derivatives A, B and C from a numerically-determined **k**-surface that is readily obtained from the refractive-index distribution. To determine the power flux, one can use the plane-wave Poynting vector of Eq. (22). In general, there may be multiple points of stationary phase contributing to the same far-field point. In this case, their contributions should be summed.

In a two-dimensional situation, where the fields do not vary in the x-direction, the electric far-field amplitude has a slightly different form. Using the same stationary-phase method, one can derive the following expression for it:

$$\hat{\mathbf{E}}(y,z) = \frac{1+i}{2\sqrt{\pi}} \tilde{\mathbf{E}}(k_{sy}) e^{i(k_{sy}y + k_{sz}z)} \frac{1}{\sqrt{z}} \left(\frac{\partial^2 k_z}{\partial k_y^2}\right)^{-1/2}. \tag{104}$$

Equations (101) and (104) disregard optical absorption in the material, and strictly speaking, overestimate the intensity in the far field. As the absorption can depend on the propagation angle due to spatial dispersion, it will further modify the far-field intensity distribution. In principle, the effect can be estimated by determining the imaginary part of k_z and multiplying the intensity distribution by the factor of $\exp(-2k_z z)$.

Finally, we determine the power emitted by dipoles in an isotropic medium, which can be used when computing the Purcell factor or the emission enhancement factor due to the emitter interacting with nanostructures. This is done by integrating the Poynting vector over a small sphere centered on the dipole, or in the two-dimensional case, over a circle. In the three-dimensional case, the dipole's power is

$$P = \frac{J_0^2}{4\pi}\frac{\eta k^2}{3}, \tag{105}$$

which again agrees with [29] but is here written in terms of different quantities. In two dimensions, the power (per unit length) for dipoles perpendicular to the 2D plane (TE-polarized) is

$$P = \frac{1}{8}J_0^2\eta k, \tag{106}$$

and for in-plane dipoles (TM-polarized),

$$P = \frac{1}{16}J_0^2\eta k. \tag{107}$$

In nonmagnetic media, the impedance can be written as $\eta = \eta_0/n$ where η_0 is the impedance of vacuum, while the wavenumber is $k = k_0 n$. From this we see that in three dimensions, the dipole power is proportional to the refractive index n, and in two dimensions the proportionality disappears.

5 Generation of light in metamaterials

In this section we study quantum emitters embedded in metamaterials and other nanostructures, employing both direct numerical simulations and the electric current decomposition method of Section 4.2. All direct calculations are performed using the finite-element method based software Comsol Multiphysics. In Section 5.1 we show how a metallic cavity at its cutoff frequency can act as a two-dimensional zero-index metamaterial, and demonstrate how such a structure can enhance the emission rate of multiple emitters embedded in it as well as shape their wavefronts. In Section 5.2 we show that dipole emitters in diffraction-compensating metamaterials will radiate collimated beams. In Section 5.3 we use a nanoantenna, a metasurface and a bifacial metamaterial to create emitters that radiate in a single direction.

5.1 Generation of light in a zero-index metamaterial

Metamaterials with a zero refractive index (known also as epsilon-near-zero metamaterials) are among the most "unnatural" of all metamaterials. The phase velocity of light in such a material is nearly infinite, which ideally has the effect that an electromagnetic field will have the same phase at each point inside the material. This has been used to demonstrate various interesting phenomena, such as shaping of an emitter's wavefronts [78], non-local enhancement of optical gain [79] and "supercoupling" that is tunneling of electromagnetic energy through narrow channels [80]. For optical wavelengths, zero-index metamaterial designs based on silicon rods [68] and metal-dielectric layer stacks [81] have been demonstrated. However, the simplest possible two-dimensional zero-index "metamaterial" is a planar metallic cavity or single-mode metal waveguide at its cutoff frequency [78]. Conceptually, the waveguide mode in this structure consists of two counterpropagating plane waves with wave vectors perpendicular to the metallic plates that are separated by a distance of half the wavelength. The mode then has a single maximum exactly between the plates and, ideally, zero amplitude on the plate surfaces. In any plane between the plates, the components of the $\mathbf{k}$-vector are zero, so in principle, the effective refractive index for the mode is also zero. In reality, the reflectivity of the metal plates is not perfect, and due to losses, the effective refractive index will have an imaginary part. Also, the waveguide will have evanescent modes originating from its finite size. In this section we consider quantum emitters located in such near-zero-index waveguides. We demonstrate the phase of the electromagnetic field radiated by a dipole to be constant in the effectively two-dimensional zero-index medium and show that when many emitters are placed into it, the emitters will preferably oscillate in phase with each other. We also observe that the wavefronts of an emitter placed inside a zero-index waveguide will, in the surrounding medium, take the shape of the waveguide, which can be used to create spatially coherent, highly-collimated light sources with designable wavefronts.

Consider the structure shown in Fig. 19. It consists of two finite silver plates (side lengths are $w_y = w_z = 4\,\mu\text{m}$ and the thickness is $w_\text{m} = 100$ nm), and a layer of glass between them (the thickness is $w_x = 175$ nm). The structure is also surrounded

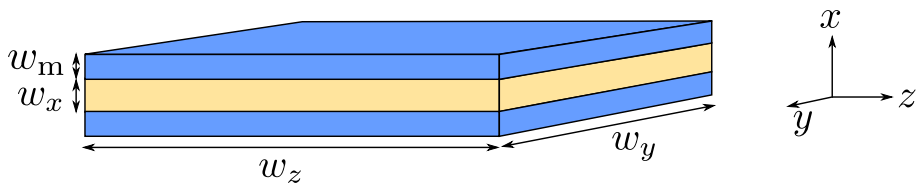

Figure 19: A waveguide consisting of silver plates (blue) on both sides of a glass slab (yellow). The structure is surrounded by glass (not shown).

by glass. The cutoff condition is achieved at $\lambda_0 = 660$ nm. While we would initially expect to require $w_x = 220$ nm to fulfill the $\lambda/2$ condition, the field penetrates slightly into the silver plates, which increases the effective thickness of the central part of the waveguide. We will now verify the zero-index properties of this structure for time-harmonic fields with $\lambda_0 = 660$ nm. All following calculations will be performed using the finite-element method of the Comsol Multiphysics software.

Let us place a z-polarized dipole emitter at the center of the waveguide. We model the emitter as a point dipole with a fixed current dipole moment of 1×10^{-12} A m [see Eq. (68)], corresponding to an electric dipole moment of 3.5×10^{-28} C m that is on the order of transition dipole moments of some typical fluorescent molecules [87]. Figure 20a shows the amplitude distribution of the field at $x = 0$, exactly between the metal plates. The field is strong inside the waveguide and is coupled out mostly from the left and right sides of the structure. In Fig. 20b, the blue line shows the field amplitude on a y-directional line passing through the dipole. We observe that the field is not constant but instead exponentially decaying with a $1/e$ decay length of

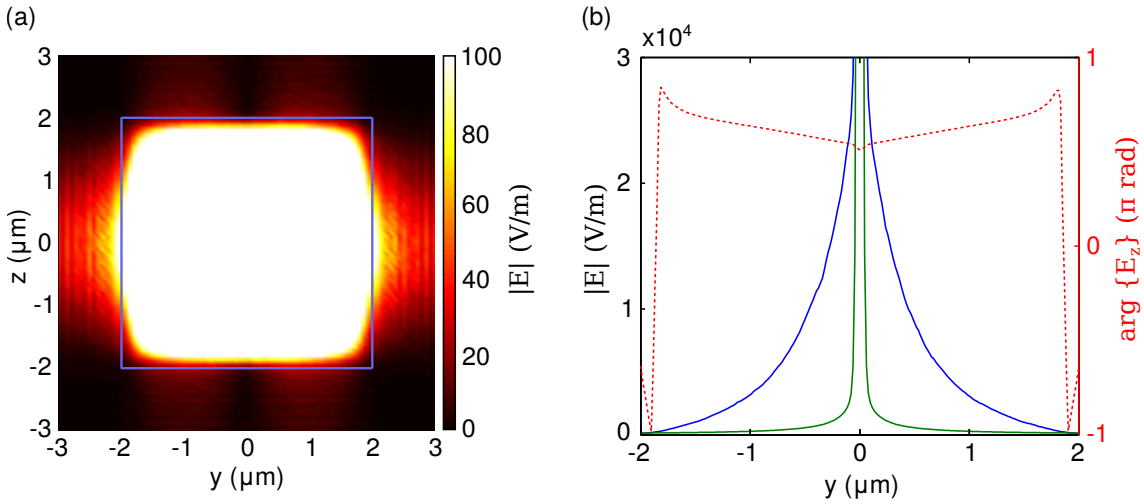

Figure 20: Field of a z-polarized dipole emitter located at the center of a zero-index waveguide. The electric field amplitude between the plates of the waveguide ($x = 0$) is shown in (a), where all values larger than 100 are displayed in white in order to show the field transmitted out of the waveguide. The waveguide edges are shown with blue lines. In (b), the blue line shows the electric field amplitude on a y-directional line passing through the dipole, and the red dashed line shows the phase of the z-component of the field. The green line shows the electric field amplitude of a dipole in glass.

400 nm. This is caused by optical absorption in the metal. For comparison, the green line shows the electric field amplitude of a dipole in glass. Clearly, the waveguide spreads the dipole field to a larger area. Figure 20b also shows the phase of the z-component of the electric field (red dashed line), which changes very slowly inside the structure as we would expect in a near-zero-index medium. By measuring the phase change from the slowly-varying part, we find that the real part of the effective refractive index inside the structure is $n_{\text{eff}} = 0.03 + 0.26i$. The Purcell factor is $\mathcal{P}_{\text{h}} = 1.0$, but only 0.5 % of the power is radiated out of the cavity as it is much larger than the absorption length.

Having measured the effective refractive index and verified the zero-index property of the structure, we reduce its size to increase the efficiency of the output coupling and study the radiation of multiple emitters. The new dimensions are $w_y = w_z = 2\,\mu\text{m}$. We start by considering two dipole emitters, both polarized in the z-direction, separated by a distance d along the z-axis. Their dipole moments have a certain phase difference. In free space, the radiated power and the field distribution will depend on the distance between the emitters and their phase difference. If $d > \lambda_0/2$, the radiation pattern will show diffraction orders. If we move the emitters closer to each other, they cannot be spatially resolved from the far field. In the most extreme case the dipoles are almost at the same coordinate. If they are in phase, they form an effective dipole with twice the moment of a single dipole (as long as strong-coupling interactions can be neglected [29]). If the dipoles are out of phase, they completely cancel each other. While in free space this happens only at distances much smaller than $\lambda_0/2$, in a near-zero-index medium the effective wavelength is long which increases the range of the effect. In our waveguide with $Re\{n_{\text{eff}}\} = 0.03$, the effective wavelength at $\lambda_0 = 660$ nm is 22 µm. Therefore, we expect that if two emitters are placed in the waveguide, they will create a strong output field if in phase and a weak field if out of phase.

Figure 21a shows the amplitude distribution of the field for two z-polarized emitters that oscillate in phase. Both have a current dipole moment of $1 \times 10^{-12}\,\text{A m}$, and the emitter-to-emitter distance is $d = 500$ nm. The field is strong and uniform. The output power is 23 nW and the total power including the absorbed part is 63 nW. The power radiated by two overlapping in-phase dipoles in infinite glass is 5.4 nW. Using this result, we find a Purcell factor of $\mathcal{P}_{\text{h}} = 12$ and an emission enhancement factor of $\mathcal{E} = 4$. In contrast, Fig. 21b shows field amplitude distribution for two out-of-phase emitters. The field is split into two parts and the output power is massively reduced to 1.8 nW. This shows that the dipoles, when simultaneously excited, will emit considerably faster when in phase than when out of phase. Ideally, the rate of emission from the waveguide will depend on the number of emitters squared, instead of just the number of emitters like in ordinary fluorescence [68]. However, when considering real emitters, there may be other interaction effects such as strong coupling and nonradiative transitions, which must be considered before making this conclusion. Also, in spontaneous emission the dipole moments will have random phases when the emitters are independent. The in-phase situation is therefore not always reached. Recently, it has been proposed that nonlinear interactions can lead to the synchronization of the emitters and therefore the radiative enhancement

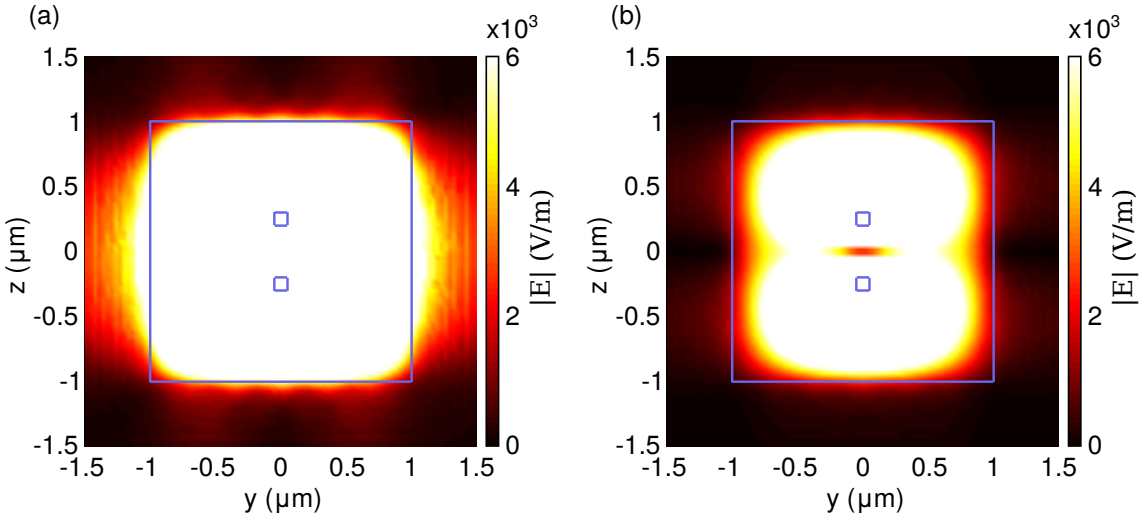

Figure 21: Electric field amplitude of two z-polarized dipole emitters (locations shown by small blue rectangles) in a zero index waveguide (edges shown by blue lines). The field is shown at $x = 0$. In (a) the emitters are in phase with each other, while in (b) they have a phase difference of $\Delta\varphi = \pi$.

predicted above [82].

Finally, let us consider the formation of wavefronts at the edge of a near-zero-index waveguide. Since it indeed acts as a near-zero-index structure, the phase of the electric field created by a dipole emitter should be the same at each point along the edge. The wavefront emitted from the structure will then take the shape of the edge. To demonstrate this, let us cut a circle section out of the waveguide of Fig. 21. Figure 22a shows the shape of the modified waveguide, along with the field amplitude at $x = 0$ created by a single y-polarized dipole. Clearly, the beam propagating in

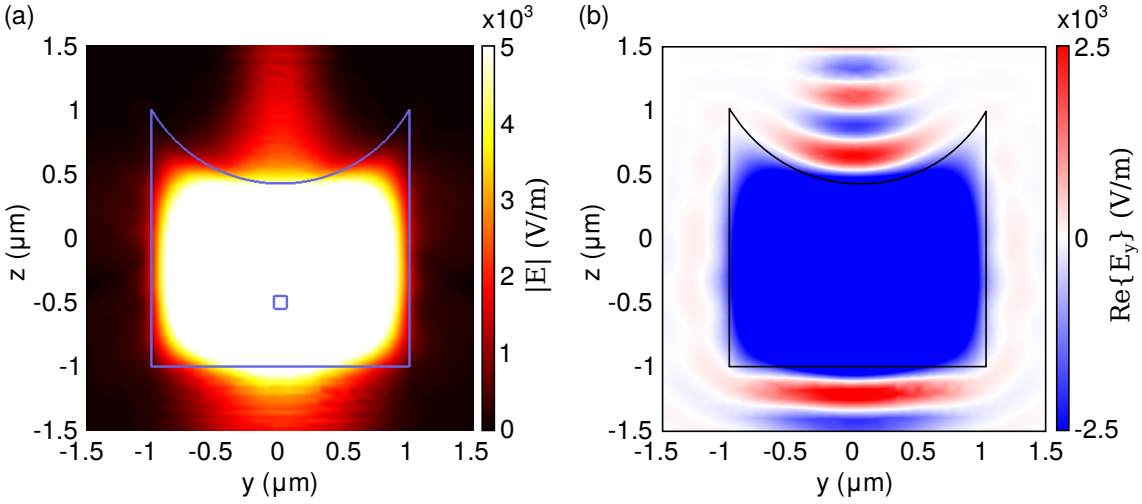

Figure 22: Electric field amplitude of a y-polarized dipole emitter (location shown by blue rectangle) in a zero index waveguide with a circle section cut off (edges shown by blue lines).

the positive z-direction from the structure is focused towards the center of the circle. Figure 22b shows the y-component of the electric field at a fixed time, where one can observe that the outgoing wavefronts conform to the waveguide shape, as expected.

Our results highlight some of the most interesting properties of zero-index materials. In particular, we have demonstrated the tendency of multiple spontaneous emitters in the material to radiate in phase and form single-mode output fields similarly to single-mode lasers. In addition, the emission of the dipoles can be significantly enhanced. Hence, the spontaneously-emitted output beams can have a high brightness and flat wavefronts without the need to create a population inversion and exceed the laser threshold. The emitters in a near-zero-index waveguide may be pumped, e.g., electrically or optically using a small slit on one of the metal plates.

5.2 Point emitters in a diffraction-compensating metamaterial

As summarized in Section 3.1, the elimination of diffraction has been studied in many media, in regard to the propagation of optical beams and images, but it is interesting to study this phenomenon also from the point of view of light emission. Usually, spontaneous radiation of point-like quantum emitters is isotropic. One way to achieve unidirectional energy transfer is to couple an emitter into a waveguide so that it radiates into the waveguide modes [83, 84]. On the other hand, one can force the emitter to radiate into a collimated beam by placing it in a diffraction-compensating material. The effect has been demonstrated in self-collimating photonic crystals with surface modifications that increase the output-coupling efficiency of light [85, 86]. In metamaterials, self-collimation of emission based on the diffraction-compensation phenomenon has not yet been demonstrated. In this section, we show that this can be done without need of any surface modifications.

In Section 3.1 we considered a diffraction-compensating metamaterial made of short silver rods. Here, we further optimize the geometry of the material to obtain a high directivity of the emission and minimize energy leakage to modes trapped inside the metamaterial slab. The new structure is basically the same as in Fig. 3a, but the dimensions of the silver rods are 40 nm in the transverse and 130 nm in the longitudinal direction, and the lattice constants are $\Lambda_x = \Lambda_y = 120$ nm and $\Lambda_z = 200$ nm. Figures 23a and 23b show the refractive index and normalized impedance, respectively, calculated for the new material as functions of propagation angle θ at the diffraction-compensation wavelength $\lambda_0 = 793$ nm for TM-polarized waves. This material has been introduced in one of our publications (see Ref. [19]). As before, the refractive index has a wide flat region in its real part and a negligible imaginary part at small propagation angles. At large angles, $\mathrm{Re}\{n_{\mathrm{eff}}\}$ seems to curve back towards smaller values unlike the contour in Fig. 3b. The impedance is again nearly matched to glass impedance at small θ. Figure 23c shows the two-dimensional directivity parameter D of emission, calculated using the method explained in Section 4.3 for a TM-polarized point dipole. A very high directivity is obtained near $\theta = 0$, meaning that the radiated dipole field cannot spread. The maxima of the directivity parameter are actually found at $\pm$ 1.5° due to a slight curvature of the isofrequency contour

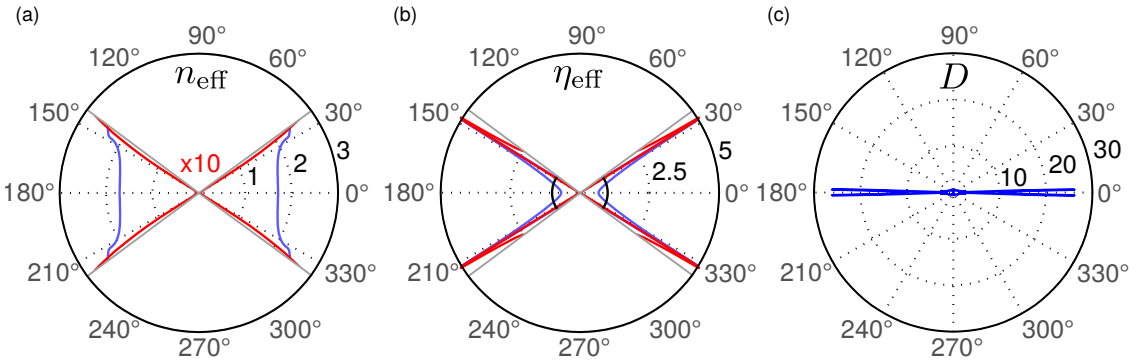

Figure 23: Characteristics of a diffraction-compensating metamaterial designed for TM-polarized waves at $\lambda_0 = 793$ nm. For the refractive index (a) and normalized impedance (b), the blue/red lines show their real/imaginary parts as functions of the wave propagation angle θ. For n_{eff} the imaginary part is multiplied by 10 to make it more visible. In (b), the black lines show the impedance of glass. The white sectors correspond to propagation directions not available for waves incident from glass. The two-dimensional directivity parameter D of a dipole (c) emitting into the material peaks near $\theta = \pm 1.5°$ and drops down to $D = 10$ at $\theta = 0$.

of $\text{Re}\{n_{\text{eff}}\}$. We thus expect that most of the energy emitted by the dipole will be contained in a well-collimated beam propagating in the material.

Let us consider a slab of the designed material, with 8 metamolecular layers, surrounded by glass. In order to obtain a reasonably accurate direct numerical solution, we simplify the problem by making it effectively two-dimensional. We assume that instead of a single dipole source, we have an infinite chain of them distributed periodically in the x-direction, with the period being equal to the unit-cell size Λ_x. This allows the calculation domain to include only one layer of the unit cells. In the y-direction, the slab must be wide enough to avoid possible edge effects. We choose the width of the slab to be equal to $60\Lambda_y$. We place a dipole emitter inside the slab between the first and second metamolecular layers and model it as a point electric current element with a current dipole moment of 1×10^{-12} A m [see Eq. (68)], corresponding to an electric dipole moment of 4×10^{-28} C m which is on the order of transition dipole moments of some typical fluorescent molecules [87], directed along the y-axis. The dipole is positioned on the yz-plane that intersects the rods at their geometric centers. Because of the introduced periodicity, the dipole source is actually a chain of coherent dipoles that generates purely TM-polarized waves.

Figure 24a shows the intensity of the emitted field in and around the slab, calculated directly by the finite-element method (FEM). The position of the dipole is marked by a black dot. We clearly see that the energy is concentrated in a beam directed along the z-axis ($\theta = 0$) as expected. The field penetrates into the silver rods in the near field of the source, but elsewhere it is almost completely concentrated in glass, resulting in a remarkably low absorption loss implied by the previously-calculated wave parameters. As the beam does not seem to have a standing wave pattern, the slab surfaces are highly transmitting, demonstrating the impedance

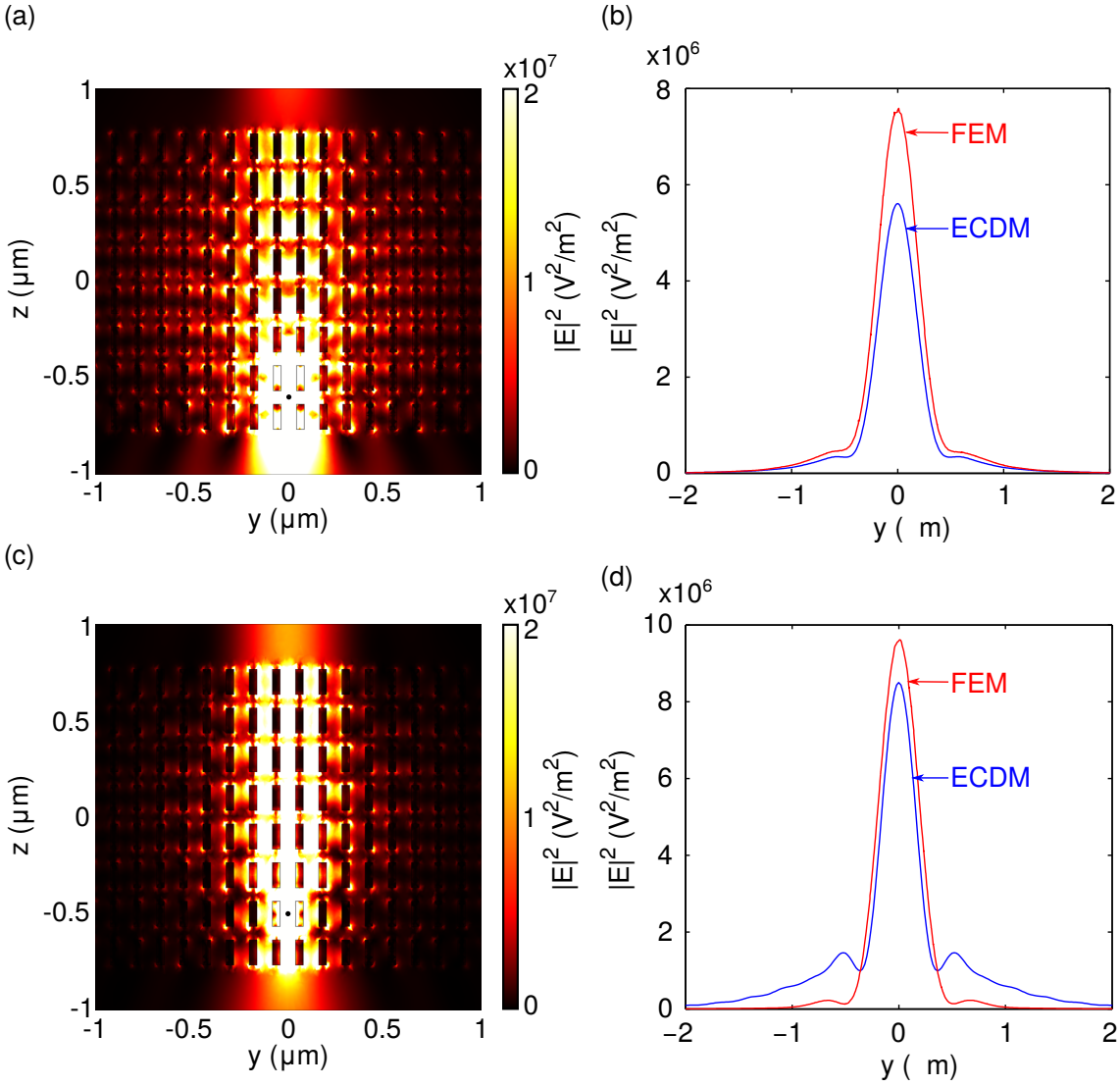

Figure 24: Intensity distributions of a dipole emitter embedded in a 8-layer slab of a diffraction-compensating metamaterial composed of nanorods. In (a) and (c), the dipole location is shown by a black dot. The intensity distribution at $z = 950$ nm is shown in (b), where the finite-element result (red curve) is compared to the result of the electric-current decomposition method (ECDM, blue curve). In (c), the dipole is moved to the middle of the second layer. The resulting intensity profiles, similar to those in (c), are shown in (d).

matching of the metamaterial to glass.

The output intensity profile at $z = 950$ nm calculated from Fig. 24a is shown in Fig. 24b by the red curve. For comparison, we use the electric-current decomposition method (ECDM) and the material's wave parameters to calculate the same intensity profile, shown by the blue curve. There is a 30 % difference in the intensities, but the shapes of the curves are almost identical. From the more accurate FEM result we can calculate the total emitted power per dipole that is 3.1 nW and then the Purcell factor [Eq. (64)] to be $\mathcal{P}_{\rm h} = 2.0$. Absorption by the rods accounts for only 10 % of the power, so we find an overall emission enhancement factor of $\mathcal{E} = 1.8$ (which

includes the beams emitted in both z-directions). The emitter will therefore have a high quantum yield of 90 %. The diameter of the output beam propagating in the positive z-direction is approximately 400 nm, and by calculating the angular spectrum of the beam we find that the divergence angle will be approximately 40° in glass.

In general, when quantum emitters radiate spontaneously, the orientation of their dipole moment is random. Thus, to determine the emission enhancement that will be observed in practice, we can average the results of three orthogonally-polarized dipoles. For the z-directional dipole we find $\mathcal{P}_\mathrm{h} = 0.4$ and for the x-polarized dipole $\mathcal{P}_\mathrm{h} = 0.7$, which are both much smaller than the $\mathcal{P}_\mathrm{h} = 2.0$ for the y-directional "wanted" dipole. This means that high quantum yield predicted above will indeed be observed in practice.

We have found that the exact location of the dipole affects its radiation pattern. As an example, we move the dipole to the position indicated by the black dot in Fig. 24c, i.e., between two rods in the second metamolecular layer. Figure 24c shows the resulting intensity distribution. The field confinement is improved compared to the results of the previous case. The output intensity profile at a distance of 150 nm from the top interface is shown in Fig. 24d, where the results of the FEM and ECDM calculations are shown by red and blue lines, respectively. The agreement between the results of the two methods is still good. The beam power calculated from the FEM result is approximately 20 % higher than in the previous case.

The results of direct numerical calculation by FEM and the semianalytical ECDM are fairly close. The most important reason for the differences between the results is undoubtedly the near-field interaction between the dipole and the nearby metamolecules, which cannot be seen by the effective-medium-based ECDM. The interaction appears to be more prominent when the dipole is directly between two of the rods. In terms of the calculation time, FEM solutions of sufficient accuracy took approximately 20 minutes each, while ECDM running time was a few seconds. This comparison, of course, does not take into account the time used to determine the wave parameters of the material.

The simplified "two-dimensional" situation studied here may in fact be realized if the metamolecules are embedded in a single-mode slab waveguide, an idea often implemented for two-dimensional photonic crystal slabs [38]. The wave parameters will be different in this case, requiring a re-optimization of the material. Contrary to dipole emitters coupled to a waveguide, the metamaterial is quite insensitive to a specific location of the dipole and can be used with a large number of emitters, e.g., to construct various spontaneous-emission or laser sources.

5.3 Point emitters in bifacial metasurfaces and metamaterials

In this section we study the interaction of quantum emitters with the gold-disc dimers of Section 3.2. These dimers prove useful not only as the units of a large crystalline metamaterial, but also as individual nanoantennas able to force a dipole emitter to create a single, unidirectional beam in free space.

5.3.1 Unidirectional nanoantennas and metasurfaces

Antennas are ubiquitous in wireless communication devices, as they are efficient emitters and receivers of electromagnetic radiation that can be designed to emit only in a certain direction. Building antennas at the micro- or nanoscale, required by optical frequencies, presents additional challenges compared to radio-frequency and microwave antennas due to the orders of magnitude shorter wavelengths. Various designs based on plasmonic structures have been demonstrated, including Yagi-Uda nanoantennas [63, 64], nanocubes [65] and bowtie antennas [88, 89], all providing various degrees of emission enhancement and directivity for otherwise isotropic quantum emitters. Positioning the emitter in the near field of the antenna allows it to transfer energy primarily into the antenna's resonant excitations which then emit into the far field. In this subsection we show that the gold-dimer metamolecules of the bifacial metamaterial of Section 3.2 can act as simple nanoantennas producing unidirectional radiation both individually and as a part of a metasurface.

Consider a dipole emitter located exactly between the discs of a single dimer metamolecule of Fig. 7a (see Fig. 25a). The emitter interacts with the discs, exciting dipolar electric currents in them. Hence, the radiated optical field will consist of a superposition of the fields of three dipoles. To obtain unidirectional emission, the fields must cancel each other in one direction and interfere constructively in the opposite direction. This happens at a vacuum wavelength $\lambda_0 = 690$ nm between the resonance wavelengths of the discs (see Fig. 7b).

Figure 25a shows the amplitude of the field radiated by the dipole at $\lambda_0 = 690$ nm. The field is calculated by the finite-element method using a current dipole moment of 1×10^{-12} A m. The near field is strong around the smaller disc, as its plasmonic resonance is closer to λ_0. However, looking beyond the near field, we see that almost nothing is emitted in the negative z-direction. This is confirmed by Fig. 25b, which shows the directivity of the radiation in the xz-plane (blue curve) and yz-plane (red curve). A maximum of 3.6 is reached in the positive z-direction ($\theta = 0$ in the figure). The radiative enhancement factor is $\mathcal{E} = 0.47$, and the Purcell factor is $\mathcal{P}_\mathrm{h} = 2.0$.

To determine the directivity of an emitter that radiates spontaneously, we average the emission patterns of three orthogonally-polarized dipole emitters. This results in the directivity shown in Fig. 25c. Obviously the z-polarized dipole radiates to the sides which makes the emission pattern more isotropic, but the backward emission is still negligible. The maximum directivity drops to 1.4 and the emission enhancement factor becomes $\mathcal{E} = 0.86$. Obviously the z-directional dipole has a large contribution to the overall radiation pattern. The wavelength of unidirectional emission is easy to tune by changing, since we only need to shift the resonance wavelengths of the discs. For example, increasing the radii of the discs will shift the resonances to longer wavelengths [90].

A planar array of the dimers form a metasurface. We choose the same lattice constants for the array as in Section 3.2, that is, $\Lambda_x = \Lambda_y = 180$ nm. To reduce the computation time, we model the metasurface as a 3x3 array of dimers. The best directionality of emission from the center of the array is achieved at a different wavelength of $\lambda_0 = 681$ nm. This change is caused by the near- and far-field

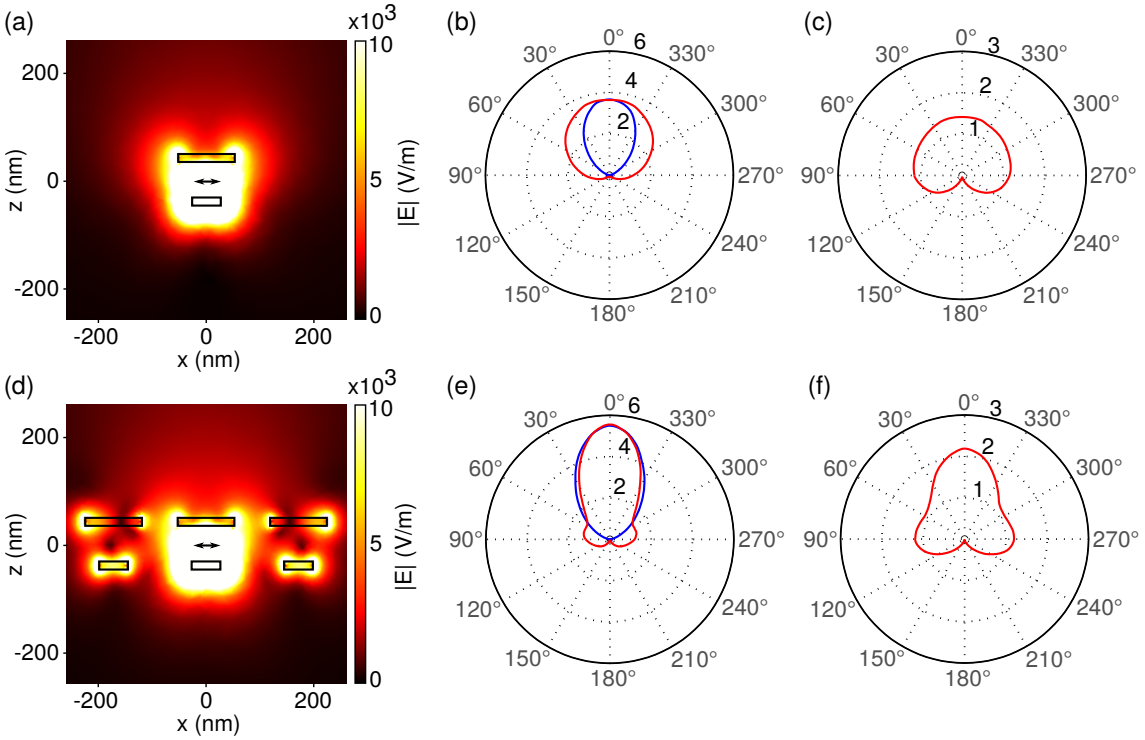

Figure 25: An x-polarized dipole emitter inside a gold-dimer metamolecule [(a)–(c)] and in a 3x3 array of such metamolecules [(d)–(f)]. The electric-field amplitude is shown in (a) and (d), while (b) and (e) show the directivity in the xz and yz planes (blue and red curves, respectively). Distribution of the average directivity of a randomly-polarized dipole is illustrated in (c) and (f).

interaction between the dimers. Figure 25d shows amplitude distribution of the field for an x-polarized dipole. The dipole is now coupled to the neighbouring dimers as well, which increases the far-field intensity by 10 % in the main radiation cone. Figure 25e shows that the directivity increased to 5.5 due to the collective action of the dimers. The radiative enhancement factor is now $\mathcal{E} = 0.54$, while the Purcell factor is $\mathcal{P}_\mathrm{h} = 3.0$. Figure 25f presents the average directivity of a spontaneously emitting dipole with a maximum of 2.2 that is higher than for the single-dimer case in Fig. 25c. Overall, the metasurface improves the single-antenna result significantly. In both structures, the directivity is improved at the cost of decreased quantum yield. However, the far-field intensity in the positive z-direction increases compared to an emitter in free space by a factor of 2 for a dipole in the metasurface.

5.3.2 Bifacial metamaterials

In this subsection, we study the radiation characteristics of a dipole emitter embedded in a bifacial metamaterial slab. Our motivation is the possibility to create a unidirectionally-emitting metamaterial slab without need for exact microscopic positioning of the emitters. In Section 4.2, we derived Eqs. (91) and (92), describing the plane-wave spectra of a dipole emitter embedded in such a slab. As a simple

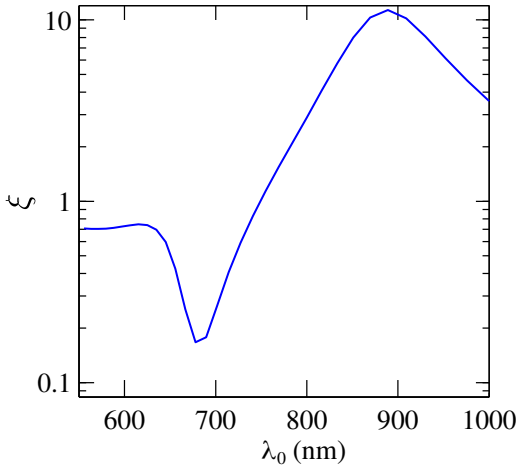

Figure 26: The ratio ξ of the radiated plane-wave intensities calculated from Eq. (108) for a two-layer slab of the gold-dimer metamaterial of Fig. 7.

figure of merit for unidirectional emission, we can take the ratio of intensities of two counterpropagating plane waves emitted by the slab in the opposite directions along the slab normal. When the emitting dipole is at the center of a slab of thickness D, this ratio is

$$\xi = \left|\frac{\tilde{E}^{\mathrm{L}}}{\tilde{E}^{\mathrm{R}}}\right|^2 = \left|\frac{\tau_{21}}{\tau_{23}}\right|^2 \left|\frac{1+\rho_{23}e^{ik_zD}}{1+\rho_{21}e^{ik_zD}}\right|^2 , \tag{108}$$

which is obtained by dividing Eq. (91) by Eq. (92) and taking the square of the absolute value. It includes both the asymmetric radiation of the dipole within the effective medium as well as the effect of the slab surfaces.

We use the metamaterial design of Fig. 7. Forming a two-layer slab ($D = 2\Lambda_z$) and applying Eq. (108), we calculate the figure of merit ξ as a function of λ_0. Fig. 26 shows the result. We find that the emission in the positive z-direction is dominant near $\lambda_0 = 680$ nm, which is the wavelength at which the dimer and the metasurface of the previous subsection showed maximum directionality. Around $\lambda_0 = 880$ nm, the emission in the negative z-direction dominates. The material, however, is highly absorbing at this wavelength. We therefore choose a slightly redshifted wavelength of $\lambda_0 = 930$ nm. The imaginary part at of the refractive index is only 0.27 at this wavelength, while at $\lambda_0 = 880$ nm it is 0.7.

Figures 27a and 27b show the isofrequency surfaces of the refractive index n_{eff} and normalized impedance η_{eff}, respectively, at $\lambda_0 = 930$ nm for TE-polarized waves. The real part of n_{eff} is almost isotropic while the imaginary part is peaked at $\theta = 0$. Interestingly, this is entirely due to spatial dispersion, as optical anisotropy has no effect on TE-polarized waves in this material. The impedance varies with θ significantly, but is mismatched everywhere from the glass impedance. Figures 27c and 27d show n_{eff} and η_{eff} for TM-polarized waves. Here, we see that the refractive index approaches $n_{\mathrm{eff}} = 1.5$ at large propagation angles as the electric field of the plane wave becomes tilted with respect to the discs. The impedance distribution is similar in shape to that of the TE case. As the material is impedance-mismatched from glass and $\mathrm{Im}\{n_{\mathrm{eff}}\}$ is not very large, each plane wave will experience multiple reflections in

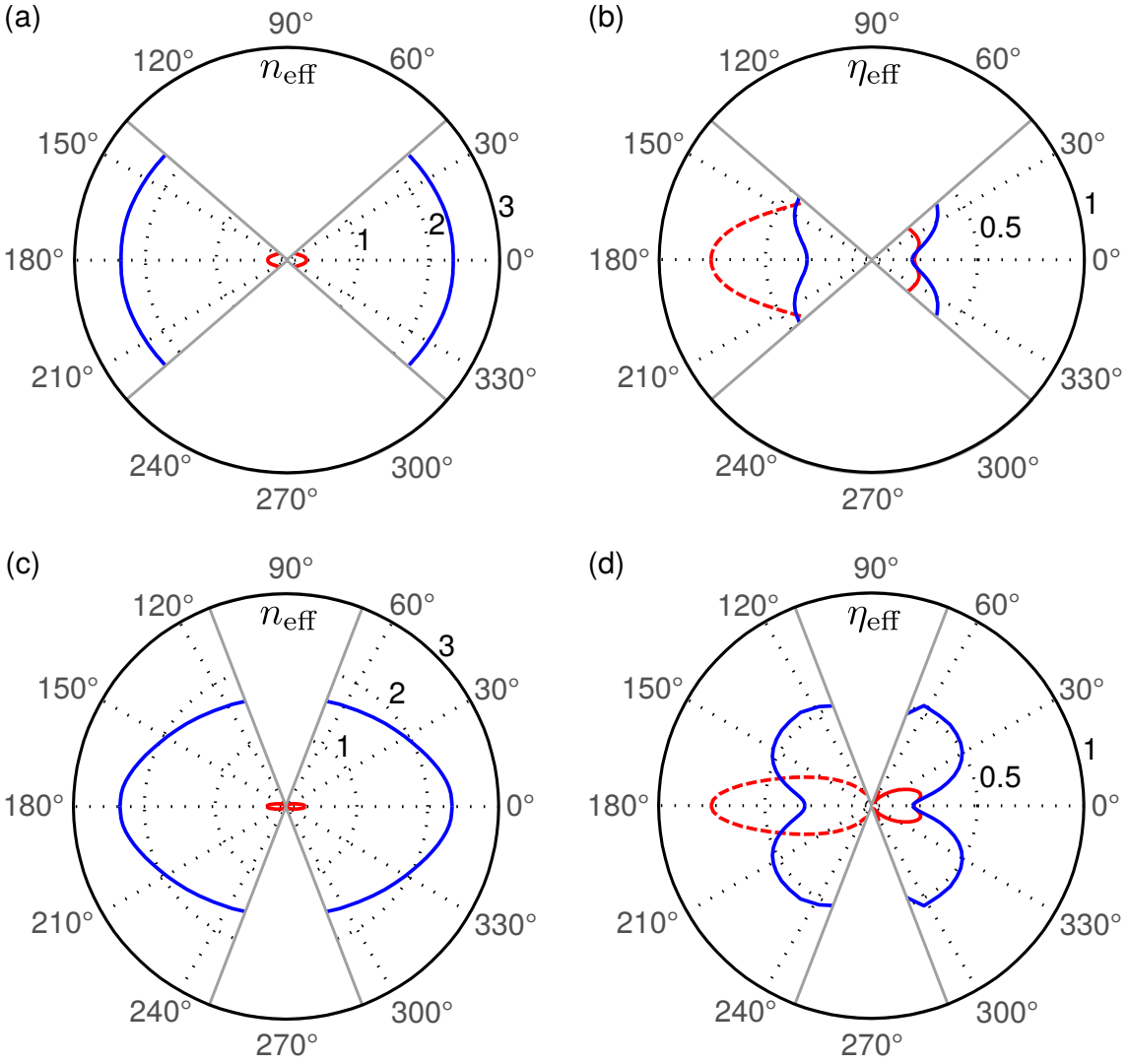

Figure 27: Wave parameters in the gold-dimer metamaterial at $\lambda_0 = 930$ nm as functions of propagation angle θ. The refractive index n_{eff} and normalized impedance η_{eff} for TE-polarized waves are shown in (a) and (b), respectively, while (c) and (d) show n_{eff} and η_{eff} for TM-polarized waves. The real/imaginary parts of each quantity are shown by blue/red lines. A dashed line indicates that the quantity is negative. White sectors correspond to propagation directions not accessible for waves incident from glass.

the slab and the output fields will be determined by the interference of these waves.

To facilitate full-wave numerical calculations, we consider a metamaterial in which the dipole emitters and the generated fields are periodic in the x-direction. The emitter is positioned between the unit cells as shown in Fig. 28a by the black dot. The amplitude distribution of the field calculated by the finite element method shows that the emission is directed mostly in the negative z-direction. The Purcell factor is calculated to be $\mathcal{P}_{\mathrm{h}} = 0.39$ and the emission enhancement factor $\mathcal{E} = 0.17$. However, 43 % of the total power is transmitted in the negative z-direction and only 2.5 % in the positive z-direction. The difference is therefore 17-fold. The slab absorbs 54 % of

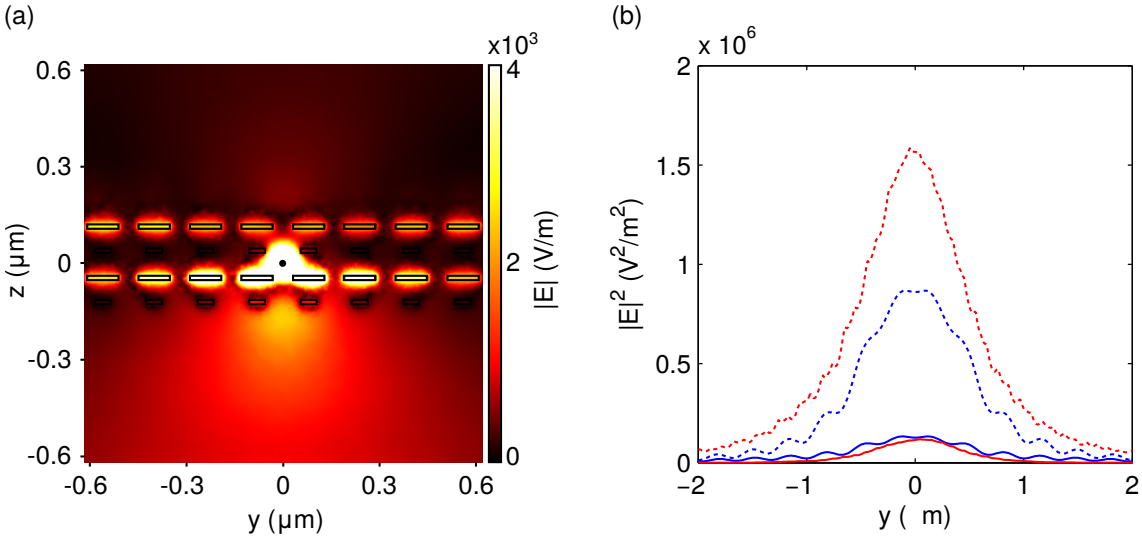

Figure 28: A dipole emitter in a two-layer slab of the gold-dimer metamaterial. The dipole [black dot in (a)] is polarized in the x-direction. The amplitude distribution of the electric field at $x = 0$, calculated by the finite-element method, is shown in (a). The intensity profiles along y are shown in (b) for $z = 350$ nm (solid lines) and $z = -350$ nm (dashed lines). The red and blue lines show the results of direct FEM and semianalytical ECDM calculations, respectively.

the power, and 0.5 % is lost through the slab sides. Figure 28b shows the intensity on the lines at $z = \pm 710$ nm, i.e., 530 nm from the slab surfaces to the positive and negative z-directions, respectively (the positions were again chosen to avoid perfectly-matched layer boundaries). The FEM result is shown in red and the result of the current-decomposition method is shown in blue. The two methods give similar results in shape, but the current decomposition method slightly underestimates the power, which can be caused by the ignored near-field energy transfer between the emitter and the metamolecules.

Let us also consider the other polarizations of the dipole using direct numerical calculations. For the z-directional dipole we find $\mathcal{P}_\mathrm{h} = 0.88$ and $\mathcal{E} = 0.76$, so this dipole actually emits faster than the y-directional one. This is an unwanted effect as the radiation pattern of the z-polarized dipole is not concentrated in the desired direction. However, if the emitter is shifted to $(x, y) = (0, \Lambda_y/2)$, then for the x-directional dipole, the Purcell factor increases to $\mathcal{P}_\mathrm{h} = 4.2$ and the emission enhancement factor to $\mathcal{E} = 0.7$, while the corresponding values for the z-directional dipole become $\mathcal{P}_\mathrm{h} = 0.78$ and $\mathcal{E} = 0.7$. Here, the y-directional dipole needed for directional emission is more efficient, but as much as 83 % of the emitted power is absorbed in the metamolecules.

To assess the directivity of a single x-polarized dipole in the slab, we use the electric-current decomposition method, as the required three-dimensional consideration of the problem is difficult to implement purely numerically. Figure 29 shows the evaluated directivity profiles in the xz- and yz-planes by the blue and red lines, respectively, which are almost identical. The maximum directivity is 5 that is slightly

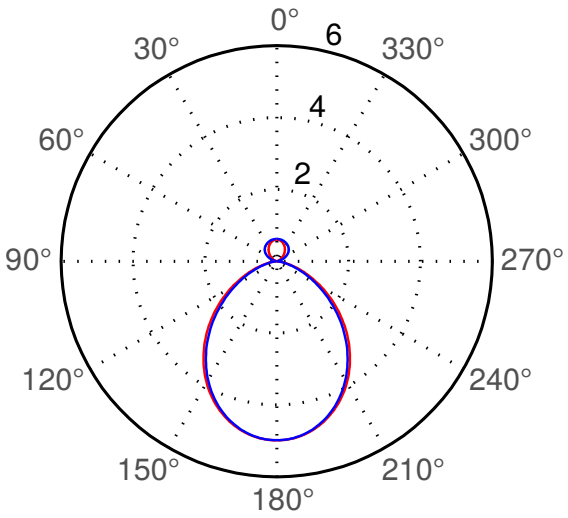

Figure 29: Directivity of an x-polarized dipole emitter located between the metamolecular layers of a two-layer slab of the gold-dimer metamaterial. The distributions in the xz-plane (blue line) and yz-plane (red line) are nearly identical.

smaller than for a dipole inside a metasurface (see Fig. 25e). Thus, we conclude that a two-layer slab of the bifacial metamaterial achieves similar directivity as a metasurface, but potentially allows for less stringent positioning of the emitters on the plane between the metamolecular layers.

To obtain any radiation, the dipole emitters must be excited which is often done by optical pumping. For fluorescent particles, pumping is usually done at a shorter wavelength than the desired emission wavelength. As was observed in Fig. 26, there is an emission peak to the positive z-direction at $\lambda_0 = 680$ nm. Let us consider this as a pump wavelength. By considering the emitters as classical dipoles absorbing the pump light, optical reciprocity ensures that when light is incident from the positive z-direction, it is efficiently coupled to the emitters. Hence, we can quantify the absorption by considering normally-incident plane waves interacting with the slab and measuring the intensity at the position of the emitter. Figure 30a shows the distribution when the wave propagates in the positive z-direction and Fig. 30b when it propagates in the negative z-direction. We notice that around $(x, y) = (0, \pm 50)$, the pump intensity exceeds that in vacuum for one direction and is close to zero in the other direction. The average pump enhancement factor is 0.2 in Fig. 30a and 0.6 in Fig. 30b. Therefore, we can use this material to create a light source emitting at $\lambda_0 = 930$ nm to the negative z-direction, being pumped at $\lambda_0 = 680$ nm from the other side of the slab. In effect, the slab will act as a nonlinear frequency converter even though the emitted radiation will not be spatially coherent. In principle, such metamaterial slabs could be used in axially-pumped lasers that conventionally have dielectric mirrors transmitting the pump light and reflecting the emitted light [71]. Here, the same effect can be achieved in a 360-nm-thick metamaterial film.

To conclude, we have observed that the positioning requirements for the emitter inside a metasurface or a metamaterial are more relaxed than in a nanoantenna. While the emission enhancement factor can be somewhat low, the overall emission

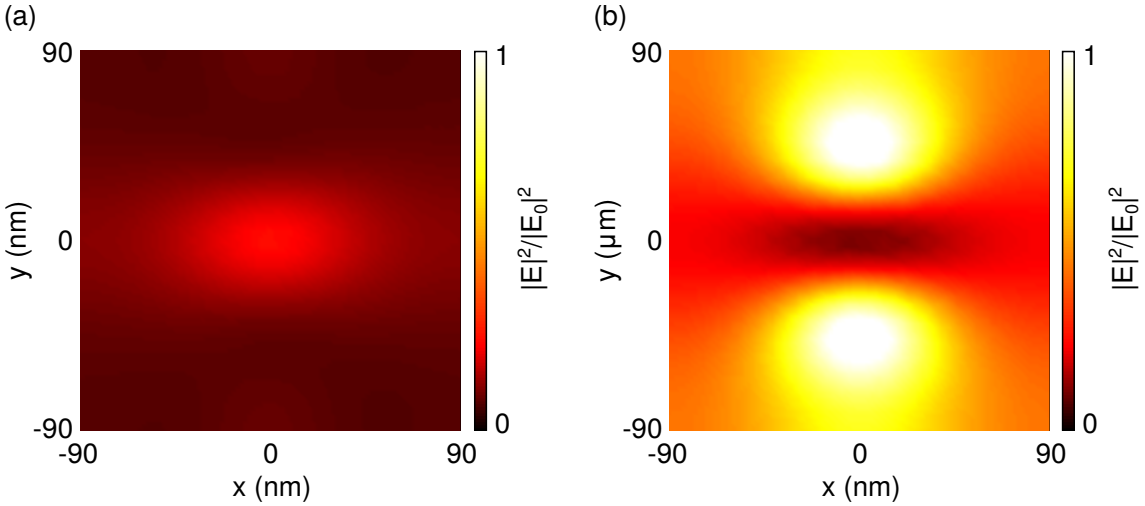

Figure 30: The intensity of a plane wave ($\lambda_0 = 680$ nm) propagating in the positive (a) and negative (b) z-directions, measured between the metamolecular layers of a two-layer slab of the gold-dimer metamaterial. The profiles are restricted to the size of a single unit cell.

efficiency can be offset by a larger number of emitters. In addition, we have shown that a thin metamaterial slab can simultaneously make an emitter single-directional and allow effective optical pumping from the other direction.

6 Summary and outlook

In this work, the propagation and generation of light in metamaterials and related nanostructures was studied. The metamaterials were characterized in terms of wave parameters calculated by using a semianalytical "interferometric" approach. The interaction of optical beams with metamaterial slabs was studied using a plane-wave decomposition method. We first applied these tools to design a diffraction-compensating metamaterial. We demonstrated that essentially arbitrary optical images can be transferred through a diffraction-compensating metamaterial slab with low distortion and optical absorption loss. Simultaneously, the material can be designed such that it is approximately impedance-matched to its surroundings, which eliminates surface reflection losses without a need in any additional anti-reflection coatings. We also found that the material preserves the intensity distribution of a circularly-polarized image propagating through it, gradually making the field consist of TM-polarized waves only. The design can be improved to compensate diffraction also for waves that are evanescent outside the material in order to achieve sub-diffraction-limited resolution. An interesting prospect would be to construct a diffraction-compensating metamaterial out of dielectrics or semiconductors, which would even further reduce the absorption loss. This could lead to the development of new types of laser resonators. Applied to thin films, such as anti-reflection coatings, diffraction compensation could provide a way to eliminate the dependence of their operation on the incidence angle of radiation.

We showed that a slab of a bifacial metamaterial can reflect quite different amounts of light by its two sides. We also demonstrated that the material can be tuned to act as a reflective spatial filter, reflecting normally-incident waves and absorbing obliquely-incident ones. Such highly spatially dispersive metamaterials are very promising for applications, which require spatially selective absorption or reflection of optical fields: e.g., one can create spatial filters that are translationally invariant, operating regardless of the location of the focal spot of an optical beam. We have also demonstrated that even highly symmetric metamaterials can lack polarization modes, converting polarization of light purely by spatial dispersion. This work highlights the fact that one must always take into account the possibility that even metamaterials with as simple structural units as discs may turn out not to have polarization modes. As a result, one must discard the description of the material in terms of wave parameters in favour of another, transfer-matrix-based approach we have developed for this purpose.

For studying the radiation of quantum emitters embedded in spatially dispersive optical media, we developed a new semianalytical method that uses the wave parameters to calculate the emitted fields. The method is based on an electric-current wave decomposition that is exact in homogeneous materials and approximative in metamaterials, where near-field interaction between the emitter and metamolecules contribute to the radiation patterns and the Purcell effect. To treat more general structures, as well as make more accurate computations, we used direct numerical solutions as well. We studied different nanostructures to modify the radiation of quantum emitters. In particular, we demonstrated that a metal waveguide at its

cutoff frequency acts as a two-dimensional near-zero-index metamaterial, forcing independent dipole emitters to preferably radiate in phase and to increase the emission rate. We also showed that the wavefronts of the radiation can take the shape of the waveguide, an effect which can be used to flatten the wavefronts or to focus light to a diffraction-limited spot even when incoherent spontaneous emission is used as the light source.

Moreover, we characterized the action of quantum emitters embedded in a diffraction-compensating metamaterial slab and found that the emitters radiate collimated beams that are efficiently coupled out of the slab. Here, the current-decomposition method proved to be very efficient and accurate, even though the emitter-metamolecule near-field coupling was present. Diffraction compensation can be used to confine optical fields without waveguides, which can find interesting applications in integrated optics. An especially interesting future research prospect is to study these materials in conjunction with molecules providing optical gain.

Finally, we studied the interaction of quantum emitters with gold dimer metamolecules. The dimers can be used as single nanoantennas forcing a dipole emitter placed in the metamolecule to radiate in one direction only. While the directivity was not perfect, we found that it can be improved by using a metasurface constructed of multiple dimers. We also used a bifacial metamaterial to direct the emission. The current-decomposition method was successfully used in this case to find the wavelengths of maximum directivity from the spectra of the calculated wave parameters. We predict there is room for improvement of the introduced directional meta-emitters, e.g., via Mie and Fabry-Pérot resonances in nanostructures with high refractive index, which can also lead to an increase of the emission efficiency.

References

[1] C. M. Soukoulis and M. Wegener, "Past achievements and future challenges in the development of three-dimensional photonic metamaterials", *Nat. Photon.* **5**, 523 (2011)

[2] K. Yao and Y. Liu, "Plasmonic metamaterials", *Nanotechnol. Rev.* **3**, 177 (2014)

[3] N. Meinzer, W. L. Barnes, I. R. Hooper, "Plasmonic meta-atoms and metasurfaces", *Nat. Photon.* **8**, 889 (2014)

[4] V. M. Shalaev, "Optical negative-index metamaterials", *Nat. Photon.* **1**, 41 (2007)

[5] R. W. Ziolkowski, "Propagation in and scattering from a matched metamaterial having a zero index of refraction", *Phys. Rev. E* **70**, 046608 (2004)

[6] A. Poddubny, I. Iorsh, P. Belov and Y. Kivshar, "Hyperbolic metamaterials", *Nat. Photon.* **7**, 958 (2013)

[7] V. K. Valev, J. J. Baumberg, C. Sibilia, T. Verbiest, "Chirality and Chiroptical Effects in Plasmonic Nanostructures: Fundamental, Recent Progress, and Outlook", *Adv. Mater.* **25**, 2517 (2013)

[8] J. B. Pendry, "Negative refraction makes a perfect lens", *Phys. Rev. Lett.* **85**, 3966 (2006)

[9] Z. Jacob, L. V. Alekseyev and E. Narimanov, "Optical Hyperlens: Far-field imaging beyond the diffraction limit", *Opt. Express* **14**, 8247 (2006)

[10] L. Ferrari, D. Lu, D. Lepage and Z. Liu, "Enhanced spontaneous emission inside hyperbolic metamaterials", *Opt. Express* **22**, 4301 (2014)

[11] M. A. Noginov, H. Li., Y. A. Barnakov, D. Dryden, G. Nataraj, G. Zhu, C. E. Bonner, M. Mayy, Z. Jacob and E. E. Narimanov, "Controlling spontaneous emission with metamaterials", *Opt. Lett.* **35**, 1863 (2010)

[12] D. Costantini, A. Lefebvre, A.-L. Coutrot, I. Moldovan-Doyen, J. P. Hugonin, S. Boutami, F. Marquier, H. Benisty and J.-J. Greffet, "Plasmonic Metasurface for Directional and Frequency-Selective Thermal Emission", *Phys. Rev. Appl.* **4**, 014023 (2015)

[13] A. Alù, M. G. Silveirinha, A. Salandrino and N. Engheta, "Epsilon-near-zero metamaterials and electromagnetic sources: Tailoring the radiation phase pattern", *Phys. Rev. B* **75**, 155410 (2007)

[14] N. I. Zheludev, S. L. Prosvirnin, N. Papasimakis and V. A. Fedotov, "Lasing spaser", *Nat. Photon.* **2**, 351 (2008)

[15] H. Chen, C. T. Chan and P. Sheng, "Transformation optics and metamaterials", *Nat. Mater.* **9**, 387 (2010)

[16] M. Silveirinha and N. Engheta, "Tunneling of Electromagnetic Energy through Subwavelength Channels and Bends using ε-Near-Zero Materials", *Phys. Rev. Lett.* **97**, 157403 (2006)

[17] B. D. F. Casse, W. T. Lu, Y. J. Huang, E. Gultepe, L. Menon and S. Sridhar, "Super-resolution imaging using a three-dimensional metamaterials nanolens", *Appl. Phys. Lett.* **96**, 023114 (2010)

[18] V. Kivijärvi, M. Nyman, A. Shevchenko and M. Kaivola, "An optical metamaterial with simultaneously suppressed optical diffraction and surface reflection", *J. Opt.* **18**, 035103 (2016)

[19] V. Kivijärvi, M. Nyman, A. Shevchenko and M. Kaivola, "Optical-image transfer through a diffraction-compensating metamaterial", *Opt. Express* **24**, 9806 (2016)

[20] A. E. Minovich, A. E. Miroshnichenko, A. Y. Bykov, T. V. Murzina, D. N. Neshev and Y. S. Kivshar, "Functional and nonlinear optical metasurfaces", *Laser Photonics Rev.* **9**, 195 (2015)

[21] G. Shvets and I. Tsukerman, *Plasmonics and Plasmonic Metamaterials*, World Scientific (2012)

[22] P. Grahn, *Theoretical Description and Design of Optical Nanomaterials*, D. Sc. (Tech.) thesis, Department of Applied Physics, Aalto University School of Science, Espoo, Finland (2014)

[23] P. Grahn, A. Shevchenko and M. Kaivola, "Interferometric description of optical metamaterials", *New J. Phys.* **15** 113044 (2013)

[24] P. Grahn, A. Shevchenko and M. Kaivola, "Theoretical desription of bifacial optical nanomaterials", *Opt. Express* **21**, 23471 (2013)

[25] A. Shevchenko, P. Grahn and M. Kaivola, "Internally twisted spatially dispersive optical metamaterials", *J. Nanophoton.* **8**, 083074 (2014)

[26] V. Kivijärvi, M. Nyman, A. Karrila, P. Grahn, A. Shevchenko and M. Kaivola, "Interaction of metamaterials with optical beams", *New J. Phys.* **17**, 063019 (2015)

[27] A. Shevchenko, V. Kivijärvi, P. Grahn, M. Kaivola and K. Lindfors, "Bifacial Metasurface with Quadrupole Optical Response", *Phys. Rev. Appl.* **4**, 024019 (2015)

[28] M. Pelton, "Modified spontaneous emission in nanophotonic structures", *Nat. Photon.* **9**, 427 (2015)

[29] L. Novotny and B. Hecht, *Principles of Nano-Optics*, Cambridge University Press (2006).

[30] G. Russakoff, "A Derivation of the Macroscopic Maxwell Equations", *Am. J. Phys.* **38**, 1188 (1970)

[31] L. D. Landau, E. M. Lifshitz, *Electrodynamics of Continuous Media*, Pergamon, Oxford (1960)

[32] P. A. Belov, R. Marqués, S. I. Maslovski, I. S. Nefedov, M. Silveirinha, C. R. Simovski and S. A. Tretyakov, "Strong spatial dispersion in wire media in the very large wavelength limit", *Phys. Rev. B* **67**, 113103 (2003)

[33] B. E. A. Saleh and M. C. Teich, *Fundamentals of Photonics*, Wiley (2007)

[34] M. G. Silveirinha, "Poynting vector, heating rate, and stored energy in structured materials: A first-principles derivation", *Phys. Rev. B* **80**, 235120 (2009)

[35] M. F. Bishop and A. A. Maradudin, "Energy flow in a semi-infinite spatially dispersive absorbing dielectric", *Phys. Rev. B* **14**, 3384 (1976)

[36] V. Veselago, "The electrodynamics of substances with simultaneously negative values of ϵ and μ", *Sov. Phys. Usp.* **10**, 509 (1964)

[37] J. A. Stratton, *Electromagnetic theory*, McGraw-Hill Book Company (1994)

[38] J. D. Joannopoulos, S. G. Johnson, J. N. Winn and R. D. Meade, *Photonic Crystals: Molding the Flow of Light*, 2nd edition, Princeton University Press (2008)

[39] A. Andryieuski, S. Ha, A. A. Sukhorukov, Y. S. Kivshar and A. V. Lavrinenko, "Bloch-mode analysis for retrieving effective parameters of metamaterials", *Phys. Rev. B* **86**, 035127 (2012)

[40] M. G. Silveirinha, "Metamaterial homogenization approach with application to the characterization of microstructured composited with negative parameters", *Phys. Rev. B* **75**, 115104 (2007)

[41] D. R. Smith, S. Schultz, P. Markoš and C. M. Soukoulis, "Determination of effective permittivity and permeability of metamaterials from reflection and transmission coefficients", *Phys. Rev. B* **65**, 195104 (2002)

[42] D. R. Smith and J. B. Pendry, "Homogenization of metamaterials by field averaging", *J. Opt. Soc. Am. B* **23**, 391 (2006)

[43] R. Marqués, F. Medina and R. Rafii-El-Idrissi, "Role of bianisotropy in negative permeability and left-handed metamaterials", *Phys. Rev. B* **65**, 144440 (2002)

[44] C. E. Kriegler, M. S. Rill, S. Linden and M. Wegener, "Bianisotropic Photonic Metamaterials", *IEEE J. Sel. Top. Quant.* **16**, 367 (2010)

[45] T. Koschny, P. Markoš, D. R. Smith and C. M. Soukoulis, "Resonant and antiresonant frequency dependence of the effective parameters of metamaterials", *Phys. Rev. E* **68**, 065602 (2003)

[46] M. Nyman, "Propagation of optical beams through metamaterial slabs", Bachelor's thesis, Aalto University School of Science (2014)

[47] J. W. Goodman, *Introduction to Fourier Optics*, 2nd edition, McGraw-Hill (1996)

[48] K. Kempa, X. Wang, Z. F. Ren and M. J. Naughton, "Discretely guided electromagnetic effective medium", *Appl. Phys. Lett.* **92**, 043114 (2008)

[49] D. W. Prather, S. Shi, J. Murakowski, G. J. Schneider, A. Sharkawy, C. Chen, B. Miao and R. Martin, "Self-collimation in photonic crystal structures: a new paradigm for applications and device development", *J. Phys. D: Appl. Phys.* **40**, 2635 (2007)

[50] J. Shin and S. Fan, "Conditions for self-collimation in three-dimensional photonic crystals", *Opt. Lett.* **30**, 2397 (2005)

[51] J. G. Hayashi, S. Fleming, B. T. Kuhlmey and A. Argyros, "Metal selection for wire array metamaterials for infrared frequencies", *Opt. Express* **23**, 29867 (2015)

[52] B. Wood, J. B. Pendry and D. P. Tsai, "Directed subwavelength imaging using a layered metal-dielectric system", *Phys. Rev. B* **74**, 115116 (2006)

[53] V. Zabelin, L. A. Dunbar, N. Le Thomas, R. Houdré, M. V. Kotlyar, L. O'Faolain and T. F. Krauss, "Self-collimating photonic crystal polarization beam splitter", *Opt. Lett.* **32**, 530 (2007)

[54] D. Zhao, C. Zhou, Q. Gong and X. Jiang, "Lasing cavities and ultra-fast switch based on self-collimation of photonic crystal", *J. Phys. D: Appl. Phys.* **41**, 115108 (2008)

[55] This is the divergence angle where the far-field intensity is $1/e^2$ of the maximum far-field intensity in the beam.

[56] M. Nyman, "Diffraction-compensating metamaterial films", special assignment, Aalto University School of Science (2015)

[57] P. Grahn, A. Shevchenko and M. Kaivola, "Electric dipole-free interaction of visible light with pairs of subwavelength-size silver particles", *Phys. Rev. B* **86**, 035419 (2012)

[58] P. B. Johnson and R. W. Christy, "Optical Constants of the Noble Metals", *Phys. Rev. B* **6**, 4370 (1972).

[59] Z. Li, M. Mutlu and E. Ozbay, "Chiral metamaterials: from optical activity and negative refractive index to asymmetric transmission", *J. Opt.* **15**, 023001 (2013)

[60] E. Plum, V. A. Fedotov, A. S. Schwanecke and N. I. Zheludev, "Giant optical gyrotropy due to electromagnetic coupling", *Appl. Phys. Lett.* **90**, 223113 (2007)

[61] C. Menzel, C. Helgert, C. Rockstuhl, E.-B. Kley, A. Tünnermann, T. Pertsch and F. Lederer, "Asymmetric Transmission of Linearly Polarized Light at Optical Metamaterials", *Phys. Rev. Lett.* **104**, 253902 (2010)

[62] M. Giloan and S. Astilean, "Negative index optical chiral metamaterial based on asymmetric hexagonal arrays of metallic triangular nanoprisms", *Opt. Comm.* **315**, 122 (2014)

[63] A. G. Curto, G. Volpe, T. H. Taminiau, M. P. Kreuzer, R. Quidant and N. F. van Hulst, "Unidirectional Emission of a Quantum Dot Coupled to a Nanoantenna", *Science* **329**, 930 (2010)

[64] D. Dregely, R. Taubert, J. Dorfmüller, R. Vogelgesang, K. Kern and H. Giessen, "3D optical Yagi-Uda nanoantenna array", *Nat. Commun.* **2**:267 (2011)

[65] T. B. Hoang, G. M. Akselrod, C. Argyropoulos, J. Huang, D. R. Smith and M. H. Mikkelsen, "Ultrafast spontaneous emission source using plasmonic nanoantennas", *Nat. Commun.* **6**:7788 (2015)

[66] P. Lodahl, S. Mahmoodian, S. Stobbe, "Interfacing single photons and single quantum dots with photonic nanostructures", *Rev. Mod. Phys.* **87**, 347 (2015)

[67] L. Gu, J. E. Livenere, G. Zhu, T. U. Tumkur, H. Hu, C. L. Cortes, Z. Jacob, S. M. Prokes and M. A. Noginov, "Angular distribution of emission from hyperbolic metamaterials", *Sci. Rep.* **4**, 7327 (2014)

[68] P. Moitra, Y. Yang, Z. Anderson, I. I. Kravchenko, D. P. Briggs and J. Valentine, "Realization of an all-dielectric zero-index optical metamaterial", *Nat. Photon.* **7**, 791 (2013)

[69] Y-W. Huang, W. T. Chen, P. C. Wu, V. A. Fedotov, N. I. Zheludev and D. P. Tsai, "Toroidal Lasing Spaser", *Sci. Rep.* **3**: 1237 (2013)

[70] H. J. Metcalf and P. van der Straten, *Laser Cooling and Trapping*, Springer-Verlag (1999)

[71] S. Hooker and C. Webb, *Laser Physics*, Oxford University Press (2010).

[72] H. Walther, B. T. H. Varcoe, B-G. E. Englert, T. Becker, "Cavity quantum electrodynamics", *Rep. Prog. Phys.* **69**, 1325 (2006)

[73] J. A. Kong, "Electromagnetic Fields Due to Dipole Antennas over Stratified Anisotropic Media", *Geophys.* **37**, 985 (1972)

[74] L. Penninck, P. De Visschere, J. Beeckman and K. Neyts, "Dipole radiation within one-dimensional anisotropic microcavities: a simulation method", *Opt. Express* **19**, 18558 (2011)

[75] S. R. J. Brueck, "Radiation from a Dipole Embedded in a Dielectric Slab", *IEEE J. Sel. Topics Quantum Electron.* **6**, 899 (2000)

[76] M. Memarian and G. V. Eleftheriades, "Dipole radiation near anisotropic low-permittivity media", *Progress In Electromagnetics Research* **142**, 437 (2013)

[77] Y. Huang, *Dyadic Green's Functions for Layered General Anisotropic Media and Their Application to Radiation of Dipole Antennas*, Ph. D. thesis, Syracuse University (2014)

[78] E. Vesseur, T. Coenen, H. Caglayan, N. Engheta and A. Polman, "Experimental Verification of $n = 0$ Structures for Visible Light", *Phys. Rev. Lett.* **110**, 013902 (2013)

[79] W. Zhu, I. D. Rukhlenko and M. Premaratne, "Light amplification in zero-index metamaterial with gain inserts", *Appl. Phys. Lett.* **101**, 031907 (2012)

[80] M. Silveirinha and N. Engheta, "Tunneling of Electromagnetic Energy through Subwavelength Channels and Bends using ϵ-Near-Zero Materials", *Phys. Rev. Lett.* **97**, 157403 (2006)

[81] R. Maas, J. Parsons, N. Engheta and A. Polman, "Experimental realization of an epsilon-near-zero metamaterial at visible wavelengths", *Nat. Photon.* **7**, 907 (2013)

[82] N. E. Nefedkin, E. S. Andrianov, A. A. Zyablovsky, A. A. Pukhov, A. V. Dorofeenko, A. P. Vinogradov and A. A. Lisyansky, "Superradiance of a subwavelength array of classical nonlinear emitters", *Opt. Express* **24**, 3464 (2016)

[83] T. Lund-Hansen, S. Stobbe, B. Julsgaard, H. Thyrrestrup, T. Sünner, M. Kamp, A. Forchel and P. Lodahl, "Experimental Realization of a Highly Efficient Broadband Coupling of Single Quantum Dots to a Photonic Crystal Waveguide", *Phys. Rev. Lett.* **101**, 113903 (2008)

[84] F. J. Rodríguez-Fortuño, G. Marino, P. Ginzburg, D. O'Connor, A. Martínez, G. A. Wurtz and A. V. Zayats, "Near-Field Interference for the Unidirectional Excitation of Electromagnetic Guided Modes", *Science* **340**, 328 (2013)

[85] W. Y. Liang, J. W. Dong and H. Z. Wang, "Directional emitter and beam splitter based on self-collimation effect", *Opt. Express* **15**, 1234 (2007)

[86] J-M. Park, S-G. Lee, H. Y. Park and J-E. Kim, "Efficient beaming of self-collimated light from photonic crystals", *Opt. Express* **16**, 20354 (2008)

[87] A. E. Siegman, *Lasers*, University Science Books (1986)

[88] A. Kinkhabwala, Z. Yu, S. Fan, Y. Avlasevich, K. Müllen and W. E. Moerner, "Large single-molecule fluorescence enhancements produced by a bowtie nanoantenna", *Nat. Photon.* **3**, 654 (2009)

[89] L. Novotny and N. van Hulst, "Antennas for light", *Nat. Photon.* **5**, 83 (2011)

[90] C. F. Bohren and D. R. Huffman, *Absorption and Scattering of Light by Small Particles*, Wiley (1983)